

Numerical Modelling of Wheel-rail Dynamic Interactions with an Explicit Finite Element Method

Yang, Zhen

DOI

[10.4233/uuid:8acb9b48-bf77-45b2-a0d6-1cf6658f749e](https://doi.org/10.4233/uuid:8acb9b48-bf77-45b2-a0d6-1cf6658f749e)

Publication date

2018

Document Version

Final published version

Citation (APA)

Yang, Z. (2018). *Numerical Modelling of Wheel-rail Dynamic Interactions with an Explicit Finite Element Method*. [Dissertation (TU Delft), Delft University of Technology]. <https://doi.org/10.4233/uuid:8acb9b48-bf77-45b2-a0d6-1cf6658f749e>

Important note

To cite this publication, please use the final published version (if applicable). Please check the document version above.

Copyright

Other than for strictly personal use, it is not permitted to download, forward or distribute the text or part of it, without the consent of the author(s) and/or copyright holder(s), unless the work is under an open content license such as Creative Commons.

Takedown policy

Please contact us and provide details if you believe this document breaches copyrights. We will remove access to the work immediately and investigate your claim.

**Numerical Modelling of Wheel-rail
Dynamic Interactions with an Explicit
Finite Element Method**

Zhen YANG

Numerical Modelling of Wheel-rail Dynamic Interactions with an Explicit Finite Element Method

Dissertation

for the purpose of obtaining the degree of doctor
at Delft University of Technology
by the authority of the Rector Magnificus prof.dr.ir. T.H.J.J. van der Hagen
chair of the Board for Doctorates
to be defended publicly on
Monday 4 June 2018 at 12:30 o'clock

by

Zhen YANG

Master of Engineering in Highway and Railway Engineering,
Tongji University, Shanghai, China
Born in Hohhot, Inner Mongolia, China

This dissertation has been approved by the promotor.

Composition of the doctoral committee:

Rector Magnificus,	Chairperson
Prof.dr.ir. R.P.B.J. Dollevoet	Delft University of Technology, promotor
Prof.dr.ir. Z. Li	Delft University of Technology, promotor

Independent members:

Prof. dr. E. Kabo	Chalmers University of Technology
Prof. dr. ir. D.J. Schipper	Universiteit Twente
Prof. dr. ir. A.S.J. Suiker	Technische Universiteit Eindhoven
Prof. dr. ir. J. Rots	Technische Universiteit Delft
Prof. dr. ir. A. Metrikine	Technische Universiteit Delft

This dissertation was financially supported by:



ISBN: 978-94-6366-048-8

Printed by: Gildeprint – Enschede

Copyright © 2018 by Zhen Yang (09yangzhenm@gmail.com)

An electronic copy of this dissertation is available at <http://repository.tudelft.nl/>

SUMMARY

The modelling of wheel-rail dynamic interactions is crucial for accurately predicting wheel/track deterioration and dynamic behaviour. A reliable wheel-rail dynamic interaction model requires a careful treatment of wheel-rail frictional rolling contact and a proper consideration of dynamic effects related to the contact. Since the wheel-rail interaction due to the frictional rolling contact significantly influences the vehicle dynamics and stability, and the dynamic effects involved in wheel-rail interactions can be increased by wheel-rail high-speed rolling, a systematic study of wheel-rail dynamic interactions is highly desired within the context of booming high-speed railways.

Explicit finite element methods (FEMs) are able to handle nonlinear material properties and arbitrary contact geometries and consider dynamic effects; thus, the explicit FEMs are suitable for predicting wheel-rail frictional rolling contact and high-frequency structural dynamic responses. However, existing studies on explicit finite element (FE) wheel-rail interactions have generally adopted algorithm-optimised commercial programs to efficiently process the large amounts of elements required in the detailed modelling of wheel/track structures and perform time integration with small time steps. To facilitate other researchers to perform simulations of wheel-rail dynamic interactions with the explicit FEM programs, systematic perceptions of the involved algorithms and the modelling know-how should be provided. In this context, this study systematically explores the core algorithms employed in the explicit FE wheel-rail dynamic interactions and theoretically demonstrates that the explicit FEM is an ideal approach because it fully couples the calculation of wheel-rail frictional rolling contact with the calculation of high-frequency dynamic responses of wheel and rail structures. To promote the broad use of the method, this study also proposes a detailed procedure for establishing robust explicit FE wheel-rail dynamic interaction models and converting outputs into wheel-rail contact and dynamic responses.

Three typical numerical examples are presented subsequently to demonstrate the effectiveness of the explicit FEM for the modelling of wheel-rail dynamic interactions. The first example presents an explicit FE wheel-insulated rail joint (IRJ) dynamic interaction model, which is validated against a comprehensive field measurement including a hammer test and a pass-by measurement. The simulated transient impact contact solutions tend to vary noticeably with the time step, indicating that the dynamic effects play important roles in the wheel-IRJ impact contact. The good agreement between the simulated ‘footprints’ of the contact patch and the in situ running band implies that the model with the measured geometry provides more realistic predictions of the transient solutions of the impact contact at the target IRJ. In addition, regular wave patterns are produced both before and during the wheel-IRJ impacts in the simulations, and these patterns reflect continuum vibrations excited by wheel-

rail frictional rolling and impact contact and confirm that the simulated transient contact solutions are reliable.

The second numerical example proposes an explicit FE wheel-rail dynamic interaction model with wheel lateral motion to investigate wheel-rail squeal-exciting contact with the involvement of dynamic effects, unsteady lateral creepage and velocity-dependent friction. The proposed model is considered to be capable of reproducing the two commonly considered mechanisms leading to squeal: falling-friction and mode-coupling. The analyses of the simulated results indicate that the explicit FE dynamic interaction model can comprehensively consider and accurately predict the wheel-rail dynamic contact and structural dynamic behaviour.

The third numerical example applies the explicit FEM to simulate the non-steady-state transition of wheel-rail rolling from single-point to two-point contact. The stress and adhesion-slip distribution under the single-point contact condition and the positions and shapes of the contact patches under the two-point contact condition correspond well with the results in the literature. Wave phenomena are observed in the wheel and rail continua, especially by the transition from single-point to two-point contact. Compared to those in single-point contact, stronger waves embodied in the alternation of the compression intensification and relaxation can be observed upon the occurrence of the second contact point. Moreover, the contact transition is found to cause the full slip of the entire wheel-rail contact. These factors may contribute to contact instability and consequently squeal and corrugation.

As main findings of wheel-rail dynamic contact solutions, waves produced by the proposed explicit FE wheel-rail dynamic interaction models are then analysed. The simulated waves are categorised as the impact-induced wave, the large-creepage-induced wave and the perturbation-induced wave. Intrinsically, they are all generated by the dynamic effects of wheel-rail interactions. The perturbation-induced wave is suspected to be closely related to the dynamic friction-induced instability. According to the characteristics of waves, this study corresponds the simulated large-creepage-induced wave to Rayleigh wave: the simulated wave is formed in particles with retrograde elliptical motion as Rayleigh wave, and the simulated wave speed is also in line with that of Rayleigh wave travelling in steel. The reproduction of the Rayleigh wave confirms that the proposed explicit FEM is appropriate and reliable for the modelling of wheel-rail dynamic interactions.

In conclusion, the proposed explicit FEM provides a suitable approach to the modelling of wheel-rail dynamic interactions. Improvements may, however, still be required to reproduce the ‘enigmatic’ squeal and corrugation, whose occurrences are sensitive to both the structural dynamic behaviour and contact conditions. The improvements may include the development and implementation of dynamic contact algorithms for more realistic contact solutions, proposing more realistic kinematic boundary conditions or a full wheelset model for accurately predicting wheel curving motion, and an application of solid rail-pad representation that may improve the accuracies of the lateral and longitudinal dynamics simulations.

SAMENVATTING

Het goed en nauwkeurig kunnen modelleren van de wiel spoor interactie is van grote waarde voor het voorspellen van slijtage en degeneratie van het spoor. Hiervoor is een contact model nodig wat niet alleen de rekening houdt met de frictie in een rollend contactpunt, maar ook de dynamische effecten van dit punt kan berekenen. Daarnaast beïnvloeden deze parameters ook het dynamisch gedrag en de stabiliteit van de trein, met name bij hoge snelheid. Door de stijgende populariteit van hogesnelheidstreinen, is het van belang om meer inzicht te krijgen in deze parameters.

Met behulp van eindige elementen modellen en expliciete tijdsintegratie is het mogelijk om modellen met niet lineaire materiaaleigenschappen en elke vorm te maken. Hierdoor zijn deze modellen geschikt om het rollend contact en de hoog frequente dynamica van het spoor te simuleren. In de huidige literatuur over het gebruik van expliciete tijdsintegratie voor wiel rail interactie wordt met name gebruik gemaakt van optimalisaties om deze simulaties met commerciële software te kunnen doen. Om meer inzicht te verschaffen in deze methode is achtergrond informatie over de noodzakelijke algoritmes en kennis over het opzetten van het model van groot belang. In dit onderzoek worden de kern algoritmes systematisch toegepast op de wiel rail interactie simulatie. Aan de hand hiervan wordt ook aangetoond dat deze methode ook direct een gekoppelde oplossing geeft voor zowel de frictie in het contact punt en de hoog frequente dynamica van het wiel en de spooronderdelen. Om het gebruik van deze methode verder te stimuleren, worden er ook stappen gepresenteerd om een stabiele simulatie op te zetten en om de data te verwerken naar contactparameters.

In deze dissertatie wordt deze methode aan de hand van drie numerieke voorbeelden gepresenteerd. In het eerste voorbeeld wordt de dynamische interactie tussen een Elektrische Scheidingslas (ES-las) en een rollend wiel gesimuleerd met behulp van een eindige elementen model en expliciete tijdsintegratie. Het gebruikte model voor de ES-las is vooraf gevalideerd aan de hand van hamer impactmetingen en treinpassages. De resultaten van de simulaties zijn sterk afhankelijk van de gekozen tijdstap, waaruit blijkt dat de dynamica een belangrijke rol speelt. Verder komen de gesimuleerde vormen van het contact oppervlak goed overeen met het verloop van rijspiegel als het gemeten dwarsprofiel voor de ES-las wordt gebruikt voor de simulatie, wat er op duidt dat de tijdsresponsie van deze ES-las goed gesimuleerd kan worden met dit model. Daarnaast zijn er ook golfpatronen voor en tijdens de impact waargenomen in de simulatie. Deze patronen komen overeen met de continuüm oplossing voor een rollend frictie contact, wat onderstreept dat deze resultaten betrouwbaar zijn.

In het tweede voorbeeld wordt de wiel rail interactie gesimuleerd met zijdelingse verplaatsing van het wiel. Hierdoor treden extra dynamische effecten, onstabiele kruip en snelheidsafhankelijke frictie op, wat piepende wielen veroorzaakt. Met het model kunnen de twee belangrijkste oorzaken van piepende wielen worden gesimuleerd; falling-friction en

mode-coupling. Op basis van de analyse van deze simulatie kan worden geconcludeerd dat het eindige elementen model nauwkeurig het dynamisch contact en de structurele dynamica kan voorspellen.

In het derde model wordt een niet stationaire overgang van het wiel rail contact gesimuleerd; van een enkel contactpunt naar een tweepunt contact. De spanning en de adhesie-slip verdeling van het enkele contactpunt en de locaties en vormen van de contactpunten voor het tweepunt contact komen goed overeen met de resultaten uit de literatuur. Opnieuw zijn golfpatronen waargenomen in het continuüm van het wiel en de spoorstaaf, met name tijdens de overgangsfase. Een toename in de intensiteit van de golfpatronen is waargenomen vlak voordat het tweede contactpunt ontstaat. Daarnaast blijkt dat tijdens deze overgangsfase het contact punt volledig slipt. Deze factoren zouden kunnen bijdragen aan contact instabiliteit wat piepende wielen en golfslijtage oplevert.

Als belangrijkste resultaat van de simulatie, zijn de gesimuleerde golfpatronen verder geanalyseerd. Hierin is onderscheid gemaakt tussen golfpatronen veroorzaakt door de impact, kruip of verstoring. Elk van deze golfpatronen wordt in principe veroorzaakt door het dynamische wiel rail contact. De verstoringpatronen worden waarschijnlijk veroorzaakt door de onstabiele dynamische wrijving. De karakteristieke eigenschappen van golfpatronen veroorzaakt door kruip zijn gelijk aan die van de Rayleigh golven, daarnaast is ook de golfsnelheid hiervan gelijk aan de snelheid van een Rayleigh golf door staal. De goede overeenkomst tussen de Rayleigh golven en de gesimuleerde golfpatronen is een extra bewijs dat deze methode betrouwbaar is voor het simuleren van wiel rail contact.

Op basis van deze dissertatie kan worden geconcludeerd dat een eindig elementen model in combinatie met een expliciet tijdsintegratieschema goed in staat is om het dynamische wiel rail contact te simuleren. Er zijn nog wel vervolgstappen nodig voordat met deze methode piepende wielen en het ontstaan van golfslijtage kan worden gereproduceerd. Dit zijn twee voorbeelden die typisch afhankelijk zijn van zowel het contact, als de dynamica van het systeem. Als verbetering kan een dynamisch contact algoritme worden geïmplementeerd waarmee nog realistischere contact simulaties kunnen worden gedaan, een compleet draaistel worden gemodelleerd zodat de loop van de wielen beter gedefinieerd is, of realistische eigenschappen voor de onderlegplaatjes in laterale en longitudinale richting worden toegepast.

CONTENTS

Summary	i
Samenvatting	iii
1 Introduction	1
1.1 From wheel-rail contact to wheel-rail dynamic interaction	2
1.2 Review of studies on wheel-rail dynamic interaction with the explicit FEM	4
1.2.1 Impact contact	4
1.2.2 Flange contact	4
1.2.3 Track dynamic behaviour	4
1.2.4 Contact solutions and characteristics	5
1.3 Objective and outline of the present work	5
1.4 Novelty of the research	6
2 Algorithms of the explicit finite element analysis of wheel-rail dynamic interaction	9
2.1 Mathematical model of wheel-rail dynamic interactions	10
2.2 Numerical solution procedure for the explicit FE wheel-rail dynamic interaction analysis	12
2.2.1 Time discretisation by central difference scheme	12
2.2.2 Procedure for the explicit FE wheel-rail dynamic interaction analyses	13
2.2.3 Stability of integration	14
2.3 External force	15
2.3.1 Gravitational load	15
2.3.2 Hammer impulse	16
2.4 Internal force	16
2.5 Hourglass control	17
2.6 Contact algorithm	18
2.6.1 Normal contact	18

2.6.2 Tangential contact	20
2.6.3 Contact stability	21
2.7 Displacement constraints	21
2.8 Summary of the algorithms	21
3 Modelling procedure and solution analyses	23
3.1 Modelling of wheel and rail structures	24
3.1.1 Geometry modelling.....	24
3.1.2 Mesh.....	24
3.1.3 Modelling of other components and model parameters	25
3.2 Modelling of static contact	26
3.3 Modelling of dynamic interactions	27
3.3.1 Rolling contact pair	27
3.3.2 Initial conditions.....	28
3.3.3 Load boundary conditions	28
3.3.4 Displacement boundary conditions	30
3.3.5 Dynamic relaxation	30
3.3.6 Time step control.....	31
3.4 Obtain wheel-rail contact solutions	31
3.4.1 Contact patch area and stresses	31
3.4.2 Micro-slip distribution.....	33
3.4.3 Adhesion-slip distribution	34
3.5 Obtain structural dynamic responses	34
4 Numerical example 1: modelling of impact contact.....	35
4.1 Introduction of the wheel-rail impact at IRJs	36
4.2 Wheel-IRJ dynamic interaction model	38
4.2.1 Condition of the target IRJ	38
4.2.2 Wheel-IRJ dynamic interaction model	38
4.3 Validations of wheel & IRJ sub-models	41
4.3.1 Set-up of the hammer test.....	41
4.3.2 Calibration of the IRJ sub-model	43
4.3.3 Validation of transfer and cross-accelerances	44
4.3.4 Validation of decay rate	46
4.3.5 Validation of the wheel sub-model	48

4.4 Validation of pass-by vibration	49
4.5 Impact forces and contact solutions	50
4.5.1 Wheel-IRJ impact contact force	51
4.5.2 Evolution of contact areas and stresses distributions	53
4.5.3 Positive surface shear stress	56
4.5.4 Adhesion-slip distribution and micro-slip	57
4.6 Wave phenomena	59
4.6.1 Wave generated by wheel-rail contact	59
4.6.2 Wave excited by wheel-IRJ impact	61
4.7 Summary of the modelling of impact contact	62
5 Numerical example 2: squeal-exciting frictional rolling contact	65
5.1. Introduction of the friction-induced squeal.....	66
5.2. Wheel-rail dynamic interaction model with wheel lateral motion	67
5.3. Analyses of wheel-rail contact and dynamics results	69
5.3.1 Contact forces.....	69
5.3.2 Contact solutions	70
5.3.3 Wheel dynamic behaviour	75
5.4. Summary of the modelling of squeal-exciting frictional rolling contact	78
6 Numerical example 3: contact transition from single-point to two-point	81
6.1. Introduction of the wheel-rail two-point contact	82
6.2. Wheel-rail dynamic interaction model with contact transition	83
6.3. Solution of the contact model	84
6.3.1 Contact positions	85
6.3.2. Contact forces.....	86
6.3.3. Pressure and surface shear stress	87
6.3.4. Adhesion-slip distribution	90
6.3.5. Wheel-rail relative velocity	92
6.4. Summary of the modelling of wheel-rail contact transition.....	95
7 Dynamic-interaction-induced waves	97
7.1. Categorisation and generation mechanisms of the simulated waves	98
7.1.1 Impact-induced waves.....	98
7.1.2 Large-creepage-induced waves	99
7.1.3 Perturbation-induced waves	100

7.2. Type of the simulated waves	103
7.2.1 Preliminary inference of the wave type	103
7.2.2 Rayleigh surface waves	104
7.2.3 Nodal motion of the large-creepage-induced waves	105
7.3. Waves generated by a crack	107
7.4. Summary of the simulated waves	108
8 Conclusions and future research	111
8.1. Conclusions	112
8.2. Future research	113
References	115
Acknowledgements	127
Curriculum Vitae	129
List of Publications	130

1

INTRODUCTION

1.1 From wheel-rail contact to wheel-rail dynamic interaction

1

Wheel-rail contact is an issue of great concern in the railway research field. As a complex and imperfect link between wheel and rail (Iwnicki, 2006), it influences significantly the generation and development of wheel/rail defects, e.g., squats, head checks, rail gauge corner wear, corrugations, wheel burns and flats (Lundén & Paulsson, 2009), as well as the emission of wheel-rail noise including rolling noise, impact noise and squeal noise (Thompson, 2009). A study of wheel-rail contact may thus contribute to a more stable, comfortable and environmentally friendly railway transport.

Studies on wheel-rail contact date from the 19th century. Hertz (1882) was among the earliest researchers to provide an analytical solution to frictionless normal contact between elastic bodies with a half-space assumption. Mindlin (1949) developed the Hertz contact theory to treat shifts of contact bodies by a tangential force within its friction limit. Wheel-rail friction rolling contact was first studied by Carter (1926), who calculated creepage in the rolling direction with a 2D analytical model. Vermeulen and Johnson (1964) then extended Carter's 2D theory to 3D with pure creepage and without spin by assuming an elliptical adhesion area.

With the development of the computer and computational sciences, numerical methods have increasingly been employed in the study of wheel-rail contact, and these methods are believed to be more appropriate for solving wheel-rail rolling with high complexity in contact conditions and material properties (Damme *et al.*, 2003). The numerical methods may be divided into two classes (Nackenhurst, 2004): the boundary element method (BEM) for local analyses based on the half-space and quasi-quarter-space (Li, 2002) assumptions and the finite element method (FEM) for global analyses based on general continuum mechanics. Important contributions to the BEM solutions of wheel-rail frictional rolling contact with arbitrary creepage and spin were made by Kalker (1990), whose simplified and full theories have been implemented in the extensively used computer programs FASTSIM and CONTACT, respectively.

Since the BEM-based approaches discretise the surfaces of contact bodies in only the limited domain of potential contact areas (Fig. 1.1 (a)), they are restricted to linear elastic contact problems (Knothe *et al.*, 2001) and fail to consider the wheel/rail dynamic effects related to contact even in non-steady state contact solutions (Nackenhurst, 2004). Here, the dynamic effects denote that the inertia of wheel/rail material elements influences the stress field when the elements 'flow' through the deforming region (Johnson, 1985). Because the analytical methods and the BEM-based approaches only provide solutions of wheel-rail contact stress and motion (displacements & velocities) of bodies in contact within the contact region, the problems solved by them are known as wheel-rail contact problem.

In contrast to 'wheel-rail contact', the term 'wheel-rail interaction' used in this study denotes that the whole wheel and rail structures with certain geometric and material properties may contribute to and be influenced by wheel-rail contact solutions. The wheel-rail interaction problem can be solved by the FEM-based approaches with a discretisation of whole contact bodies; see Fig. 1.1 (b). FEM has been demonstrated to be a more flexible tool for modelling frictional rolling contact with arbitrary contact geometries, possible material nonlinearities, dissipation and bifurcations of solutions and corresponding standing-wave phenomena (Hu & Wriggers, 2002). Early finite element (FE) wheel-rail contact models have either assumed quasi-static state contact (Telliskivi & Olofsson, 2004; Sladkowski & Sitarz, 2005; Ekberg &

Sandström, 2009) or applied contact loads independently calculated by other simplified or multi-body dynamics models (Ringsberg, 2003; Wiest *et al.*, 2008b; Johansson *et al.*, 2011). Because the inertia of wheel/rail material elements is not involved in the contact calculation, these studies may not consider the dynamic effects related to contact.

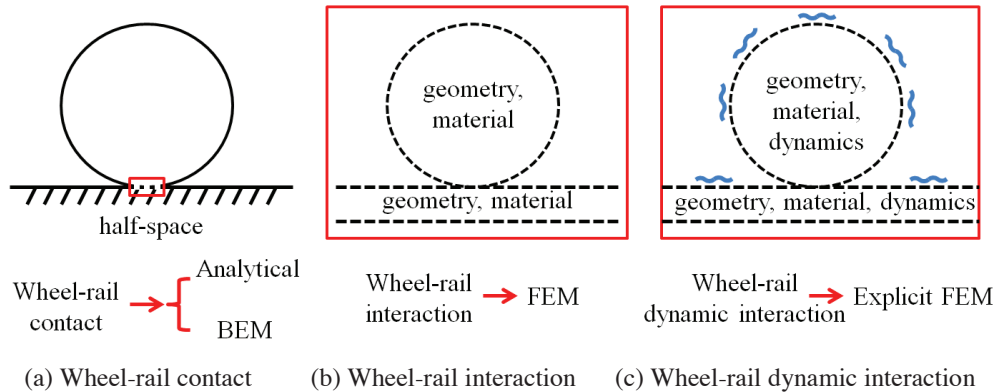


Figure. 1.1: From wheel-rail contact to dynamic interaction (Discretised solution regions are encircled with red frames)

When the contact of wheel and rail with the consideration of geometric and material properties interacts with their structural dynamic behaviour, the ‘wheel-rail dynamic interaction’ should be treated; see Fig. 1.1 (c). The dynamic effects cannot be neglected in the wheel-rail dynamic interaction problems such as wheel-rail impact contact, friction-induced unstable contact and non-steady-state transition of contact point. Note that in such contact situations, increased wear, rolling contact fatigue (RCF) and corrugation are expected (Chen *et al.*, 2010) and unpleasant impact and squeal noises may occur (Thompson, 2009). A better understanding and reliable modelling of wheel-rail dynamic interactions are hence important for the mitigation of wheel-rail deterioration and noise. Moreover, because the dynamic effects involved in wheel-rail interactions can be increased by wheel-rail high-speed rolling, a systematic study of wheel-rail dynamic interactions is highly desired within the context of booming high-speed railways.

Owing to the capabilities of handling nonlinear material properties and arbitrary contact geometries and considering dynamic effects, the explicit FEM has been proven to be suitable for tackling the problems of wheel-rail dynamic interactions. The explicit FEMs have been successfully applied to various nonlinear transient dynamics problems in recent decades (Wu & Gu, 2012) and widely implemented in commercial programs, e.g., LS-DYNA and ABAQUS/Explicit, Radios, etc. By avoiding the need for matrix evaluation, assembly and decomposition as required by the implicit integration algorithms, the explicit procedure is computationally attractive for analysing high-frequency dynamic problems of short-duration, especially when the total dynamic response time that must be modelled is only a few orders of magnitude longer than the stability critical time step, which is frequently the case in wave propagation analyses (Noh & Bathe, 2013). Moreover, in comparison with the implicit FEM, the explicit integration scheme is more robust in handling difficult contact problems because it avoids the convergence difficulties caused by demanding contact conditions (Mulvihill *et al.*,

2011) and the regularisation of the friction law required to treat the no-slip condition in the adhesion area (Wriggers, 2006).

1.2 Review of studies on wheel-rail dynamic interaction with the explicit FEM

Previous studies on wheel-rail dynamic interactions with the explicit FEM are primarily categorised into studies of wheel-rail impact contact (at rail joints, squats and crossing noses), flange contact, track dynamic behaviour, wheel-rail contact solutions and contact characteristics.

1.2.1 Impact contact

Wen *et al.* (2005) first applied the explicit FEM to calculate stresses and strains on the railhead with wheel-rail contact-impact behaviour at rail joint region. The explicit FE impact model was then developed by Cai *et al.* (2007) to calculate the dynamic impact force, stresses and strains when a wheel passes a rail joint with a height difference.

Li *et al.* (2008) applied the explicit FEM to investigate the generation mechanism of squat. Zhao *et al.* (2012) later used a validated 3D explicit FE model to evaluate the wheel-rail impact at a squat and the resulted high-frequency dynamic forces. Molodova *et al.* (2011) simulated axle box accelerations at a squat also using the explicit FEM. The simulated magnitude and frequency contents of the axle box accelerations agreed well with measurements. The simulation presented in (Molodova *et al.*, 2014) showed that the dynamic features of the ABA related to squats in the high frequency up to 2 kHz can be captured by the proposed explicit FE model.

Wiest *et al.* (2008a) investigated deformation and damage of a crossing nose with an explicit FE wheel-crossing nose dynamic interaction model. Pletz *et al.* (2012b) also presented an explicit FE model to simulate the process of a wheel passing the crossing panel of a turnout, which may consider the dynamic process, the elastic deformations of the wheel and the elastic-plastic deformations of the crossing. A 3D explicit FE model with the implementation of the nonlinear kinematic hardening material was then developed by Xin *et al.* (2016) to simulate the dynamic response of a whole wheelset while it is passing a crossing. Wei *et al.* (2017b) applied the explicit FEM to investigate wear and plastic deformation at railway crossings due to wheel-rail impacts. The simulated dynamic responses were validated by comparing with the in situ measurements of axle box acceleration.

1.2.2 Flange contact

The explicit FEM was also applied to the analysis of wear and RCF in the wheel curving behaviour with two-point contact (Vo *et al.*, 2015). The effects of the angle of attack (AoA) were considered, and the contact positions with certain AoAs and wheel/rail profiles could be determined. Another application of the explicit FEM to two-point contact was presented in (Chongyi *et al.*, 2010) to simulate the wear process on a laboratory twin-disc rig. Good agreement was achieved by comparing the simulated wear level with the experimental results.

1.2.3 Track dynamic behaviour

To model railway fastenings more realistically for the purpose of high-frequency dynamics between vehicle and track, Zhao *et al.* (2014a) developed different fastening models with the

explicit FEM to include the non-uniform pressure distribution and the constraints at the rail bottom. Oregui *et al.* (2015b) then presented a 3D explicit FE model with different fastening representations to investigate the influence of fastening models on the vertical dynamics of railway tracks with monoblock sleepers. A hammer test was reproduced by an explicit FE model in (Oregui *et al.*, 2016) to derive the stiffness and damping parameters involved in the track model.

1.2.4 Contact solutions and characteristics

Zhao and Li (2011) produced physical contact solutions of wheel-rail friction rolling with the explicit FEM. Wheel-rail contact was rigorously treated in their explicit FE models. The quasi-steady contact solutions obtained with the explicit FEM corresponded well to those obtained with well-established approaches, i.e., Hertz contact theory and CONTACT, in both the normal and tangential directions, whereas the explicit FE solutions were believed closer to the reality because the dynamic effects stemmed from the inherent vibration of wheel-rail rolling were perceived. Deng *et al.* (2015) later used explicit FEM to study the wheel-rail frictional rolling contact solutions with spin. The calculated explicit FE contact solutions have also been shown to be accurate via comparisons with Hertzian and CONTACT solutions.

Investigations of wheel-rail contact characteristics using the explicit FEM include the simulations of the transient wheel-rail rolling contact in elastoplasticity (Zhao & Li, 2015), in the presence of rail contamination (Zhao *et al.*, 2014b), under high and low adhesion conditions (Vo *et al.*, 2014), as well as with the consideration of velocity-dependent friction (Zhao & Li, 2016). These studies indicate that the explicit FEM is capable and suitable for the modelling of wheel-rail dynamic contact.

1.3 Objective and outline of the present work

Nevertheless, the aforementioned explicit FE studies have generally employed algorithm-optimised commercial programs, e.g., ANSYS/LS-DYNA or ABAQUS/Explicit, to efficiently process the large amounts of elements required in the detailed modelling of wheel/track structures and perform time integration with small time steps. To facilitate other researchers to perform simulations of wheel-rail dynamic interactions with such software or alternative explicit FEM programs, systematic perceptions of the involved algorithms and modelling know-how should be provided. This thesis in Chapter 2 systematically explores the core algorithms employed in the explicit FE wheel-rail interaction analyses, mainly the mathematical model and numerical solution procedure implemented in the solvers of commercial programs. Chapter 2 also theoretically demonstrates that the explicit FEM is an ideal approach for modelling wheel-rail dynamic interactions by fully coupling the calculation of wheel-rail frictional rolling contact with the calculation of high-frequency dynamic responses of wheel and rail structures. To promote the broad use of the method, Chapter 3 proposes detailed procedures for establishing robust explicit FE wheel-rail dynamic interaction models (pre-processing) and converting outputs into wheel-rail contact and dynamics solutions (post-processing).

Chapters 4~6 then present three typical numerical examples of modelling of wheel-rail dynamic interactions: wheel-rail impact at an insulated rail joint (IRJ), wheel-rail contact with unsteady lateral creepage and contact transition from single-point contact to two-point contact. Taking arbitrary contact geometries, nonlinear material properties and dynamic effects into

consideration, the presented numerical examples further demonstrate that the explicit FEM is appropriate and reliable for the wheel-rail dynamic interaction analyses.

Regular wave patterns that indicate wave generation, propagation and reflection are produced by the explicit FE simulations presented in Chapters 4~6. Chapter 7 summarises and categorises the simulated dynamic-interaction-induced waves, and investigates the generation mechanisms and types of the simulated waves. Chapter 8 presents the concluding remarks and discusses potential improvements in the methodology required to address controversial issues related to wheel-rail dynamic interactions, such as squeal and corrugation. The outline of this thesis is summarised in Fig. 1.2.

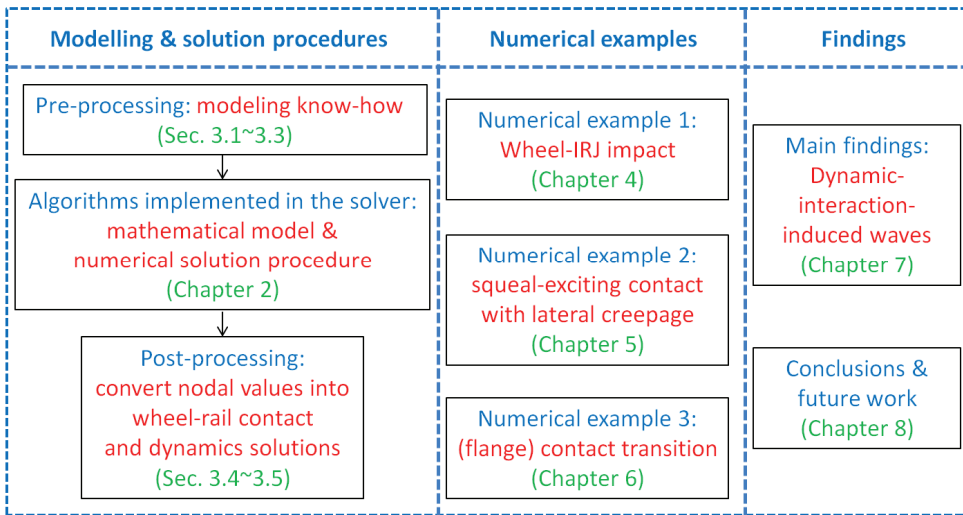


Figure. 1.2: Outline of the thesis

1.4 Novelty of the research

The novelty of this thesis mainly includes three aspects: 1. the exploration of the methodology, 2. the modelling approach and 3. the findings.

Firstly, this thesis systematically explores the methodology of the explicit FEM dedicated to the analysis of wheel-rail dynamic interactions. On one hand, the illustrations of the numerical model and the solution procedure lead to a better understanding of the modelling of wheel-rail dynamic interactions with the explicit FEM; on the other hand, on the basis of the explored numerical solution procedure, an indirect method for validating the dynamic contact solution is proposed, as shown in Fig. 1.3. Because the explicit FEM may fully couple the calculation of wheel/rail dynamic responses with the calculation of wheel-rail contact (see later in Table 2.1), the reliability of the wheel-rail dynamic interaction solutions may be confirmed by separately validating the quasi-steady contact solutions and wheel/rail dynamic responses. The former part has been accomplished by the aforementioned studies (Zhao & Li, 2011; Deng *et al.*, 2015), whereas the abilities of the method to reproduce wheel/track dynamic behaviour have been reported in (Molodova *et al.*, 2011; Molodova *et al.*, 2014; Oregui *et al.*, 2015b; Oregui *et al.*, 2016; Wei *et al.*, 2017b; Yang *et al.*, 2018).

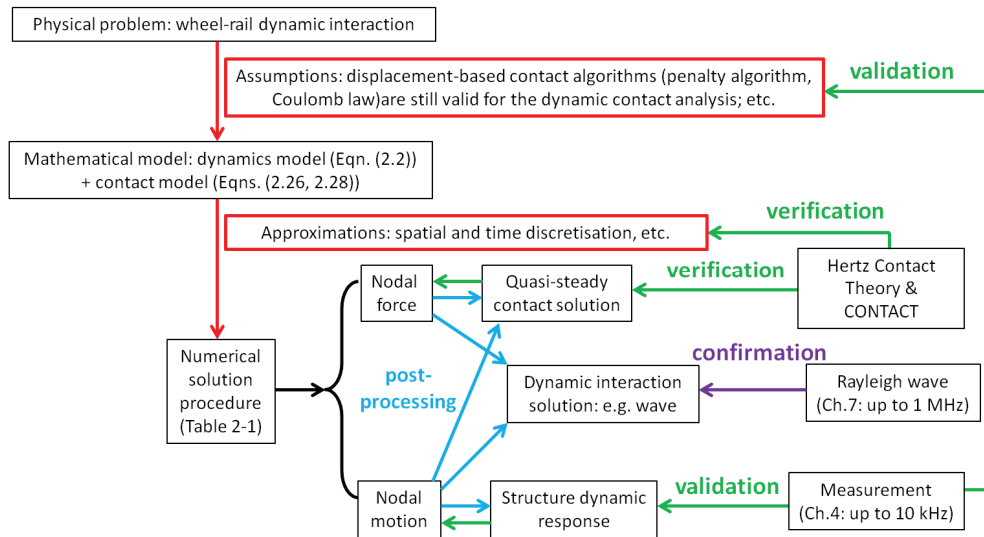


Figure. 1.3: Indirect validation of the dynamic contact solution

Fig. 1.3 indicates that as long as the quasi-steady-state contact solution and the structural dynamic responses are verified and validated, the nodal force and nodal motion calculated by the explicit FEM can be considered reliable. The dynamic interaction solutions obtained by post-processing the calculated nodal force and motion are hence validated indirectly. Simultaneously, the physical problem can be considered to be appropriately represented by the mathematical model and the errors caused by the numerical approximations are regarded as acceptable.

Secondly, this thesis robustly models wheel-rail dynamic interactions under three typically non-steady-state contact conditions: impact contact, contact with unsteady lateral creepage and contact transition from single-point to two-point. Taking into account real contact geometries, nonlinear material properties and dynamic effects, the presented numerical examples further demonstrate that the explicit FEM is appropriate and reliable for the analysis of wheel-rail dynamic interactions.

The first numerical example presents an explicit FE wheel-insulated rail joint (IRJ) dynamic interaction model (see Fig. 1.4 (a)), which is comprehensively validated against a hammer test and a pass-by measurement conducted on a typical IRJ in the Dutch railway. This numerical example provides an overall understanding of the wheel-rail dynamic contact behaviour due to impacts by calculating transient frictional impact contact solutions.

The second numerical example proposes an explicit FE wheel-rail dynamic interaction model with wheel lateral motion (Fig. 1.4 (b)) to investigate wheel-rail squeal-exciting contact with the involvement of dynamic effects, unsteady lateral creepage and velocity-dependent friction. The proposed model is considered to be capable of reproducing the two commonly considered mechanisms leading to wheel squeal noise: falling-friction and mode-coupling. This numerical example contributes to a better understanding and modelling of frictional instability and consequent wheel squeal from the perspective of wheel-rail dynamic contact.

The third numerical example uses an explicit FE model to simulate the non-steady-state transition of wheel-rail rolling from single-point to two-point contact (Fig. 1.4 (c)). This numerical example develops the understanding of wheel-rail frictional rolling with two-point contact and its resulting wear (including fretting) and RCF, and may contribute to the study of the 'elusive' short-pitch corrugation and 'erratic' flange squeal.

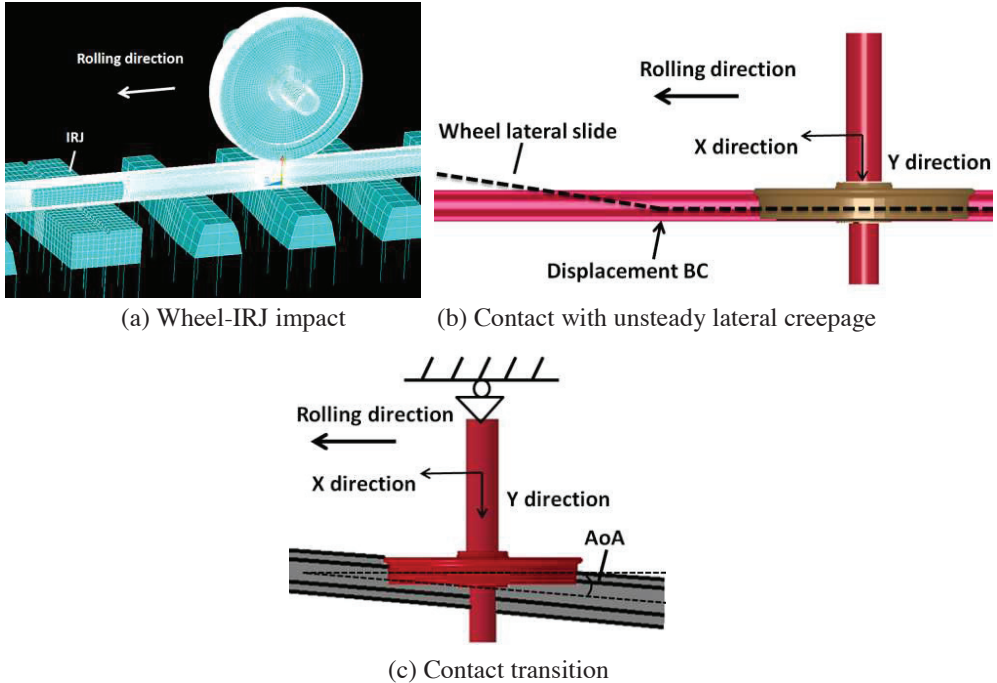


Figure. 1.4: Numerical examples presented in Chapters 4~6

Thirdly, this thesis reveals wave phenomena caused by wheel-rail dynamic interactions. To the knowledge of the author, the time-domain wave, as a typical dynamic contact solution, has rarely been reported in the previous researches of wheel-rail contact. The reproduction of the large-creepage-induced Rayleigh wave confirms the reliability of explicit FEM for the calculation of high-frequency wheel-rail dynamic interactions (see Fig. 1.3). In addition, the perturbation-induced wave is considered to be related to the occurrence of stick-slip rolling, which might subsequently result in squeal and corrugation.

2

ALGORITHMS OF THE EXPLICIT FINITE ELEMENT ANALYSIS OF WHEEL-RAIL DYNAMIC INTERACTION

This chapter systematically explores the core algorithms employed in the explicit FE wheel-rail interaction analyses with a focus on the mathematical model and the numerical solution procedure implemented in the solvers of commercial programs. The reviews of the algorithms are mainly based on the theories illustrated in several FEM books (Bathe, 1996; Wriggers, 2006; Wu & Gu, 2012) and articles (Hughes *et al.*, 1976; Oden & Pires, 1984; Hallquist *et al.*, 1985; Wu, 2003, 2009) and the theoretical manuals of commercial explicit FE programs (Hibbitt & Sorensen, 2001; Sarl, 2005; Hallquist, 2006). In addition, the applicability of the explicit FEM to wheel-rail dynamic interaction analyses is demonstrated from a theoretical perspective.

In the formulas presented in this thesis, vectors, matrices and tensors are mainly represented by index notation, and sometimes by bold-faced variables when the numbers of components and operations are not confusing. Lowercase subscripts (i, j, k) are used for spatial components, lowercase superscripts (t) for time points, capital subscripts (M) for hourglass mode numbers, and capital superscripts (J, M, N) for nodal/element numbers.

2.1 Mathematical model of wheel-rail dynamic interactions

Lagrangian formulation typically used for transient structural dynamic problems is employed for wheel-rail dynamic interaction analyses. When adopting the Lagrangian formulation, the time-dependent displacement u_i in a fixed rectangular Cartesian coordinate system can be expressed in terms of the convected coordinates x_k in the same coordinate system and time t as follows:

$$u_i = u_i(x_k, t) \quad i, k = 1, 2, 3 \quad (2.1)$$

A general 3D transient structural dynamics problem may then be described by constrained partial difference governing equations as follows:

$$\text{Momentum conservation equations:} \quad \sigma_{ij,j} + \rho f_i = \rho \dot{u}_i \quad \text{in } \Omega \quad i, j = 1, 2, 3 \quad (2.2a)$$

$$\text{Displacement boundary conditions:} \quad u_i = D_i \quad \text{on } \Gamma_u \quad (2.2b)$$

$$\text{Traction boundary conditions:} \quad \sigma_{ij} n_j = T_i \quad \text{on } \Gamma_s \quad (2.2c)$$

$$\text{Contact discontinuity conditions:} \quad (\sigma_{ij}^+ - \sigma_{ij}^-) n_i = 0 \quad \text{on } \Gamma_c \quad (2.2d)$$

$$\text{Initial conditions:} \quad u_i(x_k, 0) = U_i(x_k), \quad \dot{u}_i(x_k, 0) = V_i(x_k) \quad \text{in } \Omega \quad (2.2e)$$

$$\text{Material constitutive relation:} \quad \dot{\sigma}_{ij} = \dot{\sigma}_{ij}(E, \nu, E_t, x_i, u_i, \dot{\epsilon}_{ij}, \dots) \quad (2.2f)$$

$$\text{Strain-displacement relation:} \quad \epsilon_{ij} = (\dot{u}_{i,j} + \dot{u}_{j,i})/2 \quad (2.2g)$$

where σ_{ij} is Cauchy stress tensor; ρ is the current density; f_i is the body force density; D_i is the prescribed displacement boundary conditions on part of the boundary Γ_u ; T_i represents the components of the traction boundary conditions on part of the boundary Γ_s ; n_i is a unit outwardly normal to a boundary element on Γ ; U_i and V_i are the initial displacements and velocities, respectively; and E, ν and E_t are the Young's modulus, Poisson's ratio and tangent modulus of the material, respectively. The rate form adopted in Eqns. (2.2f) and (2.2g) may take nonlinearities into account.

The displacement-based FEM (compared with the force-based FEM) is employed to solve the dynamic problem described in Eqn. (2.2). By removing all displacement constraints and

assuming that the reactions are known, the variational governing equation can be derived by Hamilton's principle as follows:

$$\int_{\Omega} (\rho \ddot{u}_i - \sigma_{ij,j} - \rho f_i) \delta u_i d\Omega + \int_{\Gamma_s} (\sigma_{ij} n_j - T_i) \delta u_i d\Gamma + \int_{\Gamma_c} (\sigma_{ij}^+ - \sigma_{ij}^-) n_j \delta u_i d\Gamma = 0 \quad (2.3)$$

Eqn. (2.3) is a statement of the principle of virtual work, in which δu_i is the variation of displacement. By applying the Gauss divergence theorem to convert the surface integral to the volume integral, the following is obtained:

$$\int_{\Omega} (\sigma_{ij} \delta u_{i,j}) d\Omega = \int_{\Gamma_s} (\sigma_{ij} n_j) \delta u_i ds + \int_{\Gamma_c} (\sigma_{ij}^+ - \sigma_{ij}^-) n_j \delta u_i d\Gamma \quad (2.4)$$

Noting the mathematical identity:

$$(\sigma_{ij} \delta u_{i,j})_{,j} = \sigma_{ij,j} \delta u_i + \sigma_{ij} \delta u_{i,j} \quad (2.5)$$

Then, the weak form of the equilibrium equation can be derived as follows:

$$\int_{\Omega} \rho \ddot{u}_i \delta u_i d\Omega + \int_{\Omega} \sigma_{ij} \delta u_{i,j} d\Omega = \int_{\Omega} \rho f_i \delta u_i d\Omega + \int_{\Gamma_s} T_i \delta u_i d\Gamma \quad (2.6)$$

To solve Eqn. (2.6) numerically, a spatial discretisation may be used to express the equilibrium equation in terms of time-dependent nodal unknowns and base functions. A mesh of finite elements interconnected at nodal points on the reference configuration is thus superimposed, and particles are tracked through time:

$$u_i = u_i(x_k(\xi, \eta, \zeta), t) = \sum_{N=1}^n \varphi^N(\xi, \eta, \zeta) u_i^N(t) \quad i, k = 1, 2, 3 \quad (2.7)$$

where φ^N is the shape function in the parametric coordinates (ξ, η, ζ) and n is the number of nodal points defining the element. Summing over all m elements of a FE model, the semi-discrete equation of motion in the matrix notation becomes:

$$\sum_{M=1}^m \left(\int_{\Omega_e} \rho \mathbf{N}^T \mathbf{N} \ddot{\mathbf{u}} d\Omega + \int_{\Omega_e} \mathbf{B}^T \boldsymbol{\sigma} d\Omega - \int_{\Omega_e} \rho \mathbf{N}^T \mathbf{f} d\Omega - \int_{\Gamma_{s,e}} \mathbf{N}^T \mathbf{t} d\Gamma \right)^M = 0 \quad (2.8)$$

where $\boldsymbol{\sigma}$ is the Cauchy stress vector, and $\boldsymbol{\sigma}^T = (\sigma_{xx}, \sigma_{yy}, \sigma_{zz}, \sigma_{xy}, \sigma_{yz}, \sigma_{zx})$; $\ddot{\mathbf{u}}$ is the nodal acceleration vector; \mathbf{N} is the shape matrix constructed by the shape functions; \mathbf{B} is the strain-displacement matrix containing the first spatial derivatives of the shape functions; and \mathbf{f} and \mathbf{t} are the prescribed body load vector and traction load vector, respectively. Because the hexahedral solid elements ($n=8$ in Eqn. (2.7)) are mostly used in explicit FE wheel-rail interaction models, they are taken as examples to illustrate the theories summarised here. For the hexahedral elements:

$$\mathbf{N}(\xi, \eta, \zeta) = \begin{bmatrix} \varphi^1 & \varphi^2 & \dots & \dots & \dots & \dots & \dots & \dots \\ \varphi^1 & \varphi^1 & \varphi^2 & \dots & \varphi^8 & \dots & \dots & \dots \\ \varphi^1 & \varphi^1 & \dots & \dots & \dots & \dots & \dots & \varphi^8 \end{bmatrix} \quad (2.8a)$$

$$\varphi^N(\xi, \eta, \zeta) = \frac{1}{8} (1 + \xi \xi^N) (1 + \eta \eta^N) (1 + \zeta \zeta^N) \quad N = 1, 2, \dots, 8 \quad (2.8b)$$

$$\mathbf{B}(\xi, \eta, \zeta) = \begin{bmatrix} \frac{\partial}{\partial x} & & & & & \\ & \frac{\partial}{\partial y} & & & & \\ & & \frac{\partial}{\partial z} & & & \\ \frac{\partial}{\partial y} & \frac{\partial}{\partial x} & & & & \\ & & \frac{\partial}{\partial z} & \frac{\partial}{\partial y} & & \\ \frac{\partial}{\partial z} & & & & \frac{\partial}{\partial x} & \end{bmatrix} \mathbf{N}(\xi, \eta, \zeta) \quad (2.8c)$$

Note that the time dimension in Eqn. (2.8) is still continuous, and the semi-discrete equation of motion for a general transient structural dynamics problem may thus be rewritten in a shorthand format:

$$\mathbf{M}\ddot{\mathbf{u}} = \mathbf{f}_{\text{ext}} - \mathbf{f}_{\text{int}} \quad (2.9)$$

in which \mathbf{M} , \mathbf{f}_{int} and \mathbf{f}_{ext} are the mass matrix, internal force vector and external force vector, respectively, and they are defined as follows:

$$\mathbf{M} = \sum_{M=1}^m \left(\int_{\Omega_e} \rho \mathbf{N}^T \mathbf{N} d\Omega \right)^M \quad (2.9a)$$

$$\mathbf{f}_{\text{ext}} = \sum_{M=1}^m \left(\int_{\Omega_e} \rho \mathbf{N}^T \mathbf{f} d\Omega + \int_{\Gamma_{s,e}} \mathbf{N}^T \mathbf{t} d\Gamma \right)^M \quad (2.9b)$$

$$\mathbf{f}_{\text{int}} = \sum_{M=1}^m \left(\int_{\Omega_e} \mathbf{B}^T \boldsymbol{\sigma} d\Omega \right)^M \quad (2.9c)$$

By adding two extra terms, \mathbf{f}_{con} and \mathbf{H} , to the right-hand side of Eqn. (2.9), the semi-discrete equilibrium equation for the wheel-rail dynamic interaction problem is obtained as follows:

$$\mathbf{M}\ddot{\mathbf{u}} = \mathbf{f}_{\text{ext}} - \mathbf{f}_{\text{int}} + \mathbf{H} + \mathbf{f}_{\text{con}} \quad (2.10)$$

where \mathbf{H} is the anti-hourglass vector that only occurs in the reduced integration to control the zero-energy modes, and \mathbf{f}_{con} is the contact force vector, which can be included as a contribution to the externally applied tractions (Bathe, 1996; Wu & Gu, 2012). These two terms will be explicated in Sections 2.5 and 2.6, respectively.

2.2 Numerical solution procedure for the explicit FE wheel-rail dynamic interaction analysis

2.2.1 Time discretisation by central difference scheme

Among the various numerical approaches developed for solving the dynamic interaction problem formulated by Eqn. (2.10), this study focuses only on the explicit integration scheme using the central difference to approximate the acceleration vector $\ddot{\mathbf{u}}$. The explicit schemes calculate the values of dynamic quantities at time step $t + 1$ based entirely on the available

values at time step t . Eqn. (2.10) discretised by the central difference scheme at time step t may be written as follows:

$$\ddot{\mathbf{u}}^t = \mathbf{M}^{-1}(\mathbf{f}_{\text{ext}}^t - \mathbf{f}_{\text{int}}^t + \mathbf{H}^t + \mathbf{f}_{\text{con}}^t) \quad (2.11)$$

The velocity and displacement vectors may then be obtained using the central difference time integration:

$$\dot{\mathbf{u}}^{t+1/2} = \dot{\mathbf{u}}^{t-1/2} + \Delta t^{t+1/2} \ddot{\mathbf{u}}^t \quad (2.12a)$$

$$\mathbf{u}^{t+1} = \mathbf{u}^t + \Delta t^{t+1} \dot{\mathbf{u}}^{t+1/2} \quad (2.12b)$$

where Δt is the time step size, which is constant in the linear analysis but may vary in the nonlinear analysis (Bathe, 1996), and

$$\Delta t^{t+1/2} = \frac{\Delta t^{t+1} + \Delta t^t}{2} \quad (2.13)$$

2.2.2 Procedure for the explicit FE wheel-rail dynamic interaction analyses

The equilibrium Eqn. (2.11) discretised in both the space and time domains indicates that the numerical solutions of a wheel-rail dynamic interaction problem are dependent on a constant mass matrix and four time-dependent force vectors. Therefore, the numerical solution procedure for the explicit FE wheel-rail dynamic interaction analysis is mainly composed of mass matrix and force vector calculations. A lumped mass matrix can be constructed by a row summation scheme (Wu, 2006) prior to the iteration to promote the efficiency and practicality of the explicit FEM. For the force vectors, the external force vector \mathbf{f}_{ext} may be calculated directly by the given load conditions (see Section 2.3); the internal force vector \mathbf{f}_{int} contributed by stresses may be calculated by the constitutive and strain-displacement formulations built in the element and material models (see Section 2.4); and the anti-hourglass force vector \mathbf{H} and the contact force vector \mathbf{f}_{con} may be calculated by the Flanagan-Belytschko scheme (Flanagan & Belytschko, 1981) (see Section 2.5) and penalty contact method (Hallquist *et al.*, 1985) (see Section 2.6), respectively. Table 2.1 outlines a numerical procedure for the explicit FE wheel-rail dynamic interaction analysis. This procedure has been implemented in commercial explicit FE programs and used in previous wheel-rail contact and dynamics studies, although variations are possible, e.g., processing contact with a ‘predictor-corrector method’ (Attaway *et al.*, 1998; Wu, 2009): 1. Predict nodal accelerations/velocities/displacements before step (d) in Table 2.1 by assuming no contact occurs; 2. Check the contact conditions in step (d) with the predicted displacement field; and 3. Enforce contact forces and correct the nodal motions, i.e., the acceleration, velocity and displacement.

The numerical solution procedure presented in Table 2.1 contains two loops. The outer loop is constructed mainly by formulating the equation of motion and solving the equation with the central difference scheme, whereas the inner loop calculates the wheel-rail contact, which is called as a subroutine at each time step prior to the updates of the structural dynamic responses. The calculation of wheel/rail dynamics and the calculation of wheel-rail contact are, therefore, coupled in the numerical algorithm, which provides the theoretical basis for the indirect validation of the wheel-rail dynamic interaction solutions mentioned in Section 1.4.

Table 2.1: Numerical procedure for the explicit FE wheel-rail dynamic interaction analysis

Initialise algorithm:

- Apply initial conditions U_i and V_i (by Eqn. (2.2e));
- Set $\dot{\mathbf{u}}^{-1/2} = \dot{\mathbf{u}}^0 = \dot{\mathbf{u}}_i(x_k, 0) = V_i(x_k)$ and $\Delta t^0 = 0$;
- Define the slave/master nodes/segments for wheel-rail contact pairs;
- Construct the lumped mass matrix \mathbf{M} ;
- Set the termination time: T_{ter} .

LOOP1 $t = 0, 2, \dots, n$ (time step number)

- (a) Apply load conditions to construct the external force vector \mathbf{f}_{ext}^t (see Section 2.3);
- (b) Process elements to construct the internal force vector \mathbf{f}_{int}^t (see Section 2.4);
- (c) Construct the anti-hourglass vector \mathbf{H}^t (see Section 2.5);
- (d) Construct the wheel-rail contact force vector \mathbf{f}_{con}^t (see Section 2.6);

LOOP2 $N=1, 2, \dots, m$ (slave wheel node number)

- I. Locate the corresponding master segment on the rail for slave wheel node N ;
- II. Locate the wheel-rail contact point (projection of the slave node on the master segment);
- III. Check for penetration;

IF penetration occurs,

- i. Calculate the normal contact forces \mathbf{f}_{cN}^t ;
- ii. Calculate the tangential contact forces \mathbf{f}_{cT}^t ;

END IF

END LOOP2

- (e) Update time step size Δt^{t+1} to prevent unstable contact or integration (see Section 2.2.3);
- (f) Update nodal accelerations $\ddot{\mathbf{u}}^t$ (by Eqn. (2.11));
- (g) Impose displacement constraints (see Section 2.7);
- (h) Update nodal velocities $\dot{\mathbf{u}}^{t+1/2}$ (by Eqn. (2.12a));
- (i) Update nodal displacements \mathbf{u}^{t+1} (by Eqn. (2.12b));
- (j) Update structural geometries (by Eqn. (2.15));
- (k) Update time $\sum_{t+1} \Delta t$ and check for termination: **IF** $\sum_{t+1} \Delta t \geq T_{ter} \rightarrow \text{STOP}$

END LOOP1

Output: wheel/rail nodal force and nodal motion ($\ddot{\mathbf{u}}$, $\dot{\mathbf{u}}$ and \mathbf{u})

2.2.3 Stability of integration

The explicit integration scheme has a simple and neat solution procedure but is conditionally stable: the integration is only stable if the time step size used is smaller than the critical time step size. The Courant-Friedrichs-Lewy stability condition (Courant *et al.*, 1967)

can be used to guarantee convergence, which requires that a sound wave may not cross the smallest element within one time step:

$$\Delta t_c \leq L_c / C_d \quad (2.14)$$

where Δt_c is the critical time step size; L_c is the shortest characteristic dimension of the element; and C_d is the dilatational wave speed of the material. For hexahedral elements:

$$L_c = V_e / A_{emax} \quad (2.14a)$$

where V_e is the element volume, and A_{emax} is the largest surface area. For elastic materials:

$$C_d = \sqrt{E(1-\nu)/[(1+\nu)(1-2\nu)\rho]} \quad (2.14b)$$

In the calculation of wheel-rail interactions, the wheel and rail are generally considered to be steel with nominal values of $E=210$ GPa, $\nu = 0.3$ and $\rho=7800$ kg/m³; thus, C_d is equal to approximately 6 km/s. The critical time step Δt_c characterised in inequality (2.14) may vary in nonlinear dynamic analyses because of changes in the material parameters and/or geometry. The time step Δt should be correspondingly adjusted in a conservative manner so that the condition in inequality (2.14) is satisfied with certainty at all time steps. To guarantee the stability and simultaneously decrease the solution time, a suitable scale factor sf may be employed to control the time step, i.e., $\Delta t = sf \times L_c / C_d$. A detailed discussion about the scale factor sf used in the wheel-rail dynamic interaction analysis is given in Section 3.3.6.

Because the numerically obtained highest natural frequency of a structure is bounded by the highest frequency of any individual element in the FE discretisation (Hallquist, 2006), as long as the elements and time steps are sufficiently small, an explicit FE model may include in its solution all the relevant vibration modes of structures and continua and associated wave propagations (Zhao & Li, 2015). In addition, small time step sizes can reduce the truncation errors but increase the round-off errors. By adding displacement increments to the initial geometries:

$$\mathbf{x}^t = \mathbf{x}^0 + \mathbf{u}^t \quad (2.15)$$

in the geometry updating step (step (j) in Table 2.1), rather than to the geometries obtained at the previous time step, solutions turn out to be much less sensitive to the round-off errors (Hallquist, 2006).

2.3 External force

The external force vector in Eqn. (2.11) can be directly constructed by the prescribed load conditions. Common external loads applied to wheel-rail dynamics and contact models include gravitational loads, hammer impulse loads and driving torques. The first two may be regarded as the body forces and surface nodal loads contributing to the first and second terms of Eqn. (2.9b), respectively. The driving torque is discussed in Section 3.3.3.

2.3.1 Gravitational load

Gravitational loads are generally applied to wheel-rail interaction models to initialise internal forces before proceeding with calculations of dynamic responses. The gravitational loads are applied as body forces by setting a fixed gravitational acceleration g as follows:

$$\mathbf{f}_{\text{grav}} = \sum_{M=1}^m \left(\int_{\Omega_e} \rho \mathbf{N}^T \mathbf{f} d\Omega \right)^M = \sum_{M=1}^m \left(\int_{\Omega_e} \rho \mathbf{N}^T \mathbf{N} g d\Omega \right)^M = \mathbf{M}g \quad (2.16)$$

2.3.2 Hammer impulse

Hammer impulses may be applied to the explicit FE wheel/track models as surface nodal loads to characterise the dynamic behaviour of structures (Oregui *et al.*, 2015; Oregui *et al.*, 2016). The prescribed surface nodal loads at the N th node of a surface segment p^N may be converted to the traction boundary conditions as follows:

$$\mathbf{t} = t_i(\xi, \eta) = n_i \sum_{N=1}^4 \varphi^N(\xi, \eta) p^N \quad i = 1, 2, 3 \quad (2.17)$$

where n_i is the unit normal vector to the surface segment; see Eqn. (2.26b) in Section 2.6.1. A Gaussian one-point quadrature may then be used to conduct the surface integration in Eqn. (2.9b) as follows:

$$\int_{\Gamma_{s,e}} \mathbf{N}^T \mathbf{t} d\Gamma = \int_{-1}^1 \int_{-1}^1 \mathbf{N}^T \mathbf{t}(\xi, \eta) |\mathbf{J}| d\xi d\eta = 4\mathbf{N}^T \mathbf{t}(0,0) |\mathbf{J}(0,0)| \quad (2.18)$$

in which \mathbf{J} is the surface Jacobian matrix and $4|\mathbf{J}(0,0)|$ approximates the element surface.

2.4 Internal force

To construct the internal force vector given in Eqn. (2.9c), the strain-displacement matrix \mathbf{B} and the stress vector $\boldsymbol{\sigma}$ are required. Continuing to take the hexahedral element as examples, the Jacobian matrix \mathbf{J} is used to relate the displacement in the parametric coordinate system to the global coordinates system:

$$\begin{bmatrix} \frac{\partial \varphi^N}{\partial x} \\ \frac{\partial \varphi^N}{\partial y} \\ \frac{\partial \varphi^N}{\partial z} \end{bmatrix} = \mathbf{J}^{-1} \begin{bmatrix} \frac{\partial \varphi^N}{\partial \xi} \\ \frac{\partial \varphi^N}{\partial \eta} \\ \frac{\partial \varphi^N}{\partial \zeta} \end{bmatrix} \quad N = 1, 2, \dots, 8 \quad (2.19)$$

The strain-displacement matrix \mathbf{B} may then be obtained with Eqn. (2.8c), and the strain rate $\dot{\boldsymbol{\epsilon}}$ and stress rate $\dot{\boldsymbol{\sigma}}$ are readily calculated by applying the strain-displacement relation and the material constitutive relation in Eqns. (2.2g) and (2.2f), respectively. The material constitutive relation expressed in Eqn. (2.2f) can be either linear or nonlinear. See (Wu & Gu, 2012) for an additional discussion of the material constitutive relations. The Cauchy stresses may be calculated using explicit time integration as follows:

$$\boldsymbol{\sigma}(t + \Delta t) = \boldsymbol{\sigma}(t) + \dot{\boldsymbol{\sigma}}\Delta t \quad (2.20)$$

Because $\mathbf{G}(\xi, \eta, \zeta) = \mathbf{B}^T \boldsymbol{\sigma}$ is defined over the volume, the internal forces of structures may be updated with a Gaussian one-point quadrature analogous to Eqn. (2.18) as follows:

$$\int_{\Omega_e} \mathbf{G}(\xi, \eta, \zeta) d\Omega = 8\mathbf{G}(0,0,0) |\mathbf{J}(0,0,0)| \quad (2.21)$$

in which $8|J(0,0,0)|$ approximates the element volume.

2.5 Hourglass control

Explicit FE wheel-rail interaction analyses have generally adopted the one-point quadrature scheme (Eqns. (2.18) and (2.21)) for the sake of computational efficiency, which may also avoid the shear locking issue. The one-point reduced integration, however, leads to spurious zero-energy modes or ‘hourglass’ modes for hexahedral and quadrilateral elements. For hexahedral elements, the hourglass modes are present whenever diagonally opposite nodes have identical velocities, which give zero strain rates according to Eqn. (2.2g). The anti-hourglass force vector \mathbf{H} is thus introduced in Eqn. (2.10) to avoid the undesirable hourglass modes from growing large and destroying solutions. An orthogonal Flanagan-Belytschko hourglass control scheme (Flanagan & Belytschko, 1981) may be used in the explicit FE wheel-rail dynamic interaction analysis. The anti-hourglass forces are given by:

$$\mathbf{H} = f_{iM}^N = \frac{1}{4} Q_{hg} \rho C_d V_e^{\frac{2}{3}} \sum_{N=1}^8 (\dot{u}_i \gamma_M)^N \gamma_M^N \quad i = 1,2,3; M = 1,2,3,4 \quad (2.22)$$

where Q_{hg} is the hourglass coefficient, and the nodal velocities \dot{u}_i^N are the sum of the hourglass field $\dot{\mathbf{u}}_{HG}^N$ and the linear portion of the nodal velocities $\dot{\mathbf{u}}_{LIN}^N$:

$$\dot{u}_i^N = \dot{\mathbf{u}}^N = \dot{\mathbf{u}}_{HG}^N + \dot{\mathbf{u}}_{LIN}^N \quad (2.22a)$$

The hourglass shape vectors γ_M^N are defined in terms of the hourglass base vectors Γ_M^N given in Table 2.2:

$$\gamma_M^N = \Gamma_M^N - \varphi_i^N \sum_{N=1}^8 \dot{u}_i^N \Gamma_M^N \quad (2.22b)$$

Table 2.2. Hourglass base vectors for hexahedral elements

Node (N)	Γ_1^N	Γ_2^N	Γ_3^N	Γ_4^N
1	1	1	1	-1
2	1	-1	-1	1
3	-1	-1	1	-1
4	-1	1	-1	1
5	-1	-1	1	1
6	-1	1	-1	-1
7	1	1	1	1
8	1	-1	-1	-1

Note that the hourglass shape vectors γ_M^N are orthogonal to the linear velocity field $\dot{\mathbf{u}}_{LIN}^N$, which makes the anti-hourglass force vector f_{iM}^N also orthogonal to the linear velocity field $\dot{\mathbf{u}}_{LIN}^N$ and is necessary for accurately detecting an hourglass. Therefore, the hourglass control scheme avoids transferring energy to or from the rigid body and uniform strain modes.

2.6 Contact algorithm

Because of its iterative nature (Bathe, 1996; Wu & Gu, 2012), the penalty contact algorithm is considered to be suitable for solving explicit FE contact problems and has been broadly proposed to enforce the wheel-rail contact constraints. As indicated in Table 2.1, the penalty contact algorithm can be straightforwardly implemented in the explicit FE programs as a subroutine. Penetration is allowed and represents the key to the penalty method (Wu & Gu, 2012). The penalty algorithm checks each slave node for penetration through the master surface. This study refers to the wheel surface as the slave surface and to the rail surface as the master surface; the symmetry of the approach eliminates any bias in this choice.

2.6.1 Normal contact

In a wheel-rail contact simulation, a slave wheel node is seldom in exact contact with a master rail node. Instead, the slave wheel node usually ‘contacts’ a segment composed of four rail surface nodes. At each time step, the contact segments on the rail surface need to be searched for. For an arbitrary slave node N_s defined on the prospective wheel contact surface, the closest master node and segment on the rail surface need to be first located. As shown schematically in Fig. 2.1 (a), the slave node N_s is denoted as a red spot, and its closest master node N_m is stored by segments S_i ($i=1,2,3,4$). If the nodes N_s and N_m do not coincide, N_s can be shown to lie in one of the segments S_i via the following tests:

$$(\mathbf{c}_i \times \mathbf{s}) \cdot (\mathbf{c}_i \times \mathbf{c}_{i+1}) > 0 \quad , \quad (\mathbf{c}_i \times \mathbf{s}) \cdot (\mathbf{s} \times \mathbf{c}_{i+1}) > 0 \quad i = 1,2,3,4 \quad (2.23)$$

The vectors \mathbf{c}_i and \mathbf{c}_{i+1} are along the edges of S_i and point outwards from N_m , and the vector \mathbf{s} is the projection of the vector beginning at N_m and ending at N_s onto the closest segment (S_2 in this demonstration). The inequalities of Eqn. (2.23) ensure that the vector \mathbf{s} is between the vectors \mathbf{c}_i and \mathbf{c}_{i+1} and is thus located within the segment S_i . If the inequalities are not satisfied, another master segment containing N_m will be checked. The algorithm does not limit the number of segments containing N_m , and the master segment determined at the previous time step is preferentially checked at each time step.

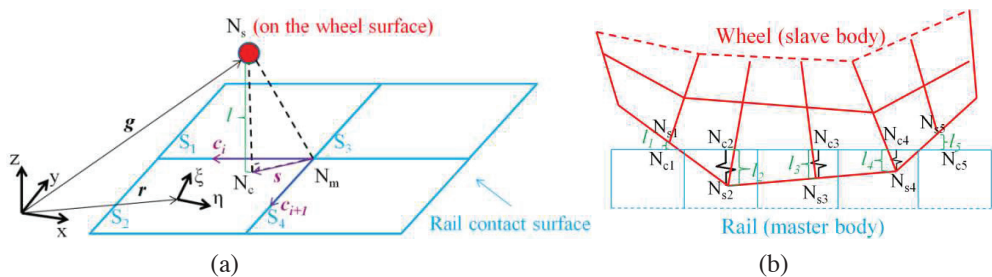


Figure. 2.1: Parametric representation of wheel-rail contact

The ‘contact point’ N_c is the projection of the slave wheel node N_s on the master rail segment (S_2 in this demonstration). The determined master segment has a bilinear parametric representation in a local coordinate system as follows:

$$\mathbf{r}(\xi, \eta) = \sum_{i=1}^3 f_i(\xi, \eta) \mathbf{i}_i \quad (2.24)$$

$$f_i(\xi, \eta) = \sum_{N=1}^4 \varphi^N(\xi, \eta) x_i^N \quad i = 1, 2, 3 \quad (2.24a)$$

$$\varphi^N(\xi, \eta) = \frac{1}{4} (1 + \xi \xi^N) (1 + \eta \eta^N) \quad N = 1, 2, \dots, 4 \quad (2.24b)$$

where $\mathbf{r}(\xi, \eta)$ represents the master segment; \mathbf{i}_i represents unit direction vectors; and x_i^N represents the nodal coordinates of the nodes contained by the segment. Let \mathbf{g} be a vector drawn to the slave node N_s . The contact point N_c with coordinates (ξ_c, η_c) on the master segment can be determined by satisfying the following:

$$\frac{\partial \mathbf{r}}{\partial \xi}(\xi_c, \eta_c) \cdot [\mathbf{g} - \mathbf{r}(\xi_c, \eta_c)] = 0 \quad (2.25a)$$

$$\frac{\partial \mathbf{r}}{\partial \eta}(\xi_c, \eta_c) \cdot [\mathbf{g} - \mathbf{r}(\xi_c, \eta_c)] = 0 \quad (2.25b)$$

The coordinates (ξ_c, η_c) in Eqns. (2.25a) and (2.25b) may be solved numerically with Newton-Rapson iterations. Since the method may diverge with distorted elements (Hallquist, 2006), a careful treatment of mesh in the wheel-rail contact region, especially in the solution zone, is highly desirable. Penetration of the slave wheel node through its master rail segment may then be judged by a scalar l :

$$l = \mathbf{n} \cdot [\mathbf{g} - \mathbf{r}(\xi_c, \eta_c)] \quad (2.26a)$$

$$\mathbf{n} = \mathbf{n}_i(\xi_c, \eta_c) = \left(\frac{\partial \mathbf{r}}{\partial \xi} \times \frac{\partial \mathbf{r}}{\partial \eta} \right) / \left| \frac{\partial \mathbf{r}}{\partial \xi} \times \frac{\partial \mathbf{r}}{\partial \eta} \right| \quad (2.26b)$$

If $l \geq 0$, no penetration occurs and nothing will be done; if $l < 0$, an interface force vector \mathbf{f}_{cN} normal to the master segment will be applied to the contact point, and its magnitude is proportional to the amount of penetration:

$$\mathbf{f}_{cN} = -lk\mathbf{n} \quad (2.26c)$$

Hence, interface springs may be assumed between the penetrating slave wheel nodes and rail contact surface as shown in Fig. 2.1 (b), and the penalty contact (spring) stiffness k is intrinsically the combination of a geometrical penalty term and a velocity penalty term (Wu, 2009). For the hexahedral elements containing the master segments used in the wheel-rail contact surfaces, k may be given in terms of the bulk modulus K , the element volume V and the face area A as follows:

$$k = \frac{f_{SI}KA^2}{V} \quad (2.26d)$$

where f_{SI} is a scale factor for the penalty contact stiffness. The choice of its value in wheel-rail interaction simulations will be discussed in Section 3.3.1. The equal and opposite contact forces distributed over the master segment nodes \mathbf{f}_{master}^J may also be obtained as follows:

$$\mathbf{f}_{master}^J = -\varphi^J(\xi_c, \eta_c) \mathbf{f}_{cN} \quad J = 1, 2, 3, 4 \quad (2.27)$$

The penalty contact algorithm implemented in the explicit FEM can treat an arbitrarily shaped surface by representing the surface with a faceted mesh.

2.6.2 Tangential contact

The Coulomb friction law is available to solve the wheel-rail tangential contact. A trial tangential contact nodal force \mathbf{f}^* at time step $t + 1$ may be defined as follows:

$$\mathbf{f}^* = \mathbf{f}_{cT}{}^t - k\Delta\mathbf{e} \quad (2.28a)$$

where $\mathbf{f}_{cT}{}^t$ is the tangential contact force calculated at time step t ; k is the penalty contact stiffness; and $\Delta\mathbf{e}$ is the incremental movement of the slave wheel node along the rail surface:

$$\Delta\mathbf{e} = \mathbf{r}^{t+1}(\xi_c^{t+1}, \eta_c^{t+1}) - \mathbf{r}^{t+1}(\xi_c^t, \eta_c^t) \quad (2.28b)$$

The traction bound $f_{bound}{}^t$ at time step t in the Coulomb friction law is the product of the magnitude of the normal force $\mathbf{f}_{cN}{}^t$ at the same time step and the coefficient of friction (COF) μ :

$$f_{bound}{}^t = \mu|\mathbf{f}_{cN}{}^t| \quad (2.28c)$$

The tangential contact force at time step $t + 1$ may thus be written as follows:

$$\mathbf{f}_{cT}{}^{t+1} = \begin{cases} \mathbf{f}^* & \text{if } |\mathbf{f}^*| \leq f_{bound}{}^{t+1} \\ \frac{f_{bound}{}^{t+1}\mathbf{f}^*}{|\mathbf{f}^*|} & \text{if } |\mathbf{f}^*| > f_{bound}{}^{t+1} \end{cases} \quad (2.28d)$$

The COF μ , which is considered a constant in the classical Coulomb's law, may vary with various factors in wheel-rail contact such as sliding speed, contact pressure, surface lubrication or contamination, roughness, temperature, and humidity (Zhao & Li, 2016). Section 2.2.2 demonstrated that the explicit FEM couples the calculation of wheel/rail dynamic responses with the calculation of wheel-rail contact in the time domain. Thus, a velocity-dependent Coulomb's law with a functional COF may be implemented in the explicit FEM. The COF updated at each time step may be expressed in terms of the static and dynamic friction coefficients μ_s and μ_d , respectively, a decay constant c and wheel-rail relative sliding velocities $\dot{\mathbf{u}}_{rel}$ between the slave nodes and master segments at the same time step as follows:

$$\mu(\dot{\mathbf{u}}_{rel}) = \mu_d + (\mu_s - \mu_d)e^{-c|\dot{\mathbf{u}}_{rel}|} \quad (2.29a)$$

$$\dot{\mathbf{u}}_{rel} = \Delta\mathbf{e}/\Delta t \quad (2.29b)$$

The decay constant c describes how fast the static coefficient approaches the dynamic coefficient and may be determined by fitting the measured results (Zhao & Li, 2016). Because the wheel-rail contact forces can be physically interpreted as externally applied tractions (Bathe, 1996; Wu & Gu, 2012), the contact force vector required in Eqn. (2.11) may be expressed as follows:

$$\mathbf{f}_{con}{}^t = \sum_{M=1}^m \left(\int_{\Gamma_{c,e}} \mathbf{N}^T (\mathbf{f}_{cN}{}^t + \mathbf{f}_{cT}{}^t) d\Gamma \right)^M \quad (2.30)$$

The traditional division of an elastic contact problem into a normal problem and a tangential problem is based on an assumption that the friction transmitted between elastic contact bodies has a negligible influence on the normal contact solutions (Poritsky, 1950). In

the explicit FEM, the normal and tangential contacts are calculated successively and dependently at each time step, which is necessary for solving inelastic contact problems. Studies with the explicit FEM (Deng *et al.*, 2015; Zhao & Li, 2015) have indicated that the tangential elastoplastic wheel-rail contact solutions have noticeable effects on the normal solutions: an increase in tangential force increases plastic flow, and the contact patch tends to become larger in size and shifts forward more.

2.6.3 Contact stability

The contact-based critical time step determined by the penalty contact algorithm is proportional to $\min[\sqrt{m^J/k}]$, where m^J ($J=1,2$) is essentially the mass attached to the contact ‘spring’ and k is the penalty contact stiffness given in Eqn. (2.26d). The time step size Δt used in the explicit FEM should not exceed the contact-based critical time step to avoid contact instability. The easiest method of increasing the contact-based critical time step is to scale down the penalty contact stiffness k .

2.7 Displacement constraints

Suitable displacement constraints are necessarily defined as essential boundary conditions in the mathematical model of wheel-rail dynamic interactions and are largely applied to structural boundaries, such as the inner end of wheel half-axles, the rail ends and the rail bottom surfaces (see Section 3.3.4). These constraints can be imposed by setting the constrained acceleration components to zero (Hallquist, 2006). Since the prescribed nodal displacement constraints are imposed in the local coordinate system, an orthogonal matrix Q constructed by the normalised unit vectors in the local axes needs to be employed to transform the global nodal acceleration vectors \ddot{u}_i^N (for node N) updated by Eqn. (2.11) to the local system as follows:

$$\ddot{u}_{Loc i}^N = Q \ddot{u}_i^N \quad i = 1,2,3 \quad (2.31a)$$

After the constrained acceleration components are zeroed, the modified vectors $\ddot{u}_{Loc i}^N$ can be transformed back to the global system:

$$\ddot{u}_i^N = Q^T \ddot{u}_{Loc i}^N \quad i = 1,2,3 \quad (2.31b)$$

where \ddot{u}_i in Eqn. (2.31b) is the finally updated nodal acceleration vector of the time step, which will further be integrated to approximate the nodal velocities and displacements by Eqns. (2.12a) and (2.12b).

2.8 Summary of the algorithms

By systematically exploring the core algorithms employed in the explicit FE wheel-rail interaction analyses, this chapter enhances the understanding of the explicit FE wheel-rail interaction studies and shows the applicability of the explicit FEM to the wheel-rail dynamic interaction analyses from a theoretical perspective. The advantages of using the explicit FE algorithm to solve the wheel-rail dynamic interactions may thus be summarised as follows:

- The explicit FEM couples the calculation of wheel/rail structural dynamic responses with the calculation of wheel-rail contact, which makes the explicit FEM an ideal approach for solving wheel-rail dynamic interactions and provides a theoretical basis for the indirect validation of the wheel-rail dynamic contact solution.

- The explicit FEM is capable of treating nonlinearities in materials, geometry and boundary conditions. The implemented penalty contact algorithm can handle arbitrarily shaped contact surfaces, and it calculates normal and tangential contact successively and dependently at each time step, which is necessary for solving inelastic wheel-rail contact problems.
- By avoiding the need for matrix evaluation, assembly and decomposition as required by implicit integration algorithms, the explicit procedure is computationally attractive for analysing high-frequency dynamic problems of short duration, especially when the total dynamic response time that must be modelled is only a few orders of magnitude longer than the stability critical time step, which is frequently the case in wave propagation analyses (Noh & Bathe, 2013). The explicit wheel-rail FE model may include in its solution all the relevant vibration modes of structures and continua and associated wave propagations.

The conditionally stable explicit FEM is, however, less efficient than the implicit FEM for static equilibrium analyses or low-frequency dynamics problems lasting for a much longer time period (Zhao *et al.*, 2016). Implicit-explicit sequential approaches may thus be employed to minimise both the solution time and the dynamic effects induced by the initialisation of wheel-rail interaction analysis. The implicit-explicit sequential approach involves performing an implicit static equilibrium analysis followed by an explicit transient dynamics analysis. The modelling procedure is elaborated in the next chapter.

3

MODELLING PROCEDURE AND SOLUTION ANALYSES

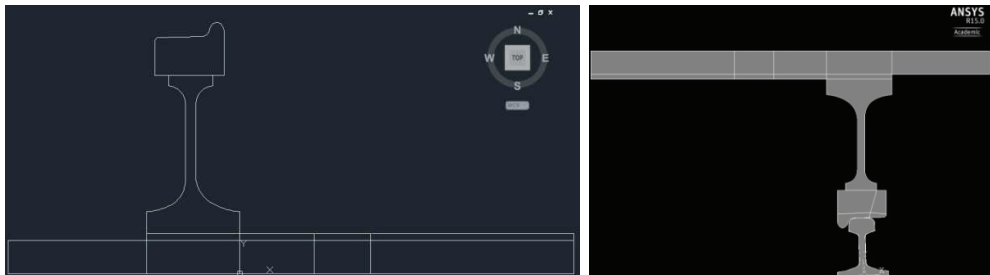
This chapter first discusses in Sections 3.1~3.3 how to establish robust explicit FE wheel-rail dynamic interaction models. A basic explicit FE wheel-rail dynamic interaction model may contain a half-track model and a half-wheelset model with its share of the sprung mass of a car body and a bogie. The modelling procedure may be divided into three stages in a physical sequence: Stage 1. build wheel and rail models; Stage 2. let the wheel and rail come into contact and achieve static equilibrium; and Stage 3. let the wheel roll along the rail. The commercial programs ANSYS/LS-DYNA were employed to demonstrate this modelling procedure, and other programs with implementations of implicit-explicit sequential approaches, such as ABAQUS/Explicit, may also be applied. Sections 3.4~3.5 introduce post-processing approaches to converting the output of numerical programs for wheel/rail nodal forces and nodal motions into wheel-rail contact and dynamics solutions.

3

3.1 Modelling of wheel and rail structures

3.1.1 Geometry modelling

The geometries of wheels and rails, including the contact profiles, should be modelled as realistically as possible because they may influence both the structural dynamic properties and contact solutions. The detailed nominal geometries of a wheel radial section and a rail cross section may initially be created in a graphical software (e.g., AutoCAD; see Fig. 3.1 (a)). Based on these geometries, the wheel and rail volumes can subsequently be generated in the pre-processing FE software (e.g., ANSYS; see Fig. 3.1 (b)) by rotating the wheel radial section with respect to the central line of the wheel axle and extruding the rail cross section longitudinally. The wheel/rail volumes are suggested to be generated after meshing the wheel radial section and rail cross section for modelling convenience.



(a) Generated in AutoCAD

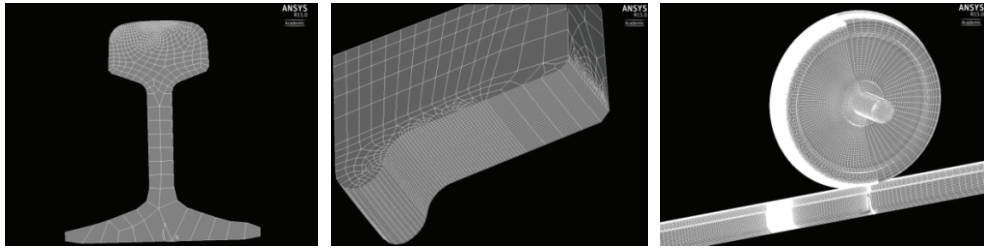
(b) Generated in ANSYS

Figure. 3.1: Modelling of wheel and rail geometries

3.1.2 Mesh

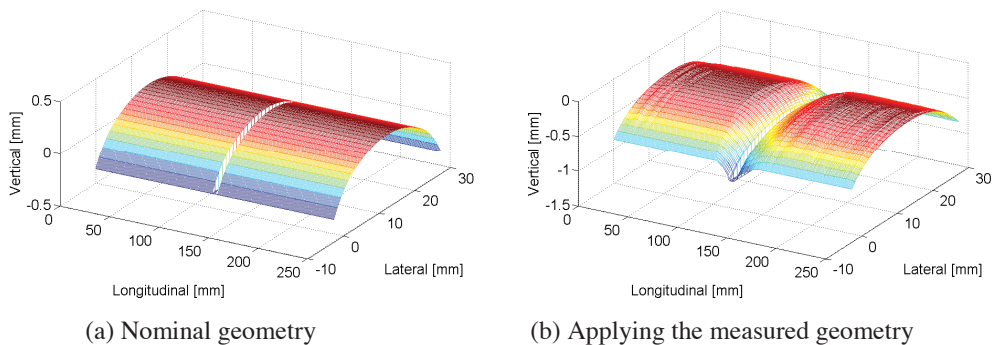
Adequately fine mesh is needed for a robust FE wheel-rail interaction model, especially when precise contact solutions and high-frequency dynamics are desired. Zhao and Li (Zhao & Li, 2011) report that the element size of approximately $1/20$ of the minor axis of the contact patch tends to provide accurate contact solutions, whereas approximately $1/10$ of the minor axis may be acceptable for many engineering problems. To obtain an optimal mesh in the sense of cost effectiveness and acceptable error, a partially refined mesh as shown in Fig. 3.2 may yield a better approximate solution (Hu & Wriggers, 2002). Fine special discretisation should be concentrated on the prospective contact regions. Another meshing method balancing

the efficiency and accuracy of contact solutions uses the surface-based tie constraints to refine the mesh in the contact regions (Pletz *et al.*, 2012b, 2012a). The tetrahedral or wedge elements with triangular faces, which have indeterminate contact condition at the corners, are not suitable for analysing contact problems and should be avoided (Hibbitt & Sorensen, 2001).



(a) Mesh of rail cross section (b) Mesh of wheel tread (c) Overview of wheel & rail meshes
Figure. 3.2: Wheel and rail meshes

Profiles with geometric irregularities are generally considered in the wheel-rail impact contact simulations (Li *et al.*, 2008; Molodova *et al.*, 2011; Zhao *et al.*, 2012; Molodova *et al.*, 2014; Yang *et al.*, 2015; Wei *et al.*, 2017b). One example of the measured rail top surface with geometric irregularities at an insulated rail joint (IRJ) is shown in Fig. 3.3. The rail surface geometric irregularities measured by Railprof (Molodova *et al.*, 2014) or HandySCAN (Wei *et al.*, 2017a) may be imposed on the originally smooth surface of the model by adjusting the nodal coordinates in the input files of the dynamic analysis solver.



(a) Nominal geometry (b) Applying the measured geometry
Figure. 3.3: Measured geometry applied to a wheel-insulated rail joint impact model (Yang *et al.*, 2018)

3.1.3 Modelling of other components and model parameters

In addition to the wheel and rail, other train/track components such as the car body, primary suspension, sleepers, fastenings and ballast, may be modelled for different study purposes. The sleepers may also be modelled with hexahedral elements as well as different material properties than those used in the rail and wheel models; the ballast is generally built as spring-damper pairs with a fixed foundation; and the fastening models may significantly influence the track dynamic behaviour, whose modelling techniques were comprehensively

discussed in (Zhao *et al.*, 2014a; Oregui *et al.*, 2015b). Because the car body and the bogie frame have a negligible influence on high-frequency wheel-rail dynamic interactions, they are normally simplified as mass elements connected to the wheelset by the primary suspension with parallel linear springs and viscous dampers.

The explicit FE wheel and rail models generally adopt either elastic or elastoplastic steel with nominal values as the material; and the sleeper models normally adopt elastic timber or concrete as the materials, although inelastic models can be conveniently used. Because the parameters used in fastening and ballast models can rarely be directly measured in the field, they are generally calibrated by fitting the simulated frequency response functions to the measured values (Oregui *et al.*, 2015b; Oregui *et al.*, 2016). Typical values of the parameters employed in the explicit FE wheel-rail interaction models can be found in (Zhao *et al.*, 2012; Molodova *et al.*, 2014).

3

3.2 Modelling of static contact

A wheel-rail static equilibrium analysis may be performed to obtain the deformation of structures caused by the gravitational load, which will subsequently be considered the initial conditions for the wheel-rail dynamic interaction analyses. The augmented Lagrangian contact algorithm is recommended for the wheel-rail static contact analysis, which is intrinsically an iterative series of penalty methods with automatic updates of penalty values (Mijar & Arora, 2004). The contact pair with a static COF needs to be defined, and it consists of the wheel and rail surface nodes that may be within the static wheel-rail contact patch.

In the wheel-rail static contact analysis, the rail ends, half-wheel-axle ends and car body should be constrained in the lateral (U_x) and longitudinal (U_z) directions. To prevent the wheel model from undesired rolling, its central radial section (normal to the rail longitudinal direction) can be constrained in the longitudinal direction (U_z); see Fig. 3.4. By applying the gravitational load, the static contact solutions can be obtained. Fig. 3.5 shows the distribution of the vertical components of the stresses on a piece of rail model that was in contact with the wheel model in a static contact analysis. An elliptical contact patch can be clearly seen at the top of the rail.

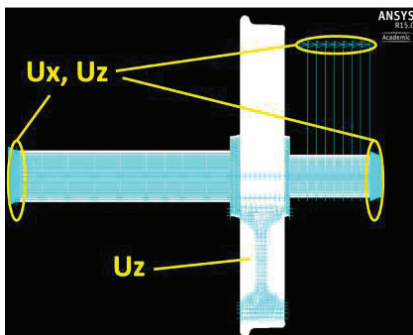


Figure. 3.4: Displacement constraints

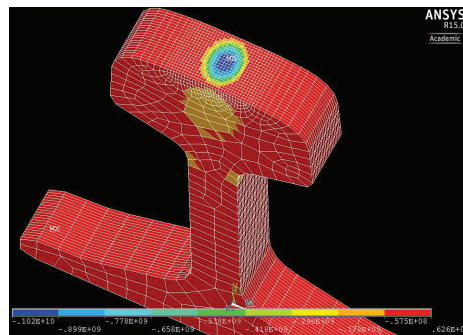


Figure. 3.5: Static contact solution

3.3 Modelling of dynamic interactions

As indicated by the numerical solution procedure presented in Table 2.1, definitions of the wheel-rail rolling contact pair, the initial conditions, and the load and displacement boundary conditions are required to proceed with an explicit FE wheel-rail dynamic interaction analysis.

3.3.1 Rolling contact pair

A rolling contact pair needs to be defined in the wheel-rail transient frictional rolling calculation. To employ the penalty contact algorithm introduced in Section 2.6, the master and slave segments of the rolling contact pair defined on the rail top and wheel tread should contain the whole prospective rolling contact region; however, the defined contact regions should be as small as possible to reduce the computation costs caused by contact searching. One example of the contact pair defined for an explicit FE wheel-rail dynamic interaction analysis is shown in Fig. 3.6.

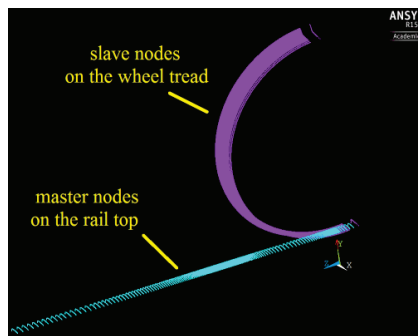


Figure. 3.6: Contact pair defined for the explicit FE wheel-rail dynamic interaction analysis

Either constant or variable COFs may be used in wheel-rail rolling simulations. Zhao and Li (Zhao & Li, 2016) studied wheel-rail dynamic contact solutions that implemented a velocity-dependent COF and concluded that the velocity-dependent COF may mimic a more realistic contact condition and provide a less regular adhesion-slip distribution pattern compared with the constant COF.

Sections 2.6.1 and 2.6.3 mentioned that the scale factor of the penalty contact stiffness f_{SI} plays an important role in the penalty contact algorithm. Ideally, a sufficiently high and low contact stiffness is required so that the penetration and slip distance are acceptably small and the problem can be well-behaved in terms of convergence, respectively. Fig. 3.7 compares the wheel-rail contact solutions obtained with different scale factors of the penalty contact stiffness: $f_{SI}=1, 0.5$ and 0.1 . The contact pressure magnitudes are indicated by contour lines, and the tangential stresses are indicated by red arrows. The arrows point in the directions of the tangential stresses, and their lengths are proportional to the magnitude. This figure shows that with decreasing scale factor f_{SI} (from Fig. 3.7 (a) to (c)), the obtained contact patch areas increases while the contact pressure decreases. A value of $f_{SI} = 1$ is recommended for wheel-rail dynamic interaction analyses. The contact solutions provided by $f_{SI} = 1$ are consistent with those obtained by the Hertz contact theory and CONTACT (Zhao & Li, 2011; Deng *et al.*, 2015); moreover, when applying 1 mm or even finer wheel/rail surface meshes, $f_{SI} > 1$ may

require the time step size to be scaled down for computational stability, which decreases the efficiency of the explicit integration.

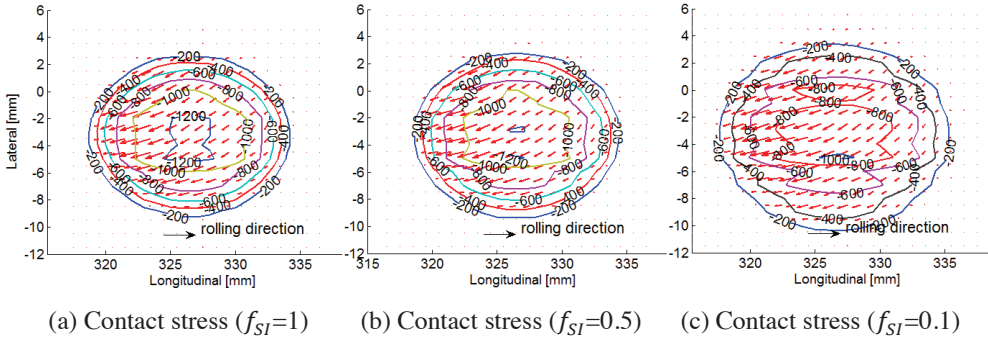


Figure. 3.7: Contact solutions with different f_{SI} values (contour graph unit: MPa)

3.3.2 Initial conditions

By applying the implicit-explicit sequential analysis, the initial nodal displacements of the wheel-rail transient rolling simulation can be obtained by the wheel-rail static equilibrium analysis illustrated in Section 3.2. The initial nodal velocities of the wheel in both rotation and forward translation should be prescribed, and the value of the applied wheel rotational velocity equals the quotient of the applied translational velocity and the wheel radius. The equivalent translational nodal velocities should also be applied to the primary suspensions and sprung mass because they travel forward together with the wheel.

3.3.3 Load boundary conditions

In addition to the gravitational load illustrated in Section 2.3.1, the driving torque is another widely used load boundary condition in the simulation of wheel-rail tractive frictional contact (Li *et al.*, 2008; Molodova *et al.*, 2011; Zhao *et al.*, 2012; Molodova *et al.*, 2014; Yang *et al.*, 2015; Wei *et al.*, 2017b). Because the hexahedral elements used to construct wheel models have only translational freedom, the Hughes-Liu (H-L) beam elements (Hughes & Liu, 1981) degenerated from the hexahedral element can be employed to take the externally exerted torque. As shown schematically in Fig. 3.8, four H-L beam elements with length L are used. The L value should not be too small because the critical time step size of the H-L beam element for integration stability is $\Delta t_{H-L} = L/\sqrt{E/\rho}$. Each H-L beam element consists of three nodes: I_j ($j=1,2,3,4$), J and K. Nodes $I_1 \sim I_4$ and J are all attached to the wheel model and located in the same plane S . Node J is the driven node located at the wheel axial centre and shared by the four beam elements. Node K is also shared by the four beam elements, and it is required to define the axis system of beam element. The vector pointing from K to J is normal to plane S . A driving torque M_T in plane S is applied to the driven node J, and its direction is determined by the right-hand rule.

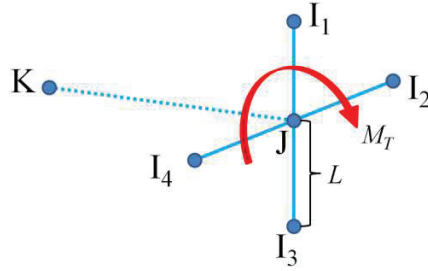


Figure. 3.8: Driving torque applied to four H-L beam elements

Driven by the torque, the wheel rolls along the rail with a consequently generated longitudinal creep force F_L between the wheel and rail, which satisfies the requirement that the traction coefficient μ_T is less than the COF μ . The traction coefficient is distinguished from the COF in wheel-rail rolling contact studies by its definition in Eqn. (3.1):

$$\mu_T = \frac{F_L}{F_N} < \mu \quad (3.1)$$

where F_L and F_N are the longitudinal and normal contact forces, respectively, and μ is the overall COF of the contact pair that limits the traction force transmitted in the contact. The overall COF may be different from the local COF at certain nodes when the velocity-dependent friction is considered (Zhao & Li, 2016). In addition, the traction coefficient may be assumed to be constant in stationary rolling, whereas it varies with time in dynamic rolling because of vibration, and its nominal value is proportional to the applied driving torque (Eqn. (3.1)).

A sudden exertion of driving torque may bring significant excitation to the wheel-rail rolling system. A gradually increased driving torque is thus suggested to avoid excitation as much as possible (Wei *et al.*, 2016) and minimise the dynamic relaxation process (see Section 3.3.5). A functional driving torque $M_T(t)$ is investigated here and is expressed as follows:

$$M_T(t) = \begin{cases} \frac{M_0}{2} \left(1 - \cos\left(\frac{\pi t}{t_0}\right) \right), & t < t_0 \\ M_0, & t \geq t_0 \end{cases} \quad (3.2)$$

where M_0 is the maximum value of the torque and t_0 is the duration required to reach M_0 . Fig. 3.9 graphically shows the loading function with $M_0=20$ kN·m and $t_0=6$ ms. Fig. 3.10 compares the calculated wheel-rail normal loads and creep forces with the applications of the loading function in Eqn. (3.2) and a constant driving torque $M_T(t)=20$ kN·m. This figure shows that the functional driving torque significantly damps the undesired excitation on the creep force, whereas it has less, if any, effect on the normal load.

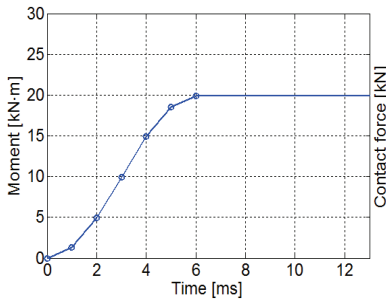


Figure 3.9: Functional driving torque

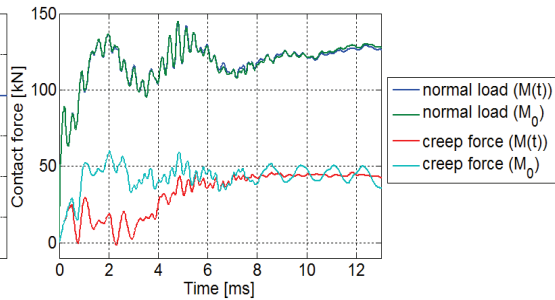


Figure 3.10: Forces obtained with different torque functions

3

3.3.4 Displacement boundary conditions

Different displacement boundary conditions may be applied to the explicit FE wheel-rail interaction models according to different research objectives. When the structural dynamics are of less concern or quasi-steady-state contact solutions are desired, the bottom surface of the rail foot may be fully constrained as in the models presented in (Zhao & Li, 2011; Deng *et al.*, 2015). When the dynamic effects must be considered and captured, a more detailed modelling of the track substructure is necessary (Li *et al.*, 2008; Molodova *et al.*, 2011; Molodova *et al.*, 2014; Oregui *et al.*, 2015b; Oregui *et al.*, 2016; Yang *et al.*, 2016; Zhao *et al.*, 2016; Wei *et al.*, 2017b). The fastening models simplified as spring-damper pairs may be constrained in the lateral and longitudinal directions if only the vertical dynamics are of concern (Oregui *et al.*, 2016). More complex boundary conditions are required when solid rail-pad representations of rail fastenings are used (Oregui *et al.*, 2015b). Because the ballast has less influence on the wheel-rail dynamic contact solutions, it is normally constrained in both the lateral and longitudinal directions and fixed at the foundation.

When only a half wheelset is modelled, the inner end of the wheel half-axle can be constrained in the lateral direction to keep the rolling wheel from toppling over. The ends of the finite-length rail models are generally constrained in the lateral and longitudinal directions, which may cause reflective waves that influence the solutions, especially when the track models are insufficiently long. A numerical experiment conducted in (Molodova, 2013) indicated that a FE track model with a length of 20 m is considered sufficiently long to reduce the influence of wave reflection, whereas a length of 10 m may meet engineering requirements for reproducing the measured axle box acceleration. Non-reflective boundary conditions have also been implemented in certain commercial FE programs (Hibbit & Sorensen, 2001; Hallquist, 2006), and their application on wheel-rail dynamic interactions is currently under development.

3.3.5 Dynamic relaxation

In the analysis of wheel-rail dynamic interactions, a certain length of rolling distance from the wheel initial position to the solution zone is necessary to damp the oscillations caused by the wheel/rail initial kinematic and potential energy from imperfect static equilibrium (Zhao & Li, 2011). This process is called dynamic relaxation. Because the wheel-rail rolling contact physically excites vibrations of the structures and waves in continua, the quasi-steady state may be considered to be achieved by the dynamic relaxation when the oscillations are damped

out to less than 10% of the static values (Yang *et al.*, 2016). The wheel-rail dynamic interaction solutions obtained after the process of the dynamic relaxation can be output for post-processing.

3.3.6 Time step control

As mentioned in Section 2.2.3, a scale factor sf is employed to control the time step and to guarantee the stability of the explicit integration, and $sf = 0.9$ has been widely used in previous explicit FE wheel-rail interaction studies. Applying smaller time steps in the explicit FEM may produce better accuracy as reported in (Wu & Gu, 2012). Fig. 3.11 compares the contact solutions obtained with $sf=0.9$ and 0.6 (used for explosive problems), where F_n , F_t , and μ are the amplitudes of the contact pressure, surface shear stress, and COF, respectively. The excellent consistency of the results obtained with different value of sf indicates that a scale factor of 0.9 is acceptable for wheel-rail interaction analyses, and it guarantees integration stability and simultaneously decreases the solution time.

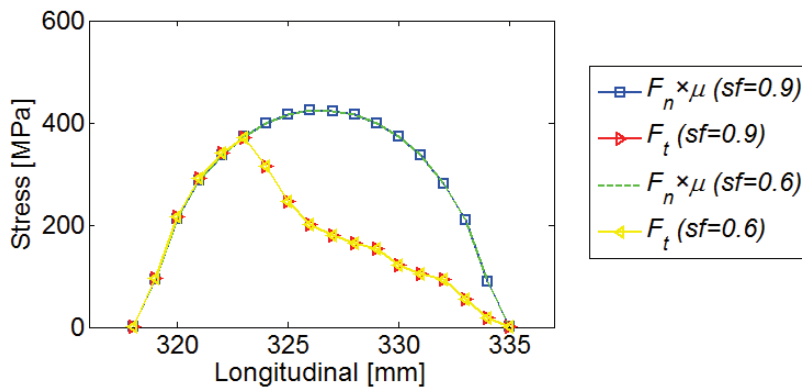


Figure. 3.11: Comparison of contact stresses calculated with $sf=0.9$ and 0.6

3.4 Obtain wheel-rail contact solutions

The wheel-rail contact solutions of interest generally include the contact patch area, normal and shear contact stresses, and micro-slip and adhesion-slip distributions within the contact patch. These solutions can be obtained by post-processing the nodal force and nodal motion simulated by the wheel-rail dynamic interaction models.

3.4.1 Contact patch area and stresses

The contact patch area may be determined with surface nodal forces: a surface node is in contact if the nodal force in the direction normal to the local surface is non-zero (Zhao & Li, 2011; Deng *et al.*, 2015; Yang *et al.*, 2016). Hence, the first step is to convert the output surface nodal forces in the global coordinate system into those in the local coordinate system. Because inertia force is included in the dynamic analyses, the force of a surface node outside the contact may be small but non-zero; thus, a non-zero threshold (e.g., 0.001 N) is used in practice to determine whether a node is in contact. Fig. 3.12 shows one example of the wheel and rail nodes in contact determined by this rule.

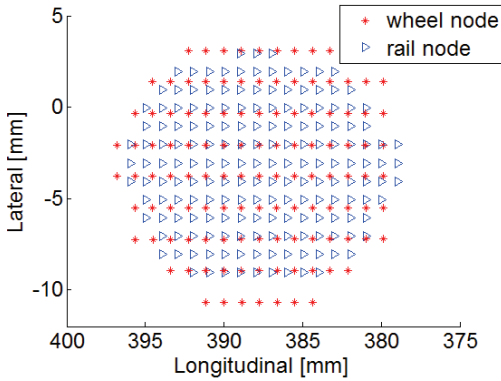


Figure. 3.12: Wheel/rail nodes in the contact patch

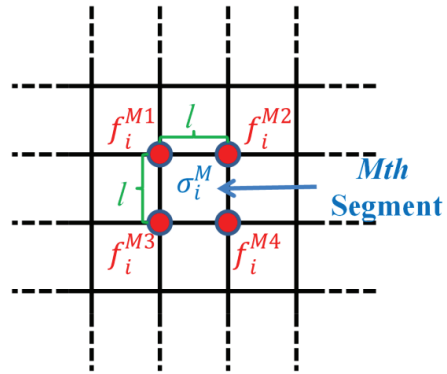


Figure. 3.13: Nodal forces converted into contact stresses

The contact stresses, including the surface normal stress and shear stress, may be calculated with the nodal forces in the local coordinate system. For the generally used quadrilateral segments:

$$\sigma_i^M = \sum_{j=1}^4 \frac{f_i^{MJ}}{4l^2} \quad i = 1,2,3 \tag{3.3}$$

where σ_i^M is the contact stress vector on the M th segment of the wheel/rail surface and the spatial components, with $i = 1,2,3$ representing the normal, lateral and longitudinal directions in the local coordinate system, respectively; f_i^{MJ} is the local nodal force vector, with $J = 1,2,3,4$ representing the number of the nodes constructing segment M as shown schematically in Fig. 3.13; and l is the dimension of the quadrilateral segment. According to Newton's third law, the contact stresses may be calculated with either the wheel nodal forces or rail nodal forces. Fig. 3.14 compares the contact stresses calculated with the wheel and rail nodal forces and indicates that the choice has negligible influence on the calculated contact stresses.

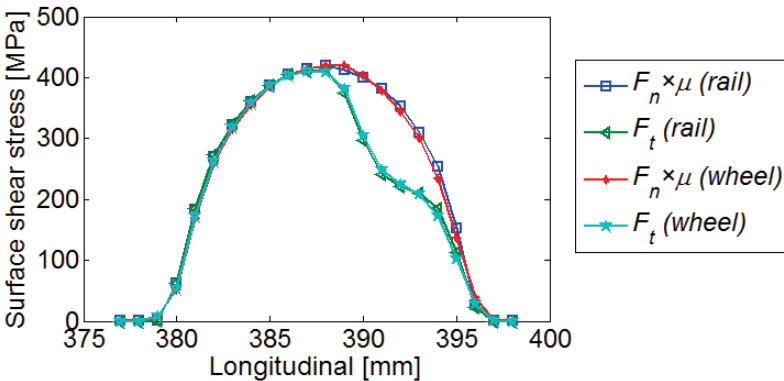


Figure. 3.14: Contact stresses calculated with wheel and rail nodal forces

3.4.2 Micro-slip distribution

The micro-slip refers to the tangential relative velocity between two particles in contact. As explained in Section 2.6.1, a rail surface contact node is actually in contact with the ‘contact point’ rather than a wheel surface node; thus, interpolations are required to convert the velocities of wheel nodes into the velocities of the ‘contact points’. Fig. 3.15 schematically shows a length-weighted linear interpolation scheme. In Fig. 3.15 (a), the red cross represents an arbitrary rail node N_r and the four blue spots N_{wi} ($i = 1,2,3,4$) represent the four wheel nodes composed of the wheel surface segment in contact with the rail node N_r . Another blue spot overlapping the red cross in Fig. 3.15 (b) denotes the interpolated ‘contact point’ N_w on the wheel surface and in contact with rail node N_r ; and l_i ($i = 1,2,3,4$) indicates the distances from the ‘contact point’ N_w to the four sides of the wheel surface contact segment.

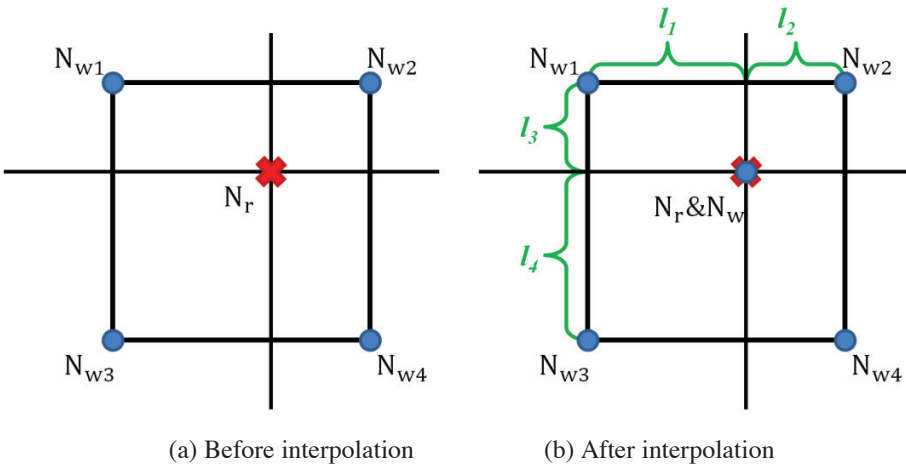


Figure 3.15: Interpolated wheel nodal coordinate/motions into rail

The interpolated velocities \mathbf{v}_w of the ‘contact point’ N_w may be obtained by the length-weighted linear interpolation as follows:

$$\mathbf{v}_w = \frac{l_2 l_4 \mathbf{v}_1 + l_1 l_4 \mathbf{v}_2 + l_2 l_3 \mathbf{v}_3 + l_1 l_3 \mathbf{v}_4}{(l_1 + l_2)(l_3 + l_4)} \quad (3.4)$$

where \mathbf{v}_i ($i = 1,2,3,4$) represents the nodal velocities of the wheel nodes N_{wi} . The micro-slip \mathbf{s}_n may then be calculated as follows:

$$\mathbf{s}_n = \mathbf{v}_w - \mathbf{v}_r \quad (3.5)$$

where \mathbf{v}_r are the nodal velocities of the rail node N_r . The length-weighted linear interpolation scheme is also applicable to the calculations for the displacement, acceleration and vertical coordinate (normal to the local contact surface) of the ‘contact points’ on the wheel. The accuracy of the length-weighted linear interpolation scheme may conveniently be estimated by comparing the wheel vertical coordinates before and after interpolation. Fig. 3.16 shows that the interpolated wheel surface formed by the ‘contact points’ overlaps the original wheel surface, indicating that the interpolation scheme is reliable. In addition, note that the calculated wheel-rail contact patch is not flat but saddle shaped. This result confirms that the

explicit FEM drops the half-space assumption and the non-flat contact patch may cause geometric spin (Zhao & Li, 2011; Deng *et al.*, 2015).

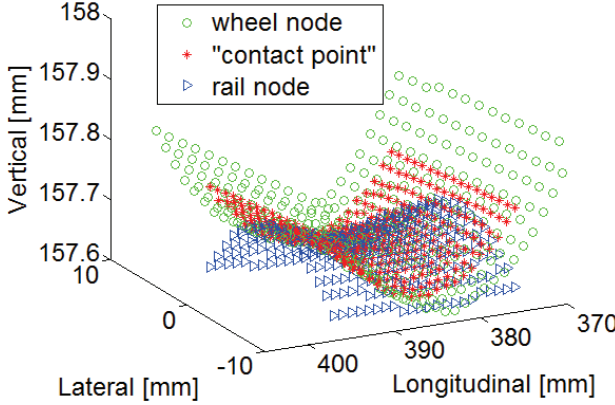


Figure. 3.16: Positions of the wheel/rail nodes and interpolated ‘contact points’

3.4.3 Adhesion-slip distribution

The division of the adhesion and slip regions in the contact patch is an important feature of the frictional rolling contact. The slip region can be distinguished from the adhesion region either by comparing the surface shear stress F_t with the traction bound $\mu|F_n|$ or by calculating the micro-slip s_n within the contact patch. A node is in a slip region if:

$$\mu|F_n| - |F_t| < \varepsilon_T \quad \text{or} \quad |s_n| > \varepsilon_s \quad (3.6)$$

where ε_T and ε_s are the tolerances of the two approaches. A value of 0.3 percent of the maximal tangential nodal force in the contact patch is suggested for ε_T (Zhao & Li, 2011; Wei *et al.*, 2016; Zhao & Li, 2016), whereas a value of 0.05 m/s is suggested for ε_s (Zhao & Li, 2016). For a robust wheel-rail dynamic interaction model, the calculated adhesion-slip distribution determined by both approaches should be consistent with each other.

3.5 Obtain structural dynamic responses

To obtain the structural dynamic responses, which are generally the vibration acceleration and velocity, the nodes enclosed by the part of the structure of interest need to be selected. The structural vibration accelerations $\ddot{\mathbf{u}}_{str}$, for example, may then be calculated by averaging the accelerations of the nodes enclosed by the structural part in the global coordinate system $\ddot{\mathbf{u}}^N$:

$$\ddot{\mathbf{u}}_{str} = \frac{1}{n} \sum_{N=1}^n \ddot{\mathbf{u}}^N \quad (3.7)$$

where n is the total number of nodes enclosed by the structural part.

4

NUMERICAL EXAMPLE 1: MODELLING OF IMPACT CONTACT

This chapter gives the first numerical example – simulating wheel-rail impacts at a typical Dutch insulated rail joint (IRJ) – to demonstrate the effectiveness of the explicit FEM for the modelling of wheel-rail dynamic interactions. Fig. 4.1 shows the outline of this chapter. Section 4.1 reviews previously published analytical and numerical studies of wheel-IRJ impact; To take dynamic effects due to impact into account, Section 4.2 presents a 3D explicit FE wheel-IRJ dynamic interaction model; Section 4.3 validated the dynamic behaviour of the IRJ the wheel sub-models against a comprehensive hammer test and a reported measurement, respectively, to qualify the model for the simulation of train pass-by interaction; Good agreements achieved in Section 4.4 comparing the simulated rail vertical and lateral vibrations up to 10 kHz due to the wheel-IRJ impact with the pass-by measurement results indicate that the explicit FEM is reliable for the prediction of high-frequency structural dynamic responses; Section 4.5 presents wheel-rail dynamic impact contact solutions simulated by the validated explicit FE wheel-IRJ interaction model; The impact-induced wave generation and propagation captured by the wheel-rail dynamic contact solutions are analysed in Section 4.6; A summary of this chapter is given in Section 4.7.

4	Sec. 4.1 Review wheel-IRJ impact studies	Sec. 4.2 Establish wheel-IRJ dynamic interaction model	Sec. 4.3 Validate IRJ and wheel sub- models	Sec. 4.4 Validate wheel-IRJ dynamic interaction model	Sec. 4.5 Analyse simulated dynamic contact solutions	Sec. 4.6 Capture generation and propagation of waves	Sec. 4.7 Summary
---	---	--	---	---	--	--	---------------------

Figure 4.1: Outline of Chapter 4

4.1 Introduction of the wheel-rail impact at IRJs

As essential track components for rail connections and signal transmission and control, insulated rail joints (IRJs) have been widely used in both traditional and high-speed railways. The performance of IRJs directly influences railway transportation safety. However, due to the significant stiffness and geometric discontinuities, the IRJ is considered as one of the weakest parts of railway track structures. When a train runs over an IRJ, wheel-rail impact occurs. This impact consequently leads to vibration and noise and accelerates track deterioration in the vicinity of the IRJ.

Numerous modelling works have been carried out to simulate wheel-rail impacts generated by IRJs. Because impact problems are inherently non-linear, the simulation models are required to be solved in the time domain. Computationally efficient analytical models have been applied to calculate wheel-rail interactions when material complexity and detailed contact solutions are of less concern (Kerr & Cox, 1999; Wu & Thompson, 2003; Kitagawa *et al.*, 2015; Mandal *et al.*, 2016). Considering a reduction of bending stiffness at a joint, Kerr and Cox (1999) simplified the joint of a track model as a gap and connected rails and fishplates with Winkler-type springs, whose stiffness was calibrated by a static load measurement. Mandal *et al.* (2016) idealised the dipped rail joint with a sinusoidal profile to analyse the impact forces considering both track design and operational parameters. Wu and Thompson (2003) treated the joint of their model as a pin between two semi-infinite Timoshenko beams and calculated the wheel-IRJ interaction by a relative displacement excitation model proposed by Grassie *et al.* (1982). Kitagawa *et al.* (2015) modified Wu and

Thompson's model by replacing the pin with a complex spring to represent the joint, whose vibratory behaviour level was validated against a field test. However, these analytical models fail to address the issues of the complex wheel-IRJ impact contact solutions and high-frequency impact dynamics over 5 kHz.

With the development of computer technology, the numerical finite element method (FEM) has increasingly been used to predict degradations of IRJs due to complex wheel-IRJ impact contact (Chen & Kuang, 2002; Wen et al., 2005; Chen & Chen, 2006; Kabo et al., 2006; Cai et al., 2007; Himebaugh et al., 2008; Sandstrom & Ekberg, 2009; Mandal & Dhanasekar, 2013; Mandal, 2016). A 3D FE analysis performed by Chen and Kuang (2002) indicated that the traditional Hertzian contact theory (Hertz, 1882) is inadequate to predict wheel-rail contact pressure distributions around IRJs. Chen and Chen (2006) established a 2D FE model to study the effects of an IRJ on wheel-rail contact stresses distributions under the condition of partial slip and suggested that Carter's theory (Carter, 1926) is no longer effective to predict the tangential stress distributions of wheel-rail contact at IRJs. Wen et al. (2005) applied an explicit FEM for the contact-impact stress analysis at rail joint regions, which can take dynamic effects into account. The explicit FE model was then developed by Cai et al. (2007) to calculate the dynamic impact force, stresses and strains when a wheel passes an IRJ with a height difference. Sandstrom and Ekberg (2009) employed a 3D elastoplastic FEM model to predict plastic deformation and fatigue due to wheel-IRJ impacts by capturing the accumulation of plastic strain. Mandal and Dhanasekar (2013) proposed a sub-modelling FE strategy to examine the ratcheting failure of IRJs. The same strategy was adopted by Mandal (2016) to study the influences of end-post materials on railhead deterioration at IRJs. Zong and Dhanasekar (2013) employed genetic algorithms coupled with FEMs to reduce impact stress through shape optimization of railhead at joints. On the basis of the coupled genetic algorithm and a parametric FEM, Zong and Dhanasekar (2017) also developed a new design of IRJ; the design relied on embedding gapped rails within one sleeper to provide sufficient rigidity to the rail ends, and may eliminate a number of components of IRJ and their associated modes of failure. Owing to the capability of coping with non-linear material properties and arbitrary discontinuous contact geometries, finite element contact models are considered capable of providing more accurate and detailed contact solutions.

To take account of complex impact contact and high-frequency wheel/rail dynamic effects, this study simulates a wheel-rail impact at a typical IRJ in the Dutch railway network by an explicit FEM. Performing the integration in the time domain with an explicit central difference scheme, the explicit FEM manages to reproduce high-frequency dynamic effects by detailed modelling of the structure of wheel/track system and employing a small time step. Compared to the explicit FE impact models proposed in the previous research (Wen *et al.*, 2005; Cai *et al.*, 2007; Li *et al.*, 2008; Pletz *et al.*, 2012; Molodova *et al.*, 2014; Yang *et al.*, 2015), the explicit FE dynamic interaction model presented in this study is more sophisticated in track dynamics and comprehensively validated. The validity of the transient impact contact solutions simulated in this study is confirmed from the following three aspects:

1. Quasi-static frictional rolling contact solutions calculated by the explicit FEM have been shown to be accurate via comparisons with Hertzian and CONTACT solutions (Zhao & Li, 2011; Deng *et al.*, 2015).

2. Dynamic effects up to 10 kHz involved in the wheel-IRJ impact contact solutions have been validated against a comprehensive field measurement (see Section 4.4) because the

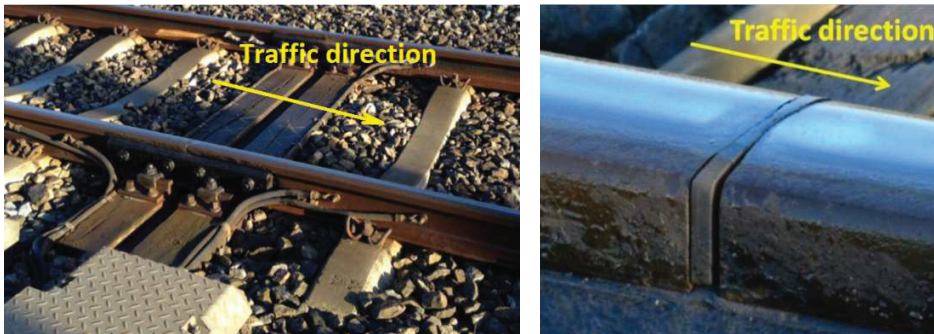
calculations of wheel/rail dynamic responses and contact forces are automatically coupled in the explicit FEM.

3. Regular wave patterns observed in the simulated transient contact solutions (see Section 4.5.3) reflect continuum vibrations excited by wheel-rail frictional rolling contact (Zhao & Li, 2011) and provide more evidence for the reliability of the calculated transient solutions of impact contact.

4.2 Wheel-IRJ dynamic interaction model

4.2.1 Condition of the target IRJ

A typical Dutch IRJ without visible damage was selected as the study target in the trunk line Amsterdam-Utrecht of the Dutch railway network. The IRJ locates on a straight track with a maximum one-directional train speed of 130 km/h. In the track, UIC54 rails with an inclination of 1/40 are supported by NS90 sleepers every 0.6 m except in the proximity of the IRJ, where a pair of adjacent timber sleepers with a distance of 0.24 m are employed to reduce the deflection of the joint and absorb vibration caused by wheel-IRJ impacts. Fig. 4.2 shows the in situ condition of the target IRJ.



(a) General condition

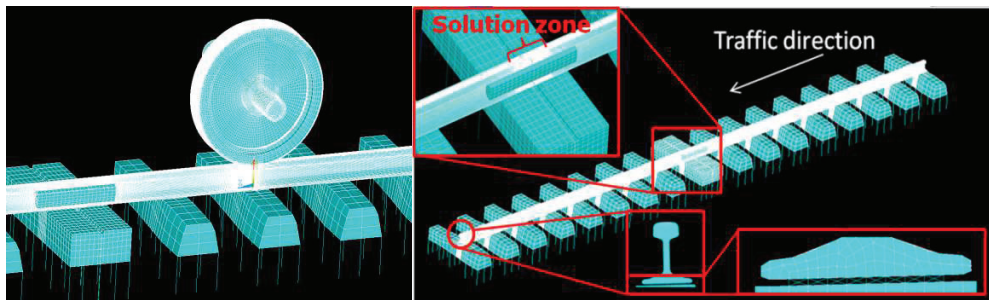
(b) Close-up of the end-post

Figure. 4.2: In situ condition of the target IRJ

4.2.2 Wheel-IRJ dynamic interaction model

Fig. 4.3 (a) shows the 3D explicit FE wheel-IRJ dynamic interaction model established in this study. This model is composed of a 10-m-long half-track with an IRJ in the middle and a half-wheelset with the sprung mass of the car body and bogie. The wheel geometry corresponds to that of a passenger car wheel of the Dutch railway with the standard profile of S1002. The IRJ, composed of 2 fishplates, 4 pairs of bolts and a 6-mm gap, was modelled in detail with fine meshes (see the close-up view at the upper left corner of Fig. 4.3 (b)). Because the value of elastic modulus of the end-post (insulation layer between two rail ends) is much lower than those of the rails and the presence of air gap (shown in Fig. 4.2 (b)) may result in free rail-end (Zong & Dhanasekar, 2014), the end-post layer was omitted in the model and simplified as a gap. Free boundaries were used on the rail ends at the joint, whereas non-reflecting boundaries were defined at the far ends of the rails. The wheel, rails, and sleepers were modelled using 8-node solid elements. Non-uniform meshing was used, and regular

discretization with a mesh size of 1 mm was allocated at the initial wheel-rail contact area and within the 0.2-m-long solution zone around the joint. The car body and bogie were modelled as mass elements connected to the wheelset by the primary suspension of the vehicle with parallel linear springs and viscous dampers. The two neighbouring timber sleepers beneath the IRJ and the concrete sleepers modelled elsewhere were differentiated by their geometries and material properties. The baseplate fastening system used on the timber sleepers and the Vossloh fastening system on the concrete sleepers were modelled by crossed spring and damper elements (see the close-up at the lower right corner of Fig. 4.3 (b)), and adopted different linear stiffness and damping parameters (see Table 4.1). The ballast was simplified as vertical spring and damper elements, with the displacements constrained in the lateral and longitudinal directions. Since the stiffness and damping parameters used to model the fastenings and ballast can hardly be measured directly in the field, these parameters were calibrated in this study by fitting the simulated frequency response functions (FRF) to the measurement results, which will be illustrated in detail in Section 4.3.2. Bi-linear elastoplastic material properties were applied to the wheel and rail models in the simulation of wheel/rail structural dynamic responses. The calibrated stiffness and damping parameters, as well as the nominal material properties applied in the model, are listed in Table 4.1.



(a) Wheel-IRJ interaction model

(b) Track model with IRJ (IRJ sub-model)

Figure. 4.3: Finite element wheel-IRJ dynamic interaction model

The transient impact contact simulation first employed a dynamic relaxation to allow the wheel-track system to reach an equilibrium state under gravity. The initial position of the wheel model was 1.32 m away from the IRJ (two standard sleeper spans and half a timber sleeper span as shown in Fig. 4.3). The rotation and forward translation movements of the wheel were applied as the initial conditions. Coulomb's law of friction was implemented for the wheel-rail contact pair with a friction coefficient of 0.35 (a typical intermediate value of rail top friction (Eadie *et al.*, 2003)). The wheel was subsequently driven by a torque applied on the axle to roll along the rail from the initial position towards the joint, thus generating a longitudinal creep force between the wheel and rail that satisfies the requirement that the traction coefficient is below the friction coefficient. Referring to the measurement, the simulated pass-by speed was 100 km/h and the impact vibration responses were calculated at the rail foot immediately after the joint in the model.

Table 4.1: The values of parameters used in the model

Parameters		Nominal values	Parameters		Calibrated values	
Rails and fishplates material	Young's modulus	210 GPa	Baseplate fastening	Vertical	Stiffness	86.7 MN/m
	Poisson's ratio	0.3			Damping	45000 Ns/m
	Density	7800 kg/m ³		Lateral	Stiffness	150 MN/m
	Yield stress	500 MPa			Damping	40000 Ns/m
	Tangent modulus	21 GPa		Vossloh fastening	Vertical	Stiffness
Young's modulus	20 GPa	Damping	67500 Ns/m			
Poisson's ratio	0.3	Lateral	Stiffness		100 MN/m	
Density	1300 kg/m ³		Damping		40000 Ns/m	
Timber sleeper material	Young's modulus	38.4 GPa	Ballast		Vertical	Stiffness
	Poisson's ratio	0.2		Damping		32000 Ns/m
	Density	2520 kg/m ³		bolt pretension		12.5 kN

4

Fig. 4.4 (a) and (b) show the meshes of rail top surface in the proximity to the joint before and after applying the measured geometry, respectively. The in situ geometry of the target IRJ was measured by a HandySCAN 3D laser scanner. The measured geometry is applied only to the vicinity of the joint rather than to the whole modelled rail surface for the simulations of wheel-rail dynamic interaction, because the impact vibration occurs transiently just when the wheel rolls over and hits the joint.

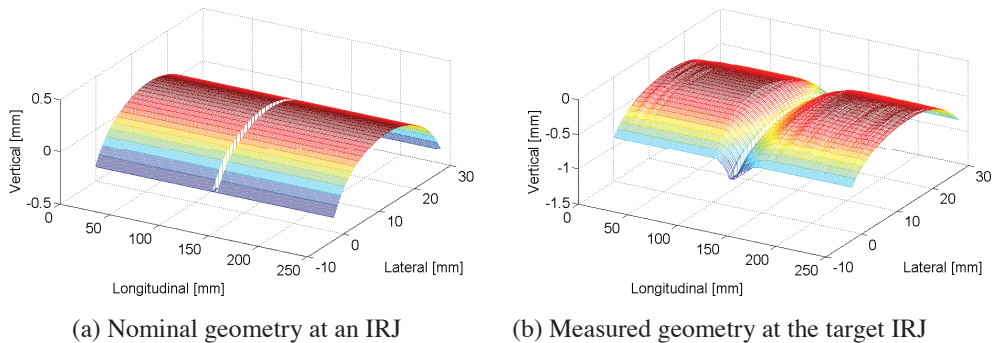


Figure. 4.4: Applying the realistic geometry to the IRJ (the size of the irregularity is exaggerated)

4.3 Validations of wheel & IRJ sub-models

In order to accurately predict the dynamic behaviour of the wheel-IRJ dynamic interaction model, this section first validated the dynamic behaviour of the track and wheel sub-models. The sub-model of the track with an IRJ, IRJ sub-model for short, was established corresponding to the target IRJ of Fig. 4.2. As shown in Fig. 4.3 (b), the IRJ sub-model excludes the wheel-sub model and car bodies presented in Fig. 4.3 (a).

The dynamic behaviour of track structures is generally characterised by frequency response functions (FRFs) due to the infinite structural nature (Thompson, 2009). Typical resonant frequencies of a track can be deduced according to its FRFs (Thompson & Vincent, 1995). Hammer test is a widespread method for the identification of the FRFs of track structures (Vincent & Thompson, 1995; De Man, 2002; Kabo *et al.*, 2006; Oregui *et al.*, 2015a), but its application specifically to IRJs is limited. Oregui *et al.* (2015c) performed a systematic hammer measurement on IRJs to assess their health conditions, but their work only investigated dynamic behaviour of the IRJs in the vertical direction.

This study conducted a more comprehensive hammer test to measure the FRFs, in terms of accelerances, of the target IRJ not only in the vertical direction but in the lateral direction as well. In this study, the measured direct accelerances (response and excitation are measured in the same direction and location (Maia & Silva, 1998)) are used to calibrate the stiffness and damping parameters involved in the FE IRJ sub-model by fitting their levels and resonant frequencies to the simulation results, as described in (De Man, 2002; Kabo *et al.*, 2006; Oregui *et al.*, 2015b; Oregui *et al.*, 2016); the measured transfer accelerances (response and excitation are measured in the same direction but different locations (Maia & Silva, 1998)), cross-accelerances (response and excitation are measured in different directions (Maia & Silva, 1998)) and decay rate of the track are then used to validate the dynamic behaviour of the calibrated track sub-model.

4.3.1 Set-up of the hammer test

Fig. 4.5 shows the set-up of the hammer test employed to identify the accelerances of the target IRJ. The FRFs of tracks without IRJs are normally measured at two track sections: on-support and mid-span (Thompson & Vincent, 1995; Vincent & Thompson, 1995; De Man, 2002; Kabo *et al.*, 2006; Oregui *et al.*, 2015a; Oregui *et al.*, 2015c), where different responses are expected. This study added a third section around the rail-end just after the IRJ along the train travel direction, where a significant dynamic impact can be expected during a train pass-by. Six accelerometers (B&K 4514, denoted as 1~6 in Fig. 4.5) were placed at the three sections: three on the rail top and the other three on the field side of the rail head (see the close-up of Fig. 4.5), respectively, used to measure the vertical and lateral responses. Two accelerometers (IMI623C00, ensuring electric insulation between two rails in the measurement, denoted as 7 and 8 in Fig. 4.5) were placed on the rail top before the joint, respectively at the sections of rail-end and on-support, to detect vibration transmission to the other side of the joint.

A hammer (PCB 086D05) with a hard metal tip (PCB 084B03) was used in the measurement to obtain high-frequency excitations. The hammer excitations were conducted as close as possible to the accelerometers 1~6, indicated by the red arrows 1~6 in Fig. 4.5. The excitation and response signals of 10 impacts were recorded at each hitting position. The spectra of the excitation loads at the six hitting positions, produced by averaging 10 impacts, are depicted in Fig. 4.6. The 3 dB drop (limit of very reliable range (De Man, 2002)) and 10

dB drop (limit of sufficiently reliable range (De Man, 2002)) occur at about 3.5 kHz and 5 kHz, respectively, indicating that the valid frequency range of the hammer-excited signals can reach up to 5 kHz.

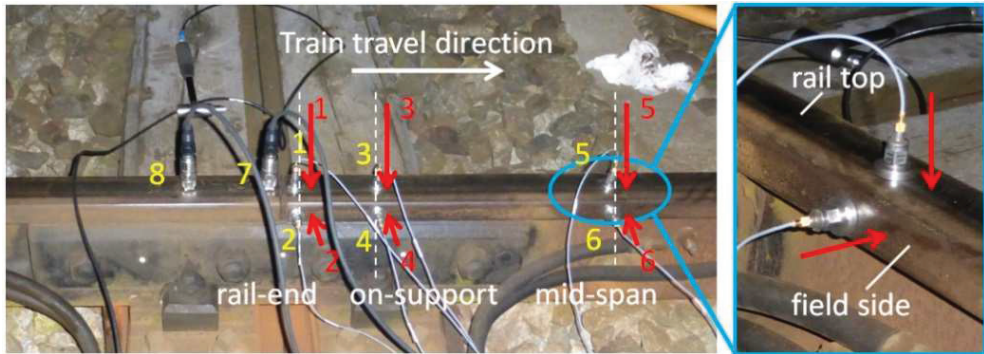


Figure. 4.5: Distribution of accelerometers and force excitation points

(The yellow numbers 1~8 denote the accelerometers placed at the IRJ and the red arrows 1~6 indicate the positions and directions of the hammer excitations)

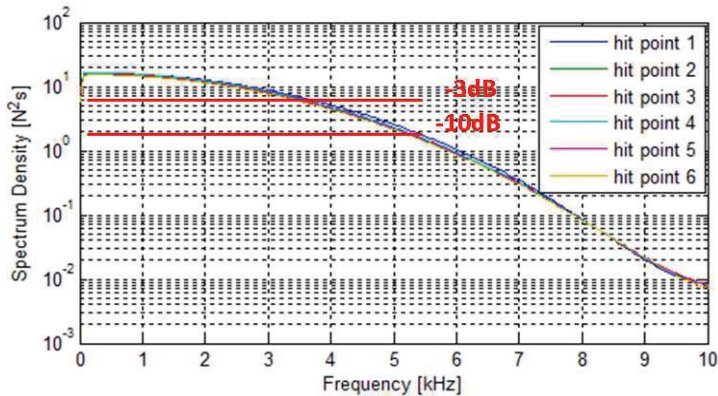


Figure. 4.6: Valid frequency range determined by the spectra of excitation forces

(within 3 dB drop: very reliable range; within 10 dB drop: reliable range (De Man, 2002))

The reliability of hammer test can be assessed by the coherence of the response signals excited by hammer impacts. Because the dynamic behaviour of the target IRJ under wheel-rail impacts is of particular interest in this study and wheel-rail impacts occur more or less at the rail-end section after the joint, the coherence of the response signals under the vertical hammer excitations at the position 1 (see Fig. 4.5) is presented here. The coherence curves of the response signals of the eight measurement points (denoted as 1~8 in Fig. 4.5) excited by the 10 hammer impacts at the position 1 are depicted in Fig. 4.7 (a) and (b). Excellent coherence over 0.9 in the whole frequency range of interest was obtained for the vertical responses (positions 1, 3, 5, 7, 8), whereas for the lateral responses (positions 2, 4, 6) lower coherence

was observed at certain frequency bands: around 360 Hz, 1160 Hz and over 3 kHz, probably due to that the cross-acceleration is more sensitive to the positions and directions of excitations and responses (Vincent & Thompson, 1995). The good coherence of the lateral responses excited by the hammer in the lateral direction in Fig. 4.7 (c) indicates the testing signals in the lateral directions are also reliable.

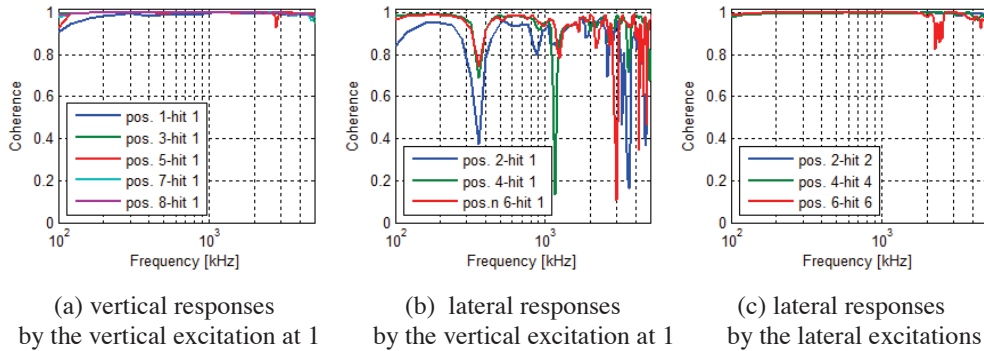
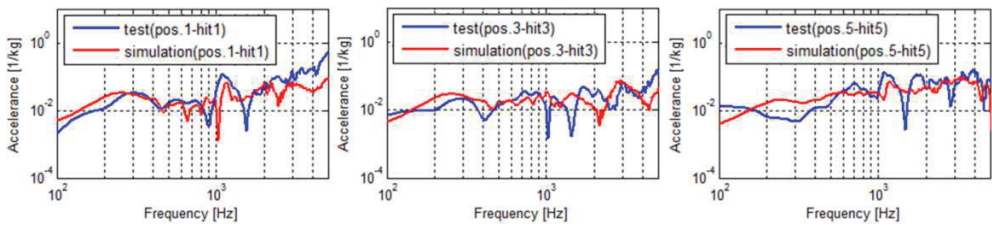


Figure. 4.7: Coherence curves of the responses at the eight measurement points

4.3.2 Calibration of the IRJ sub-model

As indicated by the coherence analysis, the direct accelerances and transfer accelerances were more reliably measured than the cross-accelerances. This study thus applied the measured direct accelerances as the reference to calibrate the stiffness and damping parameters involved in the FE IRJ sub-model. The accelerances of the IRJ sub-model were calculated by reproducing the hammer test with an explicit time integration method, as illustrated by Oregui *et al.* (2016). The simulated excitations were applied in both the vertical and lateral directions at the three sections of the IRJ sub-model, respectively, as the measurement.

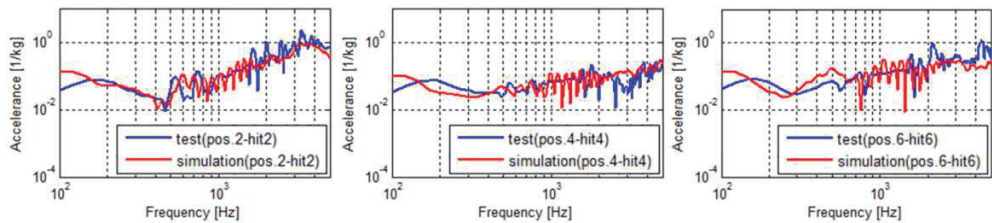
The closest fits of the simulated and measured vertical and lateral direct accelerances are depicted in Figs. 4.8 and 4.9, respectively. The measurement results shown here are the averages of the 10 times hammer-excited signals. Fig. 4.8 shows that the tendencies and resonant frequencies of the simulated vertical accelerances match the measurement. The measured typical track (anti-) resonances of the f_2 (rail mass on the fastening stiffness (Vincent & Thompson, 1995)), f_a (sleepers vibrate on the ballast and pad stiffness (Vincent & Thompson, 1995)), first and second order vertical pinned-pinned of the target IRJ are 280 Hz, 440 Hz, 1050 Hz and 2750 Hz, respectively, whereas those from the simulation are 260 Hz, 460 Hz, 1100 Hz and 2550 Hz, respectively. The vertical acceleration of the rail-end section is similar to that of the on-support section between 200 and 600 Hz, in which frequency range a rail behaves like a mass and its dynamic behaviour is mainly dominated by supports (Thompson, 2009). Over 4 kHz, the response of the rail-end section is evidently higher than the other two sections, presenting a high-intensity dynamic feature. That is probably related to the reduction of the vertical structural stiffness at the joint, which is similar to the free end of a cantilever beam (Kitagawa *et al.*, 2015).



(a) Rail-end (position 1) (b) On-support (position 3) (c) Mid-span (position 5)

Figure. 4.8: Fitting vertical accelerances (red line: simulation; blue line: test)

The general levels of the lateral direct accelerances shown in Fig. 4.9 are higher than the vertical ones shown in Fig. 4.8. The tendencies and levels of the measured and simulated lateral direct accelerances are well fitted in Fig. 4.9. The lateral pinned-pinned resonance, less pronounced than the vertical one, occurs at about 550 Hz in the measurement and 600 Hz in the simulation. More oscillations can be observed in the simulation results between 600-1300 Hz, which could be influenced by the modelling of the fastening systems. Although an improved fastening model represented by crossed linear spring and damper elements managed to take account of the lateral dynamics, it failed to fully reproduce the modes of real fastenings comprised of rail pads and clamps (Oregui *et al.*, 2015b). The deviation at the low frequency below 200 Hz is probably related to the simplification of the ballast model, whose displacements were constrained in the lateral and longitudinal directions.



(a) Rail-end (position 2) (b) On-support (position 4) (c) Mid-span (position 6)

Figure. 4.9: Fitting lateral accelerances (red line: simulation; blue line: test)

It can be concluded from the analysis of the direct accelerances that the dynamic behaviour of the rail-end section has a high-intensity feature due to the reduction of bending stiffness. The stiffness and damping parameters calibrated by the direct accelerances are then adopted in the simulations of the transfer accelerances and cross-accelerances, track decay rate and wheel-rail impact at the target IRJ.

4.3.3 Validation of transfer and cross-accelerances

The vibration responses of the IRJ under the vertical hammer excitation at the rail-end section (position 1 in Fig. 4.5) are studied for the IRJ sub-model validation. The transfer and cross-accelerances, including phases, simulated by the calibrated IRJ sub-model are compared with the measurement in Fig. 4.10. Good agreements for the transfer accelerances and reasonable agreements for the cross-accelerances are achieved. The deviations of the cross-accelerances at 120 Hz and 500-1300 Hz are believed caused by the simplification of the

ballast model and the linear spring/damper representations of the rail pads models, respectively, as analysed in the lateral direct accelerances.

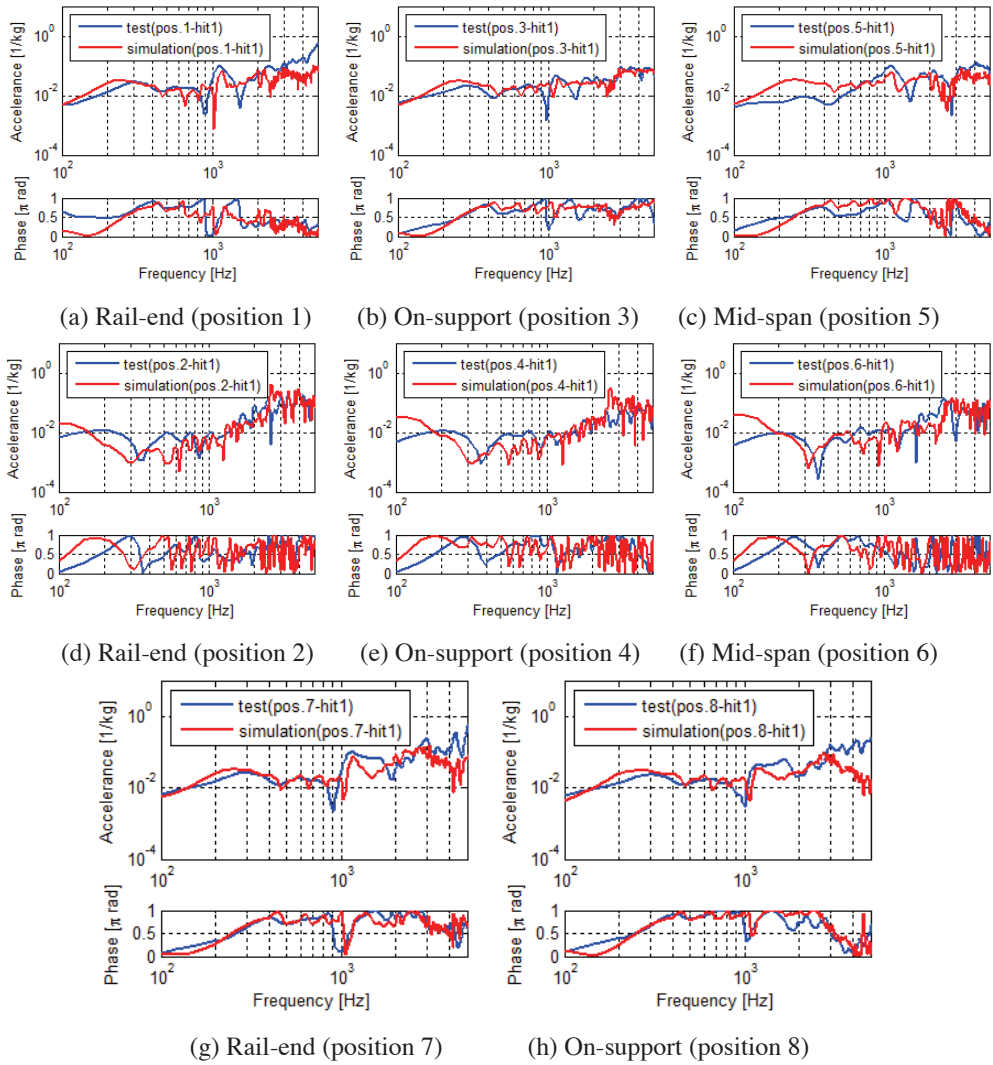


Figure. 4.10: Validations of transfer and cross-accelerances (red line: simulation; blue line: test. transfer accelerances: (a)-(c) and (g)-(h); cross-accelerances: (d)-(f))

4.3.4 Validation of decay rate

The validation of track decay rate influenced by the damping of the track system (Yang & Thompson, 2014) is also important for the accurate prediction of track dynamic behaviour. Owing to the reciprocity, the decay rate of a track with periodical structural characteristics is normally measured by a roving hammer method for operational convenience ("Railway applications - Noise emission - Characterisation of the dynamic properties of track sections for pass by noise measurements," 2010). The comparison of the transfer accelerances measured at the on-support (position 3) and mid-span (position 5) sections shown in Fig. 4.11 (a) indicates the reciprocity can be basically obeyed there, whereas Fig. 4.11 (b) and (c) show that the reciprocity can hardly be satisfied at the rail-end section in the high-frequency range over 3 kHz. Therefore, this study employed a roving sensor approach to measuring the decay rate of the target IRJ. The hammer excitations were exerted at the rail-end section after the joint (position 1 in Fig. 4.5), where wheel-IRJ impacts are expected to occur; Nine accelerometers (B&K 4514, denoted as 1~9 in Fig. 4.12) were employed in the measurement and a 5-meter section of the track (8 sleeper spans) just after the IRJ could be covered by roving the sensors once. Referring to the hammer excitation positions suggested in the roving hammer test of decay rate ("Railway applications - Noise emission - Characterisation of the dynamic properties of track sections for pass by noise measurements," 2010), the sensor distribution schemes adopted in this study are shown in Fig. 4.12 (a), and the corresponding in situ conditions are shown in Fig. 4.12 (b) and (c).

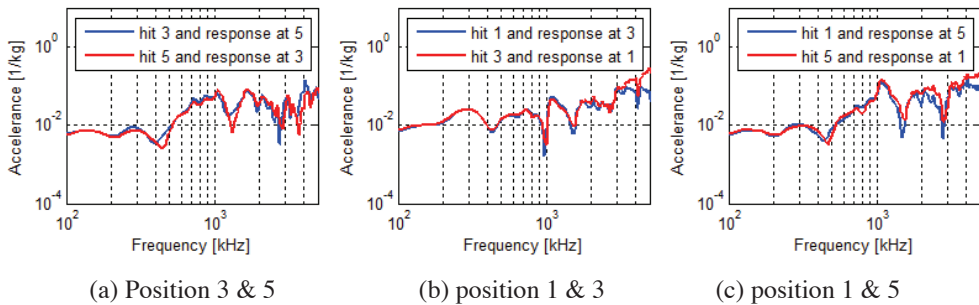
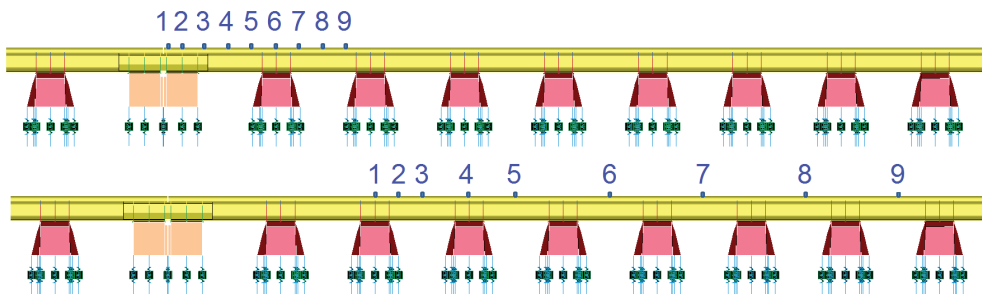


Figure. 4.11: Comparisons of measured transfer accelerances



(a) Sketch of sensor distributions before (upper graph) and after (lower graph) roving



(b) Sensor distribution before roving

(c) Sensor distribution after roving

Figure. 4.12: Sensor distribution schemes in the decay rate test

The hammer test of the decay rate was also reproduced by the proposed FE IRJ sub-model with an explicit time integration method. Fig. 4.13 compares the time histories of the simulated vibration of the 18 response positions (9 sensors \times 2 rounds) with those obtained by the measurements. The measurement results shown here are also the averages of the 10 times excitations, as the accelerances analysed above. Good agreements can be observed in the vast majority of the comparisons. The simulated and measured vertical decay rates of the target IRJ are calculated based on these vibration responses (Jones *et al.*, 2006) and compared in Fig. 4.14. Good agreements in terms of the peak, trough and average level in the comparison of the decay rate again validate the dynamic behaviour of the presented FE IRJ sub-model. The decay rate peaks at about 3 kHz and troughs at about 900 Hz and 4 kHz.

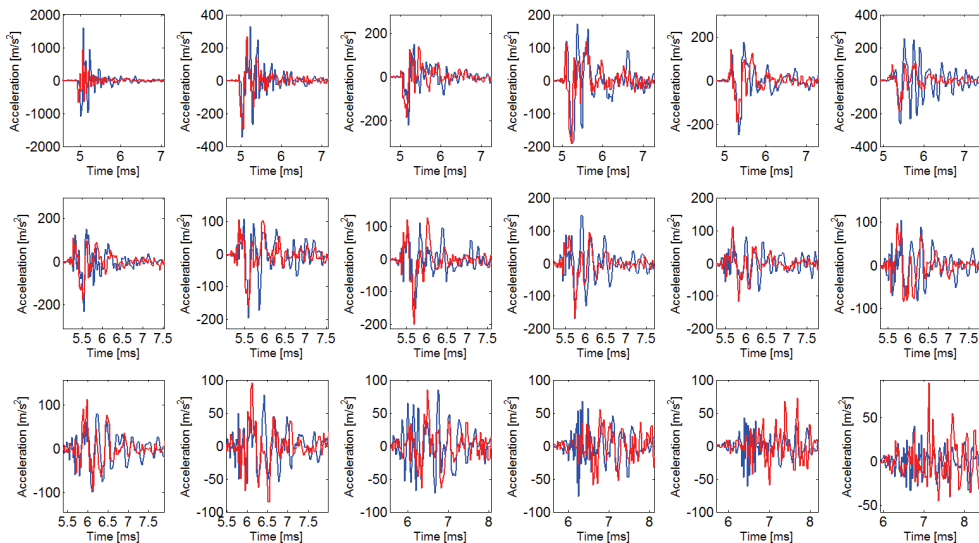


Figure. 4.13: Comparison of acceleration responses (red line: simulation; blue line: test)

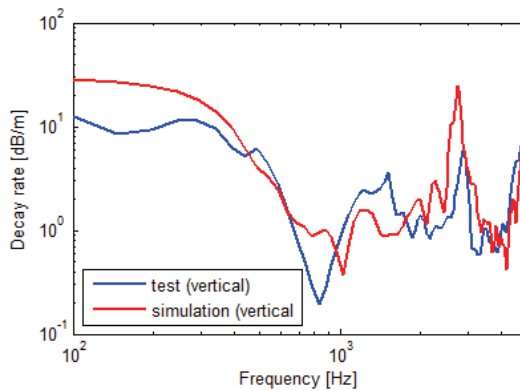
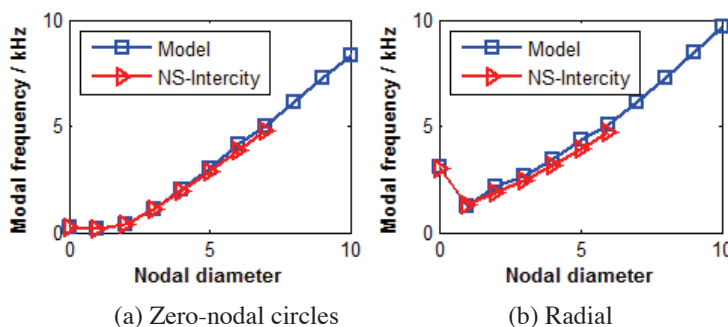


Figure. 4.14: Validation of decay rate (red line: simulation; blue line: test)

4.3.5 Validation of the wheel sub-model

Although the dynamic behaviour of wheels may also be characterised by FRFs (Wu & Thompson, 2002), this study (also for the wheel models used in Chapter 5 and 6) characterised the dynamic behaviour of the FE wheel sub-mode by the modes and corresponding natural frequencies and validated them against a measurement reported in (Thompson, 2009), because the material damping of a wheel is generally very low and the exact value of the wheel modal damping is not critical (Thompson, 2009). The frequency range of interest is 10 kHz in this study. All modes of the wheel sub-model within the frequency range of interest were identified by a modal analysis. For this, the same half-wheelset model as the explicit FE model shown in Fig. 4.3 (a) was used with the inner edge of its hub clamped. The calculated wheel modes under such a boundary condition can adequately represent the wheel dynamics under contact with the rail (Glocker *et al.*, 2009). The identified natural frequencies of the axial and radial wheel modes are plotted in Fig. 4.15. Good agreement is observed when comparing the calculated results with the experimental wheel natural frequencies from (Thompson, 2009), in which an NS-intercity wheel is measured for up to 5 kHz. All of these physical modes can be naturally included in the transient dynamic simulation when using the full FE model and a small time step (Zhao & Li, 2011).



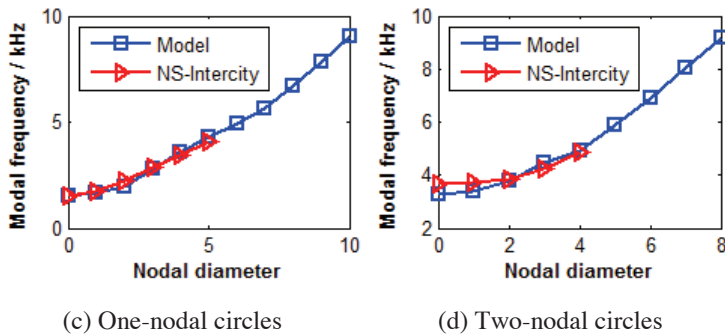


Figure. 4.15: Wheel modes calculated by a finite element modal analysis (blue) compared with the measured results (red, from (Thompson, 2009))

4.4 Validation of pass-by vibration

The validations of the IRJ and wheel sub-models enable the FE dynamic interaction model for a transient impact simulation. The simulated pass-by impact vibration is compared to the measurement results from a pass-by measurement in this section. A pass-by measurement with a travelling speed of about 100 km/h was performed on the target IRJ on 19th February 2015. The vertical and lateral impact vibration, collected on the rail foot just after the joint (see Fig. 4.16), were measured by accelerometers PCB 352A60 (measurement range: ± 4950 m/s²; frequency range (± 3 dB): 5 Hz-60 kHz) and B&K 4514 (measurement range: ± 980 m/s²; frequency range (± 6 dB): 5 Hz-10 kHz), respectively.



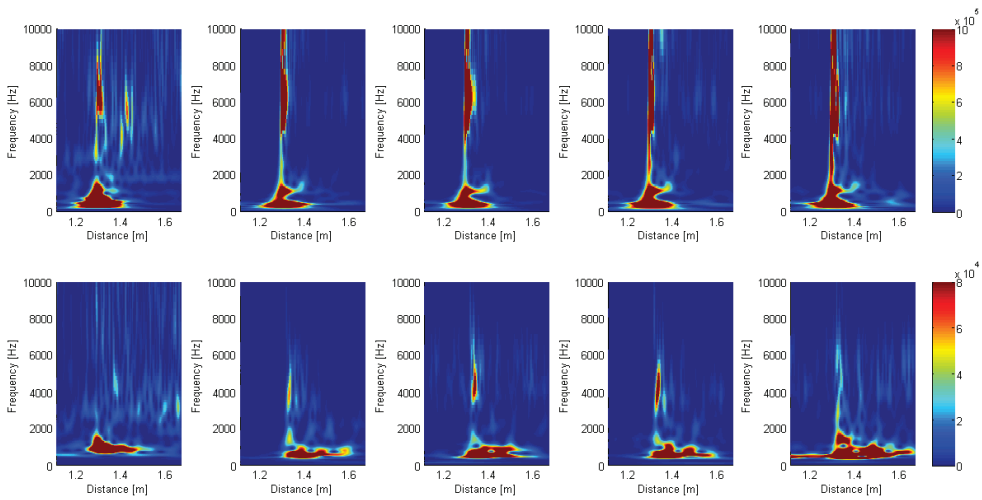
Figure. 4.16: Set-up of accelerometers used to measure impact vibration

The pass-by measurement conducted at the target IRJ was reproduced by the 3D FE wheel-IRJ dynamic interaction model shown in Fig. 4.3 (a) with explicit time integration. A small time step (49 ns) was employed to meet Courant stability condition (Courant *et al.*, 1967). This, together with the fine meshing scheme applied in the model, guaranteed that high-frequency dynamic effects up to 10 kHz or higher can be reproduced. The effects of transient wheel rotation were also included inherently.

Wavelet power spectrum (WPS) is considered appropriate for the investigation of non-stationary signals with local changes in the frequency components (Molodova *et al.*, 2014). The WPSs of the simulated and measured impact vibration up to 10 kHz are compared on the same scale in Fig. 4.17. The results of the four pass-bys shown in Fig. 4.17 were successively measured when the four wheelsets of a coach passed the target IRJ. It can be seen that the

simulated impact vibration agrees well with the pass-by measurement results in both the time domain and frequency domain. The good agreement of the impact vibration is based on the results of the sub-models validation and also demonstrates the accuracy of them. Both the measurement and simulation indicate that energy of the vertical impact vibration (upper row in Fig. 4.17) mainly concentrate on around 300 Hz and 1 kHz, corresponding to the f_2 and first order pinned-pinned resonance, respectively. Typical impact vibration feature is shown by the WPSs of the vertical rail vibration: a prominent high-frequency energy concentration with a broadband from 4 kHz to 10 kHz or higher occurs transiently just at the wheel-IRJ impact. The WPSs of the lateral impact vibration (lower row in Fig. 4.17) imply that the dominant frequencies of the simulated lateral impact vibration range from 600-1200 Hz, slightly higher than the measurement results of 550-1000 Hz. These dominant frequency ranges may be associated with the lateral pinned-pinned resonance, as the simulated and measured lateral pinned-pinned resonances occur at approximately 600 Hz and 550 Hz, respectively, in line with the lower boundaries of the dominant frequency ranges of the lateral impact vibration. High-frequency components in the lateral impact vibration are much less pronounced than the vertical ones and vary to some extent in the frequency range. This variation can be attributed to the randomness of the traffic, such as differences in wheel (worn) profile, suspension condition, hunting motion etc.

4



(a) Simulation (b) First pass-by (c) Second pass-by (d) Third pass-by (e) Fourth pass-by

Figure. 4.17: WPSs of the simulated and measured pass-by impact vibration

(upper row: vertical impact vibration; lower row: lateral impact vibration; the unit of the colour bar is m/s^2)

4.5 Impact forces and contact solutions

The ability of the wheel-IRJ dynamic interaction model in simulating the dynamic behaviour of an IRJ has been validated in previous sections. This section presents and analyses transient contact solutions of wheel-rail frictional rolling impacts calculated by the validated model. The time histories of the normal contact forces calculated by the three simulations

tabulated in Table 4.2 are presented at the beginning of this section in order to provide a broad overview of the wheel-rail impact contact at an IRJ. Typical transient contact solutions calculated within the solution zone are then analysed, including the contact patch area, stress magnitude and direction, micro-slip and adhesion-slip distributions. The influences of the rail surface geometries and material models on the wheel-rail contact solutions are also discussed. The transient contact solutions obtained in this study captured wave phenomena, which will be presented and analysed in Section 4.6.

Because the railhead surface geometries vary with the operational time and each IRJ, the measured geometry may impose randomness on the simulated impact contact solutions. Moreover, the material properties of contact bodies also influence the wheel-rail contact solutions (Deng *et al.*, 2015; Zhao & Li, 2015). Therefore, in addition to the simulation conducted by the measured-geometry model in Section 4.4, two additional simulations were performed using nominal-geometry models, with one simulating elastic materials and the other simulating elastoplastic materials, to gain an overall understanding of the transient contact behaviour of wheel-IRJ impacts.

The setup parameters of the three simulations conducted in this study are listed in Table 4.2, and simulation 3 was the one performed to predict impact vibration. Table 4.3 lists the values of the material parameters used in the simulations. The elastoplastic material model applied in the study corresponds to the R260Mn rail steel that is widely used in the Dutch railway.

Table 4.2: Parameters of the simulations with different set ups

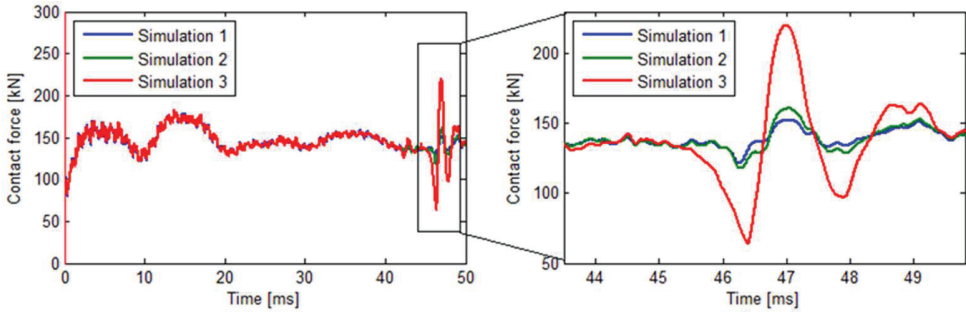
	Material	Profile
Simulation 1	Elastic	Nominal
Simulation 2	Elastoplastic	Nominal
Simulation 3	Elastoplastic	Measured

Table 4.3: Values of the materials

Elastoplastic material parameters		Values
Elastic part	Young's modulus	210 GPa
	Poisson's ratio	0.3
	Density	7800 kg/m ³
Plastic part	Yield stress	500 MPa
	Tangent modulus	21 GPa

4.5.1 Wheel-IRJ impact contact force

The time histories of the normal wheel-rail contact forces calculated by the three simulations are plotted in Fig. 4.18 (a), which shows that obvious impact contact occurred when the wheel rolled over the joint at approximately 47 ms. The damping in the system dissipated the initial kinetic and potential energy originating from any initial in-equilibrium of the system such that the oscillations were damped out to less than 10% of the static values upon arriving at the solution zone. The close-up view of the time histories around the impact plotted in Fig. 4.18 (b) shows the simulated normal impact loads within the solution zone. The figure shows that the impact simulated with the measured geometry (simulation 3) was much larger than those simulated with the nominal geometry. In addition, a comparison of the normal loads calculated by simulations 1 and 2, which only differ in the material properties, shows that the elastoplastic material model (simulation 2) provided a slightly higher impact magnitude than the elastic model (simulation 1).



(a) Overview of the simulated contact forces (b) Impact contact forces in the solution zone

Figure. 4.18: Time history of the wheel-rail contact force

As reported in Section 4.4, the wheel-IRJ dynamic interaction simulation in this study employed a small computational time step (49 ns). By applying explicit central difference time integration and a surface-to-surface contact-searching scheme illustrated in Chapter 2, nodal force and motion in the solution zone were calculated for each time step. Certain nodal force and motion were subsequently output and used to calculate the transient solutions of impact contact. A small output time step (1 μ s) was used in this study to capture high-frequency dynamic effects up to 500 kHz in the transient solutions of impact contact. Transient contact solutions of 6300 output time steps, specifically from 43.5 ms to 49.8 ms (abscissa range of Fig. 4.18 (b)), were calculated for each simulation.

4

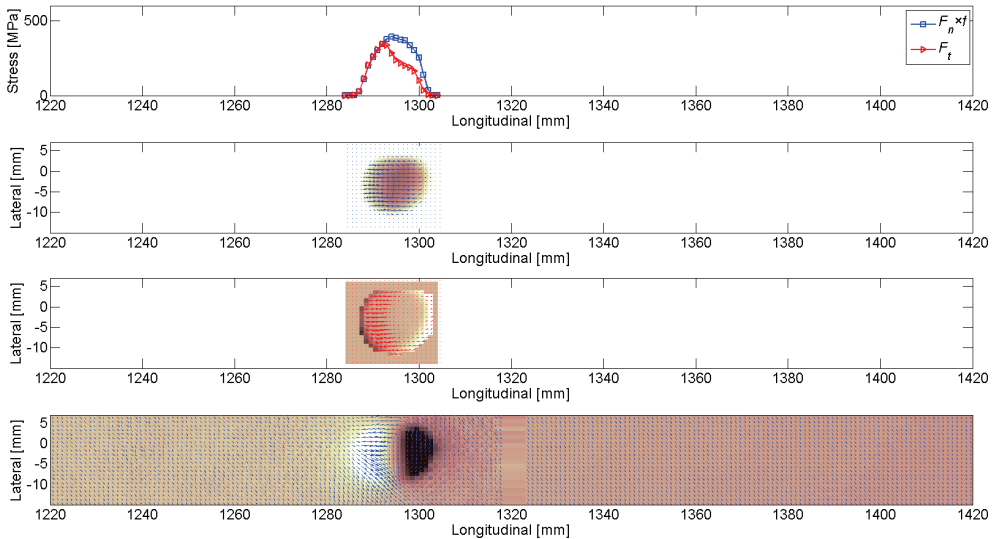


Figure. 4.19: Example of the transient contact solution (graphs from top to bottom: stress distributions along the longitudinal centre line, stress distributions within the contact patch, micro-slip distribution, and rail surface nodal velocities within the whole solution zone)

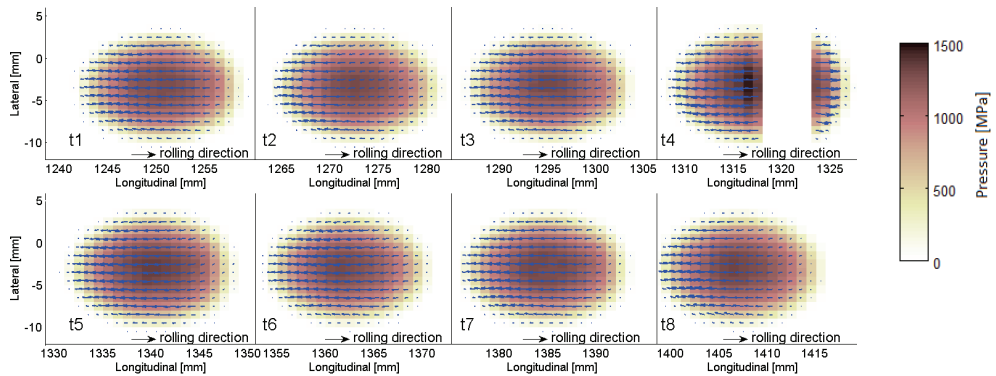
An example of a transient contact solution calculated by simulation 3 that was output at instant 45.613 ms (output time step=2113) is displayed in Fig. 4.19. From the top to the bottom, the graphs show the simulated stress distributions along the longitudinal centre line of the contact patch, stress distributions within the contact patch, micro-slip distributions and rail surface nodal velocities within the whole solution zone. Animations ("Animation for Fig. 4.25, <https://youtu.be/tWyWKw9XxRI> ; " ; "Animation for Fig. 4.27, <https://youtu.be/fAg99j6kquI> ; [accessed 16.11.22] " ; "Animation for Fig. 4.28, <https://youtu.be/eHh24SnWDFQ> ; [accessed 16.11.22] ") were created from the plots of the contact solutions of a certain amount of time steps, and they clearly show the evolution of the contact solutions along with certain high-frequency dynamic effects. Typical transient contact solutions are selected and analysed in the following sections to demonstrate the characteristics of the transient solutions of impact contact.

4.5.2 Evolution of contact areas and stresses distributions

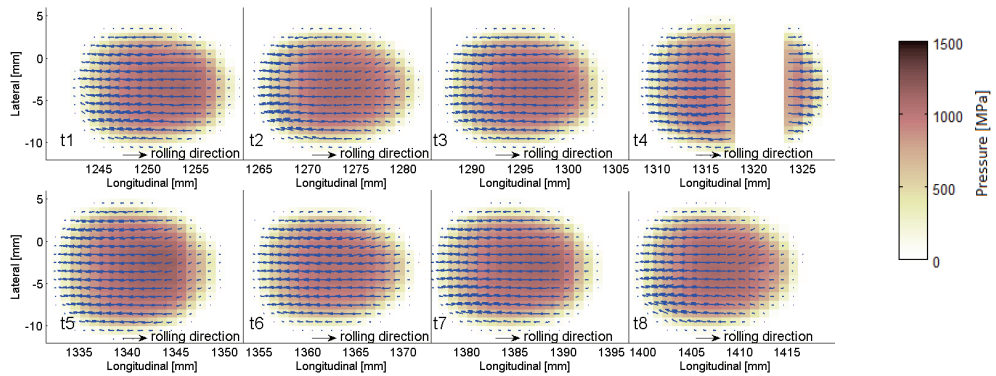
The evolution of the contact pressure together with the direction and magnitude of the surface shear stress calculated by the three simulations are plotted in the contour/vector diagrams in Fig. 4.20. The contact patch area can be determined via the contact pressure: an element is in contact if the contact pressure is non-zero. Thus, the evolution of the contact patch area can also be observed from Fig. 4.20. Eight time steps ($t_1 \sim t_8$) with a fixed interval of 0.77 ms (770 times the output time step) between two consecutive time steps are displayed for each simulation to show the main characteristics of the impact contact area and the stress evolution. The origin of the coordinate system was at the centre of the rail bottom surface at the initial position of the wheel-rail contact. Because the coordinate system included the rail inclination of the track, the longitudinal centre lines of the contact patches shown in Fig. 4.20 are at approximately -3 mm in the lateral direction rather than at 0 mm. The contact pressure magnitude corresponds to the depth of colour within the contact patch as indicated by the colour bar. The surface shear stresses are indicated by blue arrows. The arrows point in the direction of the shear stress and the arrow length is proportional to the magnitude.

In Fig. 4.20 (a) and (b), other than the discontinuous contact at the joint at t_4 , the contact patch areas calculated by both the elastic (simulation 1) and elastoplastic models (simulation 2) correspond well with those reported in (Deng *et al.*, 2015; Zhao & Li, 2015). The wheel-rail contact areas simulated by the elastic model have elliptical shapes, whereas those simulated by the elastoplastic model have 'egg' shapes, with the trailing parts of the contact patches enlarged because plastic deformation has occurred in the rear (Zhao & Li, 2015).

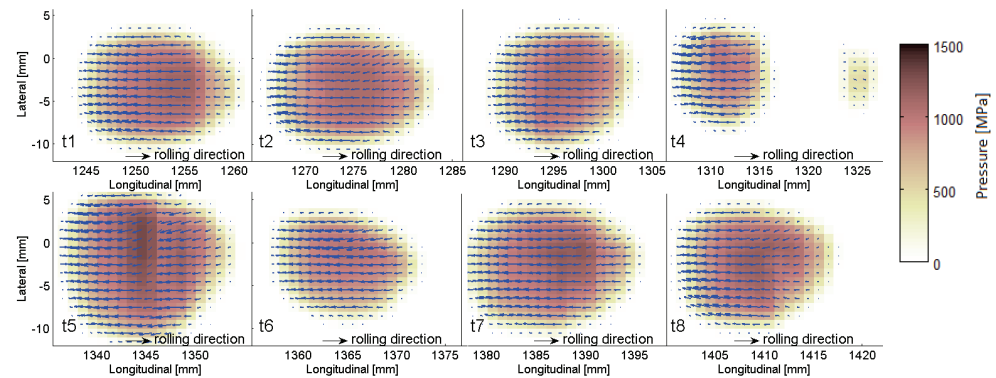
Although simulation 1 produced the smallest impact force (Fig. 4.18 (b)), the amplitudes of the contact pressures calculated by simulation 1 are larger than those calculated by the other two simulations as indicated by Fig. 4.20 because simulation 1 had the smallest contact areas. The magnitudes of the contact pressure located approximately in the middle of the contact patch in Fig. 4.20 (a) but in the leading section in Fig. 4.20 (b) are also consistent with the results reported in (Deng *et al.*, 2015; Zhao & Li, 2015). The simulated contact patch areas in Fig. 4.20 (a) and (b) basically remain steady and increase to some extent during the impact at t_4 and t_5 . This phenomenon is more evident under the elastoplastic material condition.



(a) Simulation 1 (elastic material & nominal geometry): elliptical contact patch



(b) Simulation 2 (elastoplastic material & nominal geometry): 'egg-shaped' contact patch

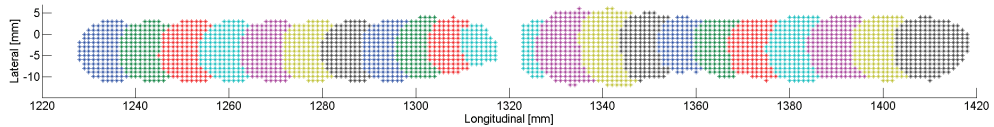


(c) Simulation 3 (elastoplastic material & measured geometry): non-steady-state contact patch

Figure. 4.20: Evolution of the impact contact area and stresses distribution

Simulation 3 provided more obviously non-steady-state contact solutions as shown in Fig. 4.20 (c). The contact areas and stress distributions vary considerably with the time step due to the geometric irregularity of the rail top surface and significant impact. The contact patches at

t_1 and t_2 in Fig. 4.20 (c) are similar to those at the same time steps in Fig. 4.20 (b). Subsequently, the area of the contact patch decreases at t_3 and t_4 because of the geometric declivity before the joint (see Fig. 4.4 (b)). The contact area increases remarkably during the impact contact at t_5 and then shrinks at t_6 , when the wheel has a tendency to bounce. The rail surface geometric irregularity contributes to the irregular shapes of the contact patches, which are neither elliptical nor ‘egg’ shaped, as well as the irregular stress distributions in Fig. 4.20 (c).



(a) ‘Footprints’ of the contact patch calculated by simulation 3 (the colour differentiates an individual contact patch from the others, and the interval between each two consecutive patches is 0.3 ms)



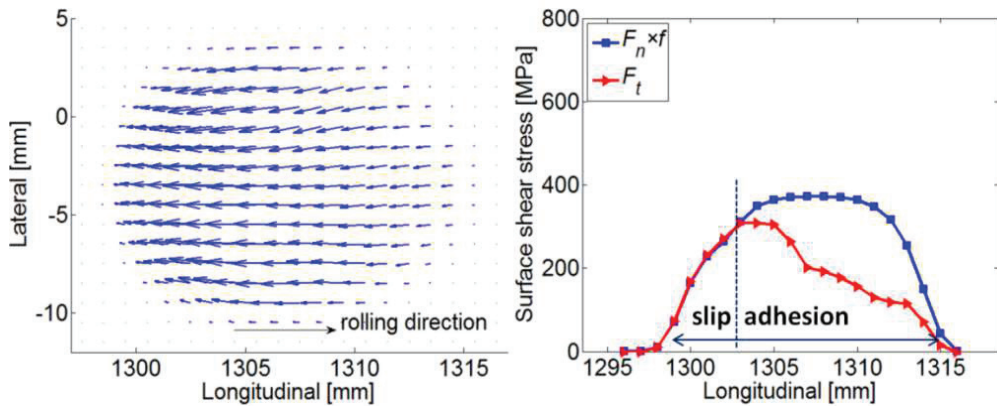
(b) In situ condition of the running band around the target IRJ

Figure. 4.21: Comparison of the simulated contact patch ‘footprints’ and in situ running band

By plotting a trail of transient contact areas, the ‘footprints’ of the contact patch calculated by simulation 3 are presented in Fig. 4.21 (a). The interval between each two consecutive contact patches is 0.3 ms (300 times the output time step). Good correspondence can be obtained by comparing the simulated ‘footprints’ to the in situ running band of the target IRJ shown in Fig. 4.21 (b). The ‘footprints’ become narrow at the region just before the joint (1310-1317 mm) in Fig. 4.21 (a), which corresponds to the cut-off of the running band (at approximately 1310 mm) in Fig. 4.21 (b). Wheel-IRJ impacts (the first peak of the contact force in Fig. 4.18 (b)) occur at approximately 1330-1350 mm, where the ‘footprints’ are larger in Fig. 4.21 (a), and a broader running band and a brighter spot can be found in Fig. 4.21 (b). The second wheel-rail impact (the second peak of the contact force in Fig. 4.18 (b)) occurs at approximately 1380-1390 mm, where larger than usual contact patches and a brighter spot can be observed in Fig. 4.21 (a) and (b), respectively, although they are less pronounced than those in the first impact. The good correspondence between the simulated contact patch ‘footprints’ and in situ running band implies that simulation 3 (with the measured geometry) can more accurately reproduce the transient impact contact solutions at the target IRJ, which is likely in a non-steady state.

4.5.3 Positive surface shear stress

When a wheel rolls along a rail driven by a torque at the axle, the shear stress direction on the rail surface is generally opposite to the wheel rolling direction. An example is shown in Fig. 4.22 (a), in which the rail surface shear stress distribution was calculated via simulation 2 at instant 46 ms (output time step=2500). By extracting the surface shear stress along the longitudinal centre line of the contact patch and comparing it to the traction bound (the product of the contact pressure F_n and friction coefficient f), the distribution of the adhesion-slip regions can be obtained, as shown in Fig. 4.22 (b). The maximum amplitude of the surface shear stress is located at the juncture of the adhesion and slip regions. The adhesion-slip distribution within the contact patch will be analysed in detail in the next section.



(a) Distribution within the contact patch (b) Distribution along the longitudinal axis

Figure 4.22: Example of the surface shear stress distribution

In this study, the direction of the surface shear stress opposite to the direction of wheel rolling is defined as negative and that along the direction of wheel rolling is defined as positive. A review of the evolution of stress distribution shown in Fig. 4.20 indicates that as the counterforce of the traction causes the wheel to move forward, the simulated surface shear stress points in the negative direction for the majority of graphs except at the regions immediately after the joint (roughly 1323-1327 mm) at t_4 . To show this phenomenon more clearly, an evolution of the surface shear stress distribution within the contact patch calculated by simulation 2 with a smaller time step (0.1 ms, 100 times of the output time step) than that used in Fig. 4.20 (0.77 ms) is depicted in Fig. 4.23. The evolution calculated by simulations 1 and 3 (not presented here) shows the same trend.

As shown in Fig. 4.23, when the wheel just touches the right rail after the joint (T1~T3), the shear stress vectors on the right rail are positive, whereas those on the left rail are negative. From T4 to T6, as the contact patch moves, the amplitudes of the positive shear stresses on the right rail between 1325 mm and 1329 mm decrease to zero and then become negative. Graphs of T4 and T5 also indicate that the lateral shear stress plays an important role at these moments, especially at locations close to the top and bottom edges of the contact patch, where the surface shear stress vectors point outwards. Such stress may exacerbate material flow on the railhead and consequently widen the running band at the impact location as shown in Fig.

4.21 (b). At the instances of T7 and T8, the contact patch has exited the positive surface shear stress region and all the stress vectors point in the negative direction. The occurrence of transient positive surface shear stress on the right rail end is shown to result from the impact contact at the IRJ with discontinuous geometry. In the region immediately after the joint, the amplitudes of the positive shear stresses caused by the wheel-IRJ impact are larger than the amplitudes of the original negative shear stresses (counterforce of the traction), thus making the resultant surface shear stresses positive.

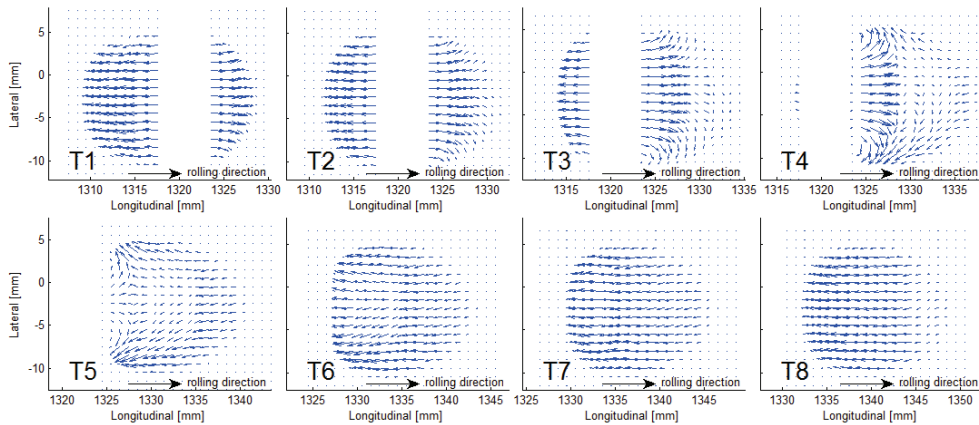


Figure. 4.23: Evolution of the surface shear stress calculated by simulation 2

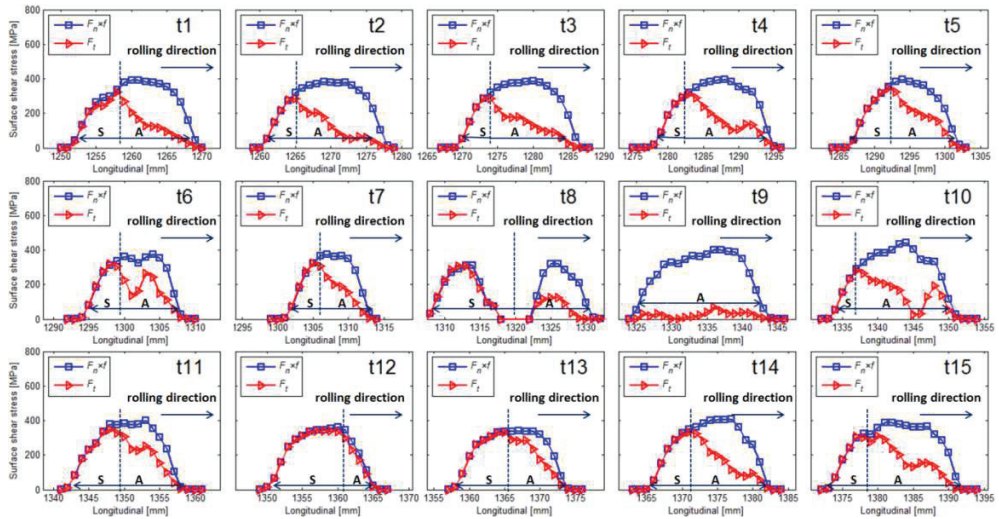
This study on the wheel-IRJ impact modelled a wheel driven by a torque on its axle. When a braking wheel rolls on a section of track with an IRJ, the original direction of the rail surface shear stresses is expected to be positive (counterforce of the braking force). In such cases, the positive shear stresses imposed by impact will be added to the original positive shear stresses. To what extent an impact between a braking wheel and an IRJ can influence the surface shear stress distribution and the consequent wear behaviour on the railhead after the joint should be studied in the future.

4.5.4 Adhesion-slip distribution and micro-slip

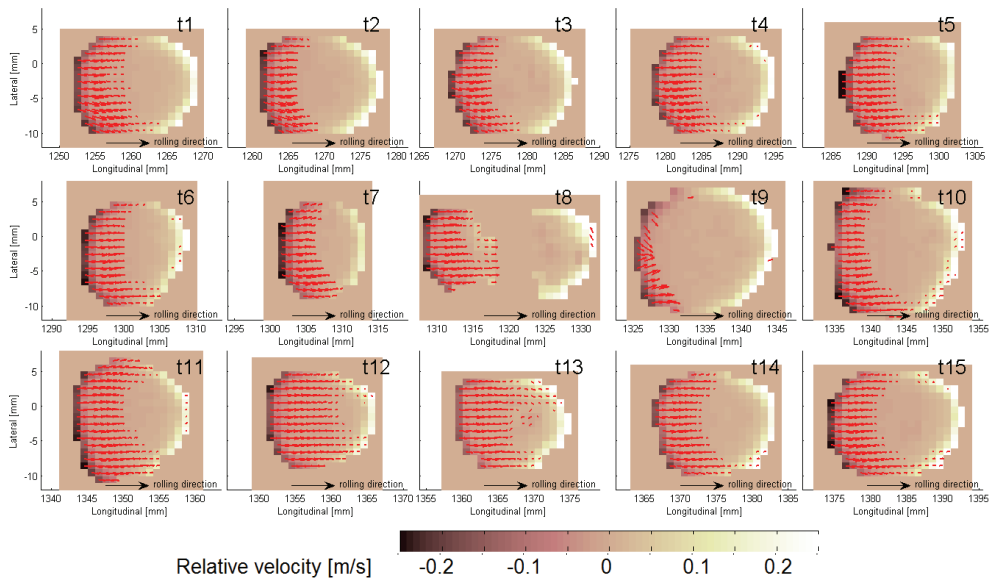
The division between adhesion and slip regions in the contact patch is an important feature of frictional rolling contact. The transient contact solutions that indicate the adhesion-slip distribution during the wheel-IRJ impact predicted by simulation 3 are presented in this section. The adhesion-slip distribution can be determined either by comparing the surface shear stress with the traction bound or by calculating the micro-slip within the contact patch (see Section 3.4.3). The simulated adhesion-slip distributions determined by these two approaches are consistent with each other, as shown in Fig. 4.24.

Fig. 4.24 (a) displays comparisons of the surface shear stress and traction bound along the longitudinal centre line of the contact patch at 15 instants. Instant t1 is equal to 44.4 ms, and the interval between each two consecutive instants is 0.3 ms (300 times of the output time step). Fig. 4.24 (b) shows the evolution of the micro-slip distribution within the contact patch at the same 15 instants. The red arrows point in the direction of the micro-slip and the arrow length is proportional to the magnitude. The micro-slip vectors (slip region) occur at the

trailing part of the contact patch, and their directions largely correspond to the wheel rolling direction. The colour depth within the contact patch indicates the magnitude of the normal wheel-rail relatively velocity. The colour outside the contact patch corresponds to a zero relative velocity, whereas that at the leading and trailing edges of the contact patch are lighter and darker, indicating a positive and negative normal relative velocity, respectively.



(a) By stress distribution (A: adhesion region; S: slip region)



(b) By micro-slip distribution

Figure. 4.24: Evolution of the adhesion-slip distributions calculated by simulation 3

The adhesion-slip distributions shown in Fig. 4.24 are non-steady during the wheel-IRJ impact, and the proportion of contact patch occupied by the adhesion and slip regions vary greatly with the time step from t_8 onwards. The most significant variation occurs from t_9 to t_{13} . At instant t_9 , the adhesion region accounts for almost the entire contact patch. Next, the adhesion zone shrinks gradually and the slip region reaches its maximum occupation at instant t_{12} , when the bounce tendency of the wheel comes to an end and the wheel is nearly at the second impact, which corresponds to the contact force trough at approximately 47.7 ms in Fig. 4.18 (b). The good consistency between the adhesion-slip distributions calculated by the contact stresses and the micro-slips support the conclusion that the explicit FEM can solve the transient impact contact problem with non-linear material properties and arbitrary discontinuous contact geometries.

4.6 Wave phenomena

Compared with the contact force and stress, the surface nodal vibration velocity is found to be more sensitive to dynamic effects excited by wheel-rail contact (Yang *et al.*, 2016; Zhao & Li, 2016). The rail surface nodal velocity calculations in this study revealed wave phenomena excited by wheel-rail frictional rolling impact contact, and the results were based on the fine mesh of the FE model, small computational and output time steps, and full coupling of the contact and dynamics in the explicit integration. The size of the fine mesh is based on the requirement that the size of the elements should be no larger than half a wavelength. The small computational time step enables the calculations to capture high-frequency dynamic effects, and the small output time step facilitates the observation of the generation and propagation processes of the simulated waves. The full coupling means that the contact force and wheel-rail dynamics are updated simultaneously in every time step, thereby allowing the dynamic effects to be fully considered when calculating the contact solutions. Certain wave patterns that indicate wave generation, propagation and reflection were excited by wheel-rail contact produced in the solution zone, and they are presented and analysed in this section. More evident wave phenomena can be observed in the animations ("Animation for Fig. 4.25, <https://youtu.be/tWyWKw9XxRI> ; , " ; "Animation for Fig. 4.27, <https://youtu.be/fAg99j6kquI> ; [accessed 16.11.22] " ; "Animation for Fig. 4.28, <https://youtu.be/eHh24SnWDFQ> ; [accessed 16.11.22] ").

4.6.1 Wave generated by wheel-rail contact

The wave phenomenon discussed here was first observed before the wheel-IRJ impact. Fig. 4.25 (a) and (b) show the rail nodal velocities in the solution zone simulated by simulation 3 at instants 43.615 ms (output time step=115) and 43.640 ms (output time step=140), respectively. The colour depth in the figure indicates the magnitude of the normal nodal velocity, which can be used to identify the approximate position of the wheel-rail contact patch. The darker and lighter semi-ovals indicate the leading and trailing parts of the contact patch, respectively. The tangential nodal velocities are indicated by blue arrows. The arrows point in the direction of the tangential velocity and the arrow length is proportional to the magnitude. The stripe in the middle of each graph shows the position of the joint.

A regular wave pattern propagating from the wheel-rail contact area towards the joint can be observed in Fig. 4.25 (a). The wave with a wavelength of approximately 6 mm is stronger around the contact patch and dissipates when propagating. When the wavefront reaches the joint, a reflective wave occurs under the free boundary condition defined on the rail end at the

joint. The reflective wave extends from the joint back to the contact patch and interferes with the original wave as indicated in Fig. 4.25 (b). More obvious wave interference can be observed in the corresponding animation ("Animation for Fig. 4.25, <https://youtu.be/tWyWKw9XxRI> ; ,").

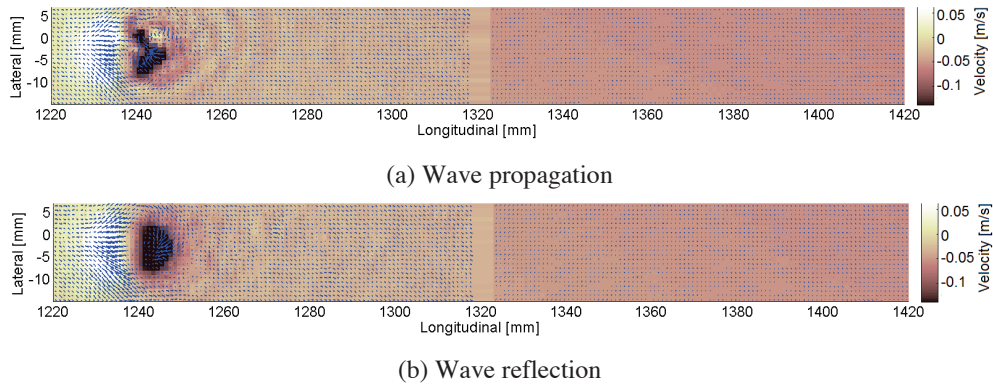


Figure. 4.25: Patterns of wave propagation and reflection produced by simulation 3

The wave phenomena discovered here are transient and normally take less than 0.1 ms from generation to disappearance. The generation process of the wave shown in Fig. 4.25 (a) is displayed with an output time step of $1 \mu\text{s}$ in Fig. 4.26. The instant of the first graph (T1) is 43.603 ms, which is 0.012 ms (12 output time steps) earlier than that of Fig. 4.25 (a). At T1, the rail surface nodal velocities appear to be distributed symmetrically with respect to the longitudinal centre line. The leading and trailing parts of the contact patch can be identified by the darker and lighter semi-ovals, respectively. The region ahead of the contact area is slightly darker than that behind the contact area. The tangential velocities are mainly concentrated on the trailing part of the contact patch, and their directions are largely consistent with the wheel rolling direction. The lateral components of the tangential velocities increase with the distance to the longitudinal centre line of the contact patch. At instant T2, perturbation of the nodal velocity suddenly occurs in the leading part of the contact patch. The perturbation spreads radially and consequently develops into a wave in the following instants. This perturbation is suspected to be related to the wheel-rail friction-induced instability and stick-slip rolling contact, which will be discussed in Chapter 7.

Graphs of instants T3 and T6 indicate that the wave patterns are embodied in both the normal and tangential nodal velocities, and the direction of the tangential velocities are consistent with the wave propagation direction. The wave is initiated at the longitudinal position of 1244 mm (T2), and within 3 time steps, its front reaches 1254 mm (T5). Neglecting the wheel rolling distance in such a short period (less than 0.1 mm), the wave speed is estimated as 3 km/s. Both the propagation form and the speed of the produced wave are consistent with the properties of Rayleigh waves (Telford *et al.*, 1990).

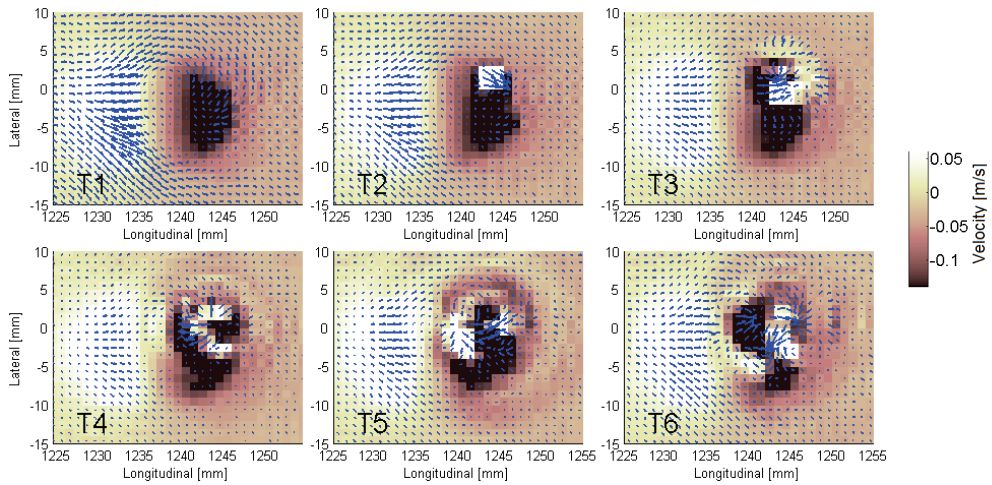
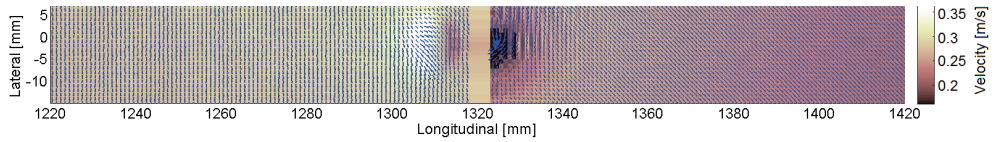


Figure. 4.26: Generation process of a wave

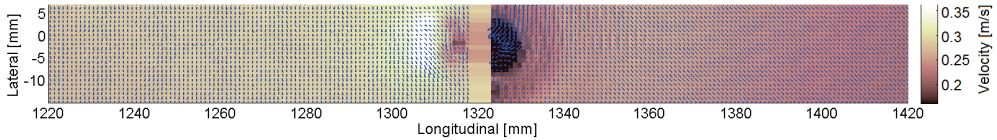
4.6.2 Wave excited by wheel-IRJ impact

The simulation of wheel-IRJ impact also revealed that an impact wave can be generated when the wheel rolls over the joint and just touches the rail on the other side. Fig. 4.27 displays an impact wave produced by simulation 3 at instants 46.390 ms (output time step=2890), 46.395 ms (output time step=2895) and 46.400 ms (output time step=2900). At these instants, the wheel was rolling from the left rail to the right rail, and it was in contact with both rail ends. As shown in Fig. 4.27, an obvious wave occurs and propagates on the rail after the joint. Compared with the wave patterns displayed in Fig. 4.25, the impact wave patterns displayed in Fig. 4.27 are mainly formed by the normal nodal velocities, and the wavelength is approximately 10 mm. The contributions of the tangential nodal velocities to the wave patterns are much less pronounced. More evident impact wave propagation can be seen in the animation ("Animation for Fig. 4.27, <https://youtu.be/fAg99j6kquI> ; [accessed 16.11.22] ").

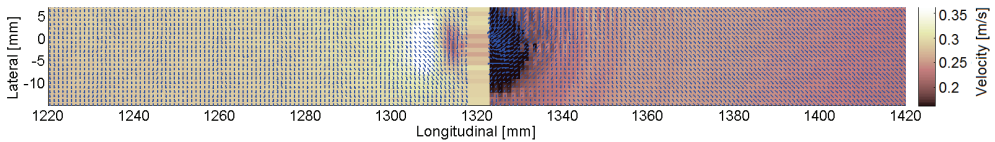
In addition to the wave types displayed in Fig. 4.25 and 4.27, simulations 1 and 2 also produced waves with longer wavelengths. Fig. 4.28 (a) and (b) show two examples produced by simulation 2 at instants 46.74 ms (output time step=3240) and 46.762 ms (output time step=3252), respectively. These two waves appear immediately after the whole contact patch is transferred to the rail after the joint, and their wavelengths, which are shown in Fig. 4.28 (a) and (b), are approximately 40 mm and 20 mm, respectively. The animation ("Animation for Fig. 4.28, <https://youtu.be/eHh24SnWDFQ> ; [accessed 16.11.22] ") shows a more clear depiction of these waves. The longer-wavelength wave was not observed in simulation 3. The cause of these longer-wavelength waves must be further studied.



(a) An impact wave at instant 46.390 ms

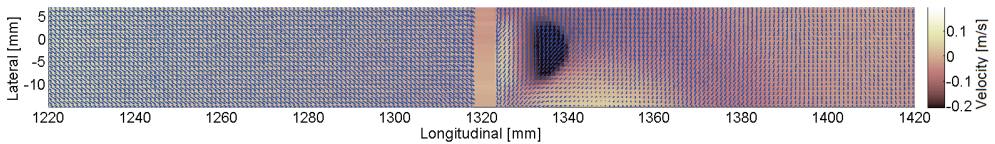


(b) An impact wave at instant 46.395 ms

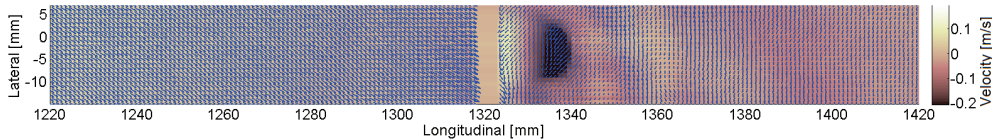


(c) An impact wave at instant 46.400 ms

Figure. 4.27: An impact wave pattern produced by simulation 3



(a) Wave with a wavelength of approximately 40 mm



(b) Wave with a wavelength of approximately 20 mm

Figure. 4.28: Wave patterns with longer wavelengths produced by simulation 2

4.7 Summary of the modelling of impact contact

This chapter investigated the transient contact solutions of wheel-IRJ frictional rolling impacts with dynamic effects simulated by an explicit FE wheel-IRJ dynamic interaction model, which was validated against a comprehensive field measurement including a hammer test and a pass-by measurement. The presented explicit FEM is proven to be sufficient and accurate for solving wheel-IRJ impact problems by fully coupling the high-frequency dynamics of wheel and rail continua with the complex transient impact contact in one simulation.

The transient solutions of impact contact with small time steps calculated in this study include the contact patch area, stress magnitude and direction, micro-slip distribution, and rail surface nodal velocity in the vicinity of a joint. The simulated contact solutions tended to vary noticeably with the time step, indicating that dynamic effects play important roles in the wheel-IRJ impact contact. Transient positive surface shear stress, whose direction is opposite that of shear stress under ordinary tractive rolling, was discovered on the rail surface immediately after the joint. The simulated transient adhesion-slip distributions determined by the contact stresses and micro-slip solutions were verified by each other.

The influence of the wheel-rail contact geometry on the transient contact solutions was also investigated in this study. The contact solutions calculated with the nominal geometry correspond well with those reported in the literature, whereas those simulated with the measured geometry show obviously non-steady-state impact effects. The good agreement between the simulated 'footprints' of the contact patch and the in situ running band implies that the model with the measured geometry provides more realistic predictions of the transient solutions of the impact contact at the target IRJ. Without considering the realistic contact geometries, the impact contact force and impact contact area fluctuations may be significantly underestimated.

In addition, regular wave patterns were produced both before and during the wheel-IRJ impacts in the simulations, and these patterns reflect continuum vibrations excited by wheel-rail frictional rolling and impact contact and confirm that the simulated transient contact solutions are reliable.

5

NUMERICAL EXAMPLE 2: SQUEAL-EXCITING FRICTIONAL ROLLING CONTACT

This chapter gives the second numerical example of modelling of wheel-rail dynamic interactions with the explicit finite element method (FEM) – simulating the squeal-exciting frictional rolling contact. Fig. 5.1 shows the schematic logic of this chapter. Section 5.1 first reviews two widely accepted generation mechanisms, i.e., falling-friction and mode-coupling, and also the modelling approaches of wheel unstable vibration and the consequent squeal. Section 5.2 presents an explicit finite element (FE) wheel-rail dynamic interaction model with wheel lateral motion. Section 5.3 then analyses the simulated contact forces (Subsection 5.3.1), the dynamic contact solutions (Subsection 5.3.2) and the wheel dynamic behaviour (Subsection 5.3.3). The analyses suggest that the explicit FE model may reproduce the falling-friction effect and the wheel mode-coupling behaviour and thus confirm that the explicit FEM is suitable for modelling squeal-exciting contact. The aim of this chapter is to contribute to better modelling and understanding of friction instability and squeal generation from the perspective of wheel-rail dynamic interaction.

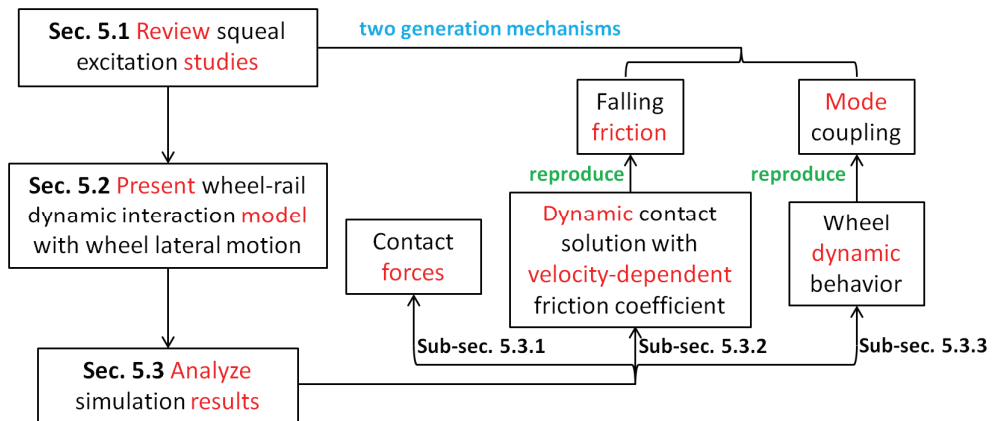


Figure 5.1: The schematic logic of Chapter 5

5.1. Introduction of the friction-induced squeal

Squeal noise can occur when a railway vehicle negotiates tight curves. Because the leading wheelset fails to align itself tangentially to the rail, large lateral creepage occurs at the contact between the tread of the inner wheel and the top surface of the low rail, and the flange of the outer wheel contacts the gauge corner of the high rail. During this process, two types of high-frequency curve squeal effects, which share certain features, can be induced: the tonal ‘wheel squeal’ (studied in this chapter) and the more broad-band ‘flange squeal’ (the flange contact will be discussed in Chapter 6).

Squeal, which is an intrinsically nonlinear and transient phenomenon, poses great challenges in modelling (Pieringer, 2014). Systematic studies on curve squeal noise began in the 1970s, when Rudd (1976) described the wheel-rail frictional characteristic (the functional dependence between friction force and wheel-rail relative velocity) in terms of ‘negative damping’ (generalised as full ‘stick-slip’) or ‘falling friction’ and associated this characteristic with the mechanism of wheel squeal. Since then, various increasingly sophisticated theoretical models have adopted parts of this mechanism based on Rudd’s seminal model (Remington,

1987; Fingberg, 1990; Périard, 1998; Heckl & Abrahams, 2000; de Beer *et al.*, 2003; Huang, 2007).

Analytical research (Graf & Ostermeyer, 2015), however, revealed that instability can also occur with constant or even positive creep force characteristics when additional mechanical degrees of freedom are considered. Similarly, FE analyses by the complex eigenvalue approach revealed that instability arises when two modes coalesce, or couple, in the presence of friction (Ouyang *et al.*, 2005). To consider the influence of vertical dynamics on friction, the ‘mode-coupling dynamic instability’ or the ‘sprag-slip’ mechanism have been employed in combination with falling-friction theories to predict friction-induced instability (Eadie *et al.*, 2005; Iwnicki, 2006; Huang, 2007; Anderson & Wheatley, 2008). Chiello *et al.* (2006) concluded that the two types of destabilization, i.e., that caused by the falling-friction mechanism and that caused by the mode-coupling mechanism, may be combined in each particular situation of squeal; thus, both should be explored. The generation of squeal is characterised as ‘enigmatic’ (Jiang *et al.*, 2015) or ‘erratic’ (Vincent *et al.*, 2006; Glocker *et al.*, 2009) in railway research, because field observations of squeal phenomena often fail to be explained by the existing theories.

The contact model accounting for the frictional instability of a vibrating wheel is considered the central part of the squeal prediction model (Zenzerovic *et al.*, 2016). This chapter presents an explicit FE wheel-rail dynamic interaction model to simulate wheel-rail squeal-exciting contact with unsteady lateral creepage. The dynamic wheel and rail interaction is considered to be directly related to squeal generation (Huang *et al.*, 2008); moreover, unsteady lateral creepage, particularly between the leading inner wheel and low rail, is thought to be the main cause of squeal (Thompson, 2009). Because the explicit FEM fully couples the calculation of wheel-rail frictional rolling contact with the calculation of wheel/rail structural dynamics (see Chapter 2), the proposed explicit FE model can accommodate the dynamic effects involved in wheel-rail interactions and is intrinsically suitable for modelling wheel-rail friction-induced unstable vibration and the resulting squeal.

5.2. Wheel-rail dynamic interaction model with wheel lateral motion

Fig. 5.2 (a) shows the employed three-dimensional explicit FE wheel-track dynamic interaction model with wheel lateral motion. A 10 m length of half-track and a half wheelset with sprung mass of the car body and the bogie were considered. The wheel, the rail and the sleepers were modelled using 8-node solid elements. To achieve high solution accuracy with a reasonable model size, non-uniform meshing was used. The mesh size around the initial position of the wheel-rail contact and the 150 mm length of the solution zone was 1 mm. The lumped mass of the car body and bogie were modelled as mass elements that were connected to the wheelset by the primary suspension of the vehicle with parallel linear springs and viscous dampers. Because the sleepers and ballast have little influence on the high-frequency dynamic behaviour under study, each sleeper model contained only 12 solid elements, and the ballast was simplified as vertical spring and damper elements with the displacement constrained in the lateral and longitudinal directions. The parameters involved in the track model are taken primarily from Table 4.1. The wheel-rail contact was defined with real geometry and with the wheel flange being included. The wheel geometry corresponded to a passenger car wheel of the Dutch railway with the standard profile of S1002; the rail was UIC54E1 with an inclination of 1:40. No geometry irregularities were considered on the surfaces of the wheel or rail.

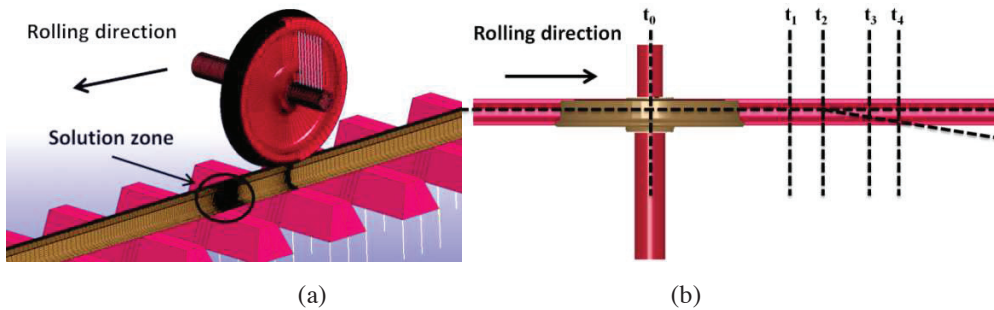


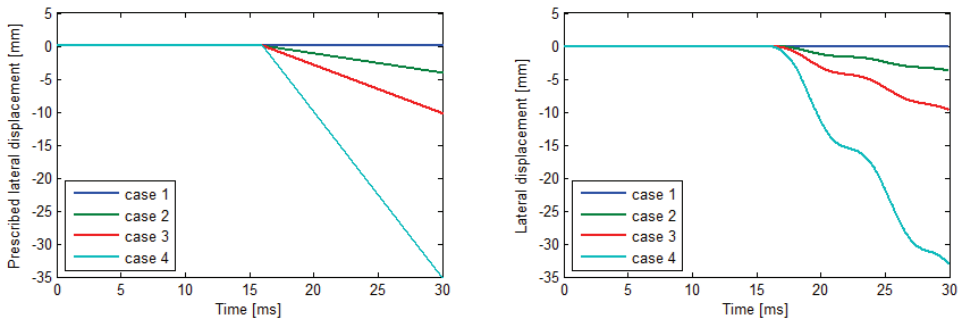
Figure 5.2: Wheel-rail interaction model

In the transient dynamic simulation, the wheel rolled from its initial position at time $t_0=0$ s to the solution zone with an initial speed of 100 km/h along the rail, as shown in Fig. 5.2 (b). The dynamics arising from the wheel/rail initial kinematic and potential energy due to imperfect static equilibrium (Zhao & Li, 2011) have relaxed at time $t_1=15$ ms. The wheel lateral motion was subsequently simulated from time $t_2=16$ ms by applying the prescribed displacement boundary conditions listed in Table 5.1 to both ends of the wheel half-axle, except for simulation case 1. Note that in this study, the angle of attack was approximated to zero because in the simulations, the initial angles of attack were zero and both ends of the wheel half-axle model applied the same displacement boundary condition during the transient rolling. Figs. 5.3 (a) and (b) present the prescribed displacement boundary conditions applied in the simulations and the resulting lateral wheel displacements, respectively. The two graphs share the same trend, but the simulated displacements fluctuated due to the flexibility of the wheel and axle; the unsteady lateral creepage was thus simulated. The wheel entered the solution zone at time $t_3=16.5$ ms and exited at $t_4=18.7$ ms. The dynamic evolution of the contact solutions was captured between t_3 and t_4 .

Table 5.1 Prescribed displacement boundary conditions applied to different simulation cases

Prescribed displacement boundary conditions	Simulation cases with a constant COF	Simulation case with a velocity-dependent COF
No lateral motion of wheel	Case 1	
Small lateral motion of wheel	Case 2	
Medium lateral motion of wheel	Case 3	Case 5
Large lateral motion of wheel	Case 4	

The wheel was driven by a cosine-functional driving torque (Eqn. (3.2)) applied on the wheel axle. The torque increased gradually before reaching its maximum value at 6 ms. A longitudinal creep force was thus generated and the traction coefficient was below the COF before the wheel entered the solution zone at time $t_3=16.5$ ms. The traction coefficient varies with time in dynamic rolling because of vibration, and its nominal value is approximately 0.27. A constant COF=0.45 was used for simulation cases 1~4. Knothe *et al.* (2001) reported that the falling-friction characteristic can be reproduced only by assuming that the COF depends on the wheel-rail sliding velocity; an additional simulation, i.e., case 5 listed in Table 5.1, was therefore conducted with a velocity-dependent COF. Simulation case 5 shared the same configuration as case 3 except for the COF. When a velocity-dependent COF is applied, the overall COF may differ from the local COF at a node (Zhao & Li, 2016).



(a) Prescribed displacement boundary conditions (b) Resulted wheel lateral displacements

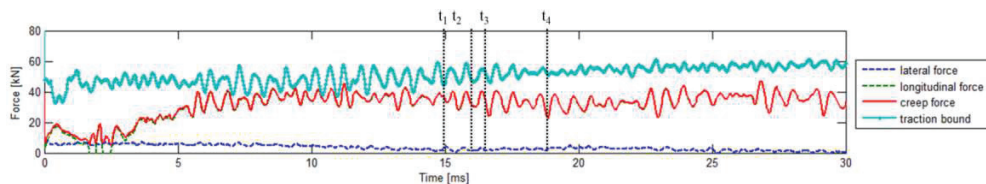
Figure. 5.3: Time histories of the prescribed displacement boundary conditions and the resulted wheel lateral displacements

5.3. Analyses of wheel-rail contact and dynamics results

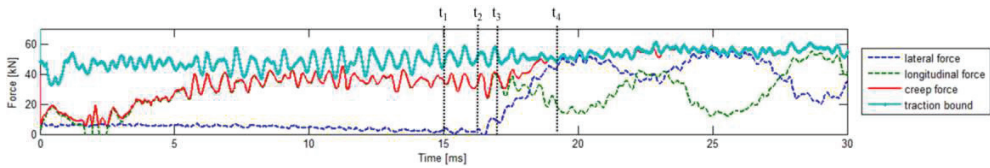
This section first analyses the contact forces calculated by the explicit FE model in Subsection 5.3.1 to provide a broad overview of the wheel-rail dynamic interaction with wheel lateral motion. To reproduce the two potential mechanisms of squeal introduced in Section 5.1, i.e., falling-friction and mode-coupling, the simulated wheel-rail dynamic contact solutions and structural dynamic responses are analysed in Subsections 5.3.2 and 5.3.3, respectively.

5.3.1 Contact forces

Figs. 5.4 (a) and (b) show the time histories of the contact forces simulated without wheel lateral motion (case 1) and with medium lateral motion (case 3), respectively. Before time $t_1=15$ ms, the simulated contact forces fluctuated mostly due to vibrations excited by initial kinetic and potential energy in the un-relaxed system. The traction bound (denoted by the cyan curve) fluctuated around the static value 50 kN. After the oscillations were damped to less than 10% of the static values at time t_1 , a quasi-steady state could be assumed to have entered into. The creep force is the resultant force of the lateral and longitudinal contact forces. In Fig. 5.4 (a), the simulated creep force (denoted by the red curve) almost overlaps the longitudinal force (denoted by the green curve) because the value of the lateral force (denoted by the blue curve) is small. By contrast, as shown in Fig. 5.4 (b), the lateral force simulated by case 3 jumped to large value after $t_2=16$ ms due to the enforcement of a prescribed displacement boundary condition; consequently, the creep force reached the traction bound, and friction saturation occurred at approximately 19 ms. The dynamic evolution of the contact solution between times $t_3=16.5$ ms and $t_4=18.7$ ms were output and are analysed in the next subsection.



(a) Contact forces simulated by case 1



(b) Contact forces simulated by case 3

Figure. 5.4: Time histories of the simulated contact forces

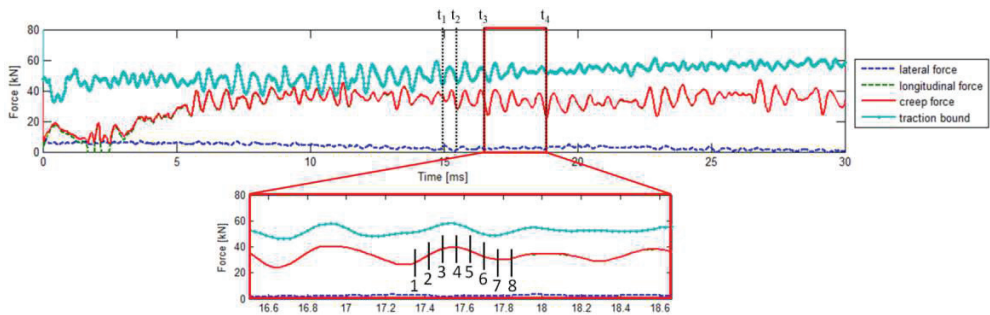
5.3.2 Contact solutions

This subsection analyses the dynamic contact solutions calculated using the proposed explicit FE wheel-rail interaction model, including contact stresses and the distributions of micro-slip and adhesion-slip regions within the contact patch. This subsection also discusses the influences of lateral creepage and velocity-dependent COF on the dynamic contact solutions.

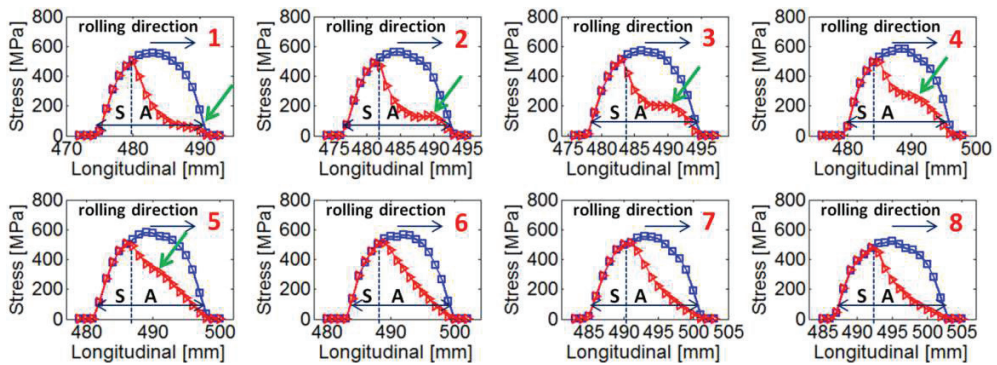
5.3.2.1 Contact solutions with dynamic effects

Fig. 5.5 (a) shows a magnified view of the time histories of the contact forces calculated by case 1 between times $t_3=16.5$ and $t_4=18.7$ ms (within the solution zone). The close-up view shows that the simulated traction bound and creep force oscillated periodically but were not exactly in phase. Eight time points with a fixed interval (0.06 ms) were selected from a certain period of the creep force fluctuation, designated 1~8 in the magnified view in Fig. 5.5 (a). Fig. 5.5 (b) plots the distributions of the simulated surface shear stress (red curve) and traction bound (blue curve) within the contact patch at these eight selected time points. The adhesion and slip regions determined by the contact stress are denoted 'A' and 'S' in the figure, respectively. A comparison of the stress distributions calculated at the eight time points in Fig. 5.5 (b) indicates that the surface shear stress within the adhesion region increased gradually from the first time point to the 4th time point and decreased from the 5th time point to the 8th time point. This trend is in accordance with the variation in the creep force shown in the magnified view of Fig. 5.5 (a). The animation displaying the variation in the surface stress with time ("Animation for Fig. 5.5, <https://youtu.be/3jeei3NTP84>,") indicates that the surface shear stress and the traction bound varied periodically with the contact forces. As reported by Ouyang *et al.* (2005), the interface pressure distribution varies with time during vibration; thus, the periodic variation in the surface normal and shear stresses reproduced in this numerical example may reflect the dynamic effects involved in the explicit FE contact solutions.

In addition, a moving local peak of the shear stress, indicated by the green arrows in Fig. 5.5 (b), was observed within the adhesion region in the variation process of the contact stress. The peak starts at the leading edge of the contact patch, moves towards the trailing part, and ultimately exits the adhesion region at the juncture of the adhesion-slip regions. Because the shear stress is close to the traction bound when close to the leading edge of the contact patch and when close to the juncture of the adhesion-slip regions, sudden friction saturation, or a perturbation of micro-slip, may arise when such a local peak of shear stress appears or exits the adhesion region. This will be illustrated in more detail in Section 7.1.3.



(a) Magnified view (within the solution zone) of the time histories of the contact forces for simulation case 1



(b) Stress distributions calculated at corresponding time points denoted by 1~8 in (a) (blue curve: traction bound; red curve: surface shear stress; A: adhesion region; and S: slip region)

Figure. 5.5: Periodical surface stress distribution for simulation case 1

5.3.2.2 Contact solutions with lateral creepage

Contact stress and micro-slip are symmetrically distributed with respect to the longitudinal axis within the contact patch when creepage exists only in the longitudinal direction. When simulating wheel lateral motion in this study, the resulting wheel-rail lateral creepage caused asymmetric distributions of contact stress and micro-slip within the contact patch, as shown in Fig. 5.6. To compare contact solutions with a broad range of lateral creepage, Fig. 5.6 plots six typical contact solutions obtained with different simulation cases: (a) and (b) were obtained with simulation case 1 at 17.58 ms and case 2 at 17.58 ms, respectively; (c) and (e) were obtained with case 3 at 17.58 ms and 18.54 ms, respectively; and (d) and (f) were obtained with case 4 at 17.07 ms and 17.94 ms, respectively. From top to bottom, the graphs in Fig. 5.6 display the simulated stress distributions along the longitudinal centre line of the contact patch (first row), stress distributions (second row) and micro-slip distributions (third row) within the contact patch, and shear stress and adhesion-slip region distributions obtained with Kalker’s boundary element method program CONTACT (Kalker, 1990) (fourth row). The corresponding creepage values (lateral creepage η and longitudinal creepage ξ) are presented in the captions below the graphs (except for Fig. 5.6 (f)).

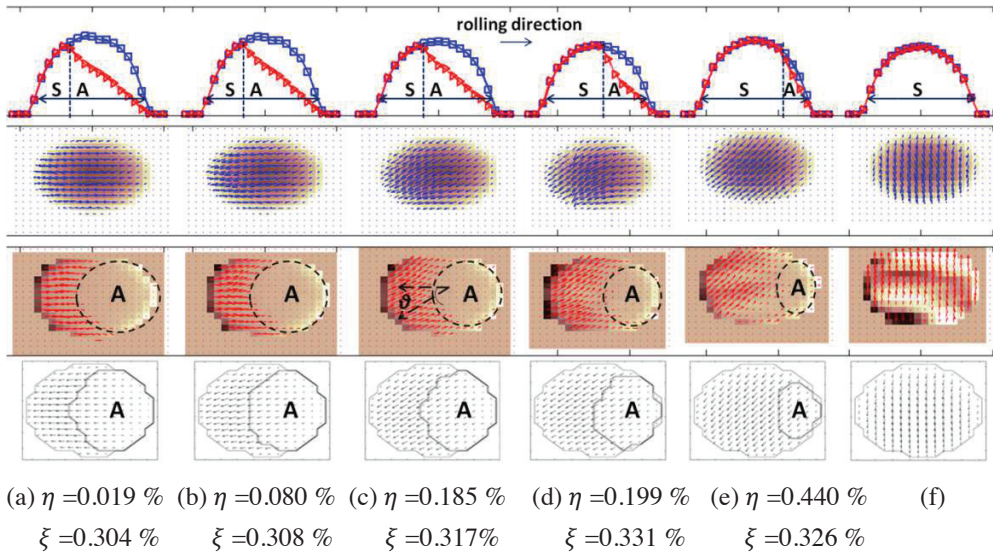


Figure 5.6: Simulated contact solutions with lateral creepage (first row: stress distributions along the longitudinal center line; second row: stress distributions within the contact patch; third row: micro-slip distributions within the contact patch; and fourth row: shear stress and adhesion-slip region distributions calculated with Kalker's CONTACT (Kalker, 1990). η and ξ are lateral and longitudinal creepage, respectively.)

Table 5.2 Input forces in the simulations with CONTACT

Graph Numbers in Fig. 5.6 Corresponding forces	(a)	(b)	(c)	(d)	(e)	(f)
Normal load F_n (kN)	126.68	125.61	123.87	102.60	116.19	106.46
Lateral creep force F_{ly} (kN)	2.19	9.30	20.27	18.41	36.83	47.04
Longitudinal creep force F_{lx} (kN)	39.46	39.19	38.12	33.59	34.01	6.09

The velocities of material particles vary with their locations due to vibration in a flexible finite element contact body (wheel or rail), as happens in reality. The creepage should thus be calculated with the velocities of the parts of the wheel and rail encompassing a certain number of elements at the contact, rather than with the velocities of the whole wheel and rail, as has been done so far in the literature. However, this study found that the size and location of the contact parts considered for the calculations of creepage may significantly influence the calculation results and cannot be easily determined. Considering that the explicit FEM and CONTACT should provide similar creepage-creep force relations, as reported in (Vo *et al.*, 2014), this study estimated the corresponding creepage values of the explicit FE contact solutions using CONTACT: the creep forces calculated with the explicit FE model (see Table 5.2) were input into the simulations with CONTACT as the prescribed tangential forces, and

the other input parameters used in the CONTACT simulations were the same as those involved in the explicit FE simulations. Contact solutions and the creepage values were then obtained with CONTACT and presented in the fourth row of Fig. 5.6. Note that no creepage value was presented below Fig. 5.6 (f); that is because when friction saturation occurs, a prescribed creep force corresponds to non-unique creepage.

In the contour/vector diagrams showing the stress distributions (second row), the pressure magnitude corresponds to the depth of the colour; the blue arrows indicate the direction of the shear stress, and their lengths are proportional to the shear stress magnitude. Similarly, in the contour/vector diagrams showing the micro-slip distributions (third row), the depth of the colour within the contact patch indicates the magnitude of the normal wheel-rail relative velocity; the red arrows indicate the directions of the micro-slip, and their lengths are proportional to the micro-slip magnitude. The asymmetry of the distribution of the contact patch can be characterised by an orientation angle θ , as shown in 5.6 (c). The orientation angle increases with the lateral creepage from Fig. 5.6 (a) to (f). For the solutions calculated with CONTACT (fourth row), the black arrows indicate the direction of the shear stress, and their lengths are proportional to the shear stress magnitude. The orientation angles obtained with CONTACT are consistent with those obtained with the explicit FEM.

The distributions of the adhesion-slip regions determined by the simulated explicit FE contact stresses in the first row and micro-slips in the third row are in line with each other. They are also in reasonable agreement with the distributions of adhesion-slip regions determined by CONTACT in the fourth row. In the graphs of the micro-slip distribution (third row), the slip regions covered with micro-slip vectors are located at the trailing part of the contact patch, while the adhesion regions 'A' indicated by dashed ovals shrink with increasing lateral creepage from Fig. 5.6 (a) to (e). Fig. 5.6 (f) shows friction saturation.

The colour depth outside the contact patch corresponds to a zero normal relative velocity in the graphs of the micro-slip distribution (third row). Thus, the colour depths at the leading and trailing edges are lighter and darker, respectively, indicating a positive and negative normal relative velocity. Wave phenomena indicated by the variation in colour depth can be observed in the micro-slip distributions calculated with the explicit FEM in Figs. 5.6 (e) and (f). Because the surface elements of the wheel and rail were in contact, further movement towards or away from each other caused transient intensification or relaxation of the contact, respectively (see also Section 6.3.5.3). The waves were therefore essentially embodied in the alternation of compression intensification and relaxation. The generation mechanism and property of the wave will be discussed in Chapter 7.

5.3.2.3 Contact solutions with a velocity-dependent COF

A velocity-dependent COF defined in Eqn. (2.29a) was adopted in the simulation case 5. The decay coefficient c , static COF μ_s and dynamic COF μ_d were set to 6, 0.5 and 0.32, respectively, as those used in (Zhao & Li, 2016). Fig. 5.7 presents one example of the contact solutions calculated with the simulation case 5 at 16.68 ms. Although simulation case 5 shared the same configuration as case 3 except for the COF, the orientation angle shown in Fig. 5.7 (b) is much smaller than those shown in Figs. 5.6 (c) and (e). That is because the lateral creep force increased when the wheel passed the solution zone (see the blue curve between time t_3 and t_4 in Fig. 5.4 (b)), and the contact solution presented in Fig. 5.7 was calculated at an earlier time step than those of Figs. 5.6 (c) and (e) and thus had a smaller lateral creepage.

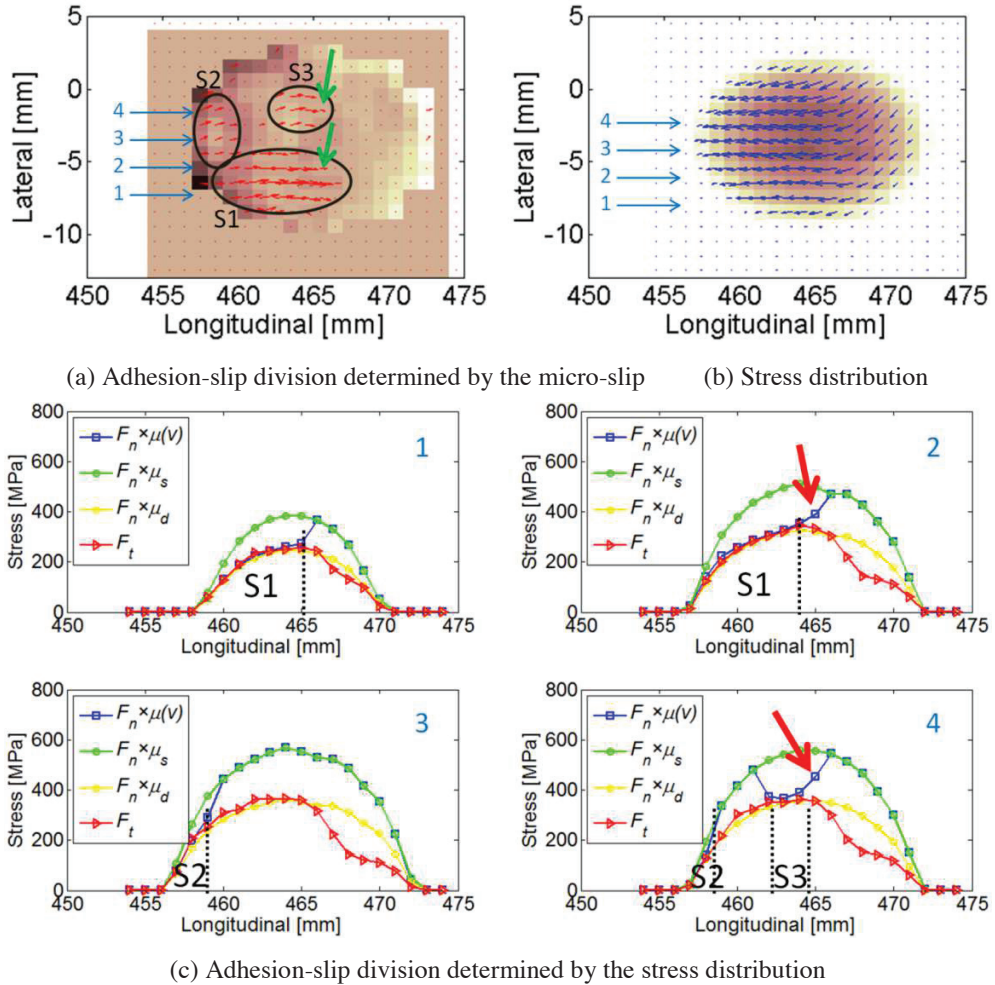


Figure. 5.7: One example of the contact solutions calculated using a velocity-dependent COF (simulation case 5)

Fig. 5.7 (a) shows the simulated micro-slip distribution within the contact patch. Compared to the adhesion-slip distributions simulated with a constant COF shown in Fig. 5.6, the adhesion-slip distribution in Fig. 5.7 shows a less regular pattern: the slip regions denoted by the black ovals S1, S2 and S3 scatter in the trailing part of the contact patch. However, this result is believed to be a more realistic contact condition (Zhao & Li, 2016).

The contact pressures and surface shear stresses plotted in Fig. 5.7 (c) were extracted from the stress distribution shown in Fig. 5.7 (b) along the four longitudinal lines of contact patches indicated by blue arrows. In Fig. 5.7 (c), the red and blue curves indicate the simulated surface shear stresses F_t and the traction bound (the product of the contact pressure F_n and the velocity-dependent COF $\mu(v)$), respectively; the green curve indicates the product of the

contact pressure and the static COF μ_s ; and the yellow curve indicates the product of the contact pressure and the dynamic COF μ_d .

According to Coulomb law for statics, the blue curve in Fig. 5.7 (c) should coincide either with the green curve for adhesion regions or with the red curve for slip regions. Discrepancies were, however, observed in the numerical solutions at two data points, as indicated by the two red arrows: the blue curves at these two data points should have overlapped with the red curves because the calculated micro-slips at these locations are nonzero in Fig. 5.7 (a), as indicated by the two green arrows. These discrepancies may stem from two aspects. First, the shear stress and traction bound shown in Fig. 5.7 (c) were obtained at different time steps. Because the velocity-dependent COF $\mu(\dot{\mathbf{u}}_{rel})$ used to calculate the traction bound (Eqn. (2.28c)) and tangential force (Eqn. (2.28d)) at a certain time step relies on the nodal displacements obtained at the previous time step (see Eqns. (2.28) and (2.29) and Table 2.1), the traction bound displayed in Fig. 5.7 (c) was in fact calculated one time step later than the shear stress. Considering that the time step used in the simulation was small (approximately 86 ns), the second aspect is expected to dominate: the discrepancies were due to the different sensitivities of the approaches used to determine the slip region. The micro-slip shown in Fig. 5.7 (a) and the velocity-dependent COF $\mu(v)$ used for Fig. 5.7 were calculated using the wheel-rail relative velocities, whereas the shear stress F_t was obtained using the relative displacement (Eqn. (2.28a)). Because the displacement was obtained by integrating the velocity (Eqn. (2.12b)) and the integration can act as a filter, the traction bound shown in Fig. 5.7 (c) is expected to reflect dynamic effects more sensitively than the surface shear stress calculated using the displacement.

The adhesion-slip distribution determined using the calculated contact stresses in Fig. 5.7 (c) is in reasonable agreement with that determined using the calculated micro-slip in Fig. 5.7 (a), indicating that the explicit FEM can predict wheel-rail dynamic contact solutions with velocity-dependent COFs. Because the falling-friction characteristic can be reproduced only by the velocity-dependent COF (Knothe *et al.*, 2001), the explicit FEM is expected to be capable of reproducing the falling-friction characteristic.

5.3.3 Wheel dynamic behaviour

Based on the analysis of the simulated wheel-rail dynamic contact solution with velocity-dependent COF, the preceding subsection indicated that the explicit FEM is capable of addressing the falling-friction generation mechanism of wheel squeal. As illustrated in Sec. 2.2.3, an explicit FE model may include in its solution all the relevant vibration modes and associated wave propagations as long as the elements and time steps are sufficiently small. The computational time step (Δt in Eqn. (2.12)) of the transient analyses in this study fluctuated around 86 ns; thus, the vibration frequency up to 5.8 MHz can theoretically be predicted. This subsection analyses the wheel dynamic behaviour and compares the wheel dynamic responses simulated with and without lateral motion to address the other generation mechanism of squeal, namely, mode-coupling.

5.3.3.1 Validation of wheel dynamic behaviour

Wheel dynamic behaviour plays a more important role in the generation of high-frequency squeal noise than track dynamic behaviour (Thompson, 2009). Each tonal frequency of squeal is expected to relate to a wheel mode (Vincent *et al.*, 2006; Squicciarini *et al.*, 2015). To accurately simulate wheel dynamic responses during rolling, this study first validated the dynamic behaviour of the explicit FE wheel sub-model with a laboratory hammer test. The

wheel dynamic behaviour can be characterised by the modes and the corresponding natural frequencies (see Section 4.3.5). A typical NS-intercity wheel used in the Dutch railway was measured. Fig. 5.8 compares the wheel vibration modes measured by the hammer test and those identified through the FE modal analysis within the frequency range of squeal (up to 10 kHz), and reasonable agreement was reached. All these physical modes were thus included in the transient dynamic simulation by virtue of the full FE model and the small time step (Zhao & Li, 2011).

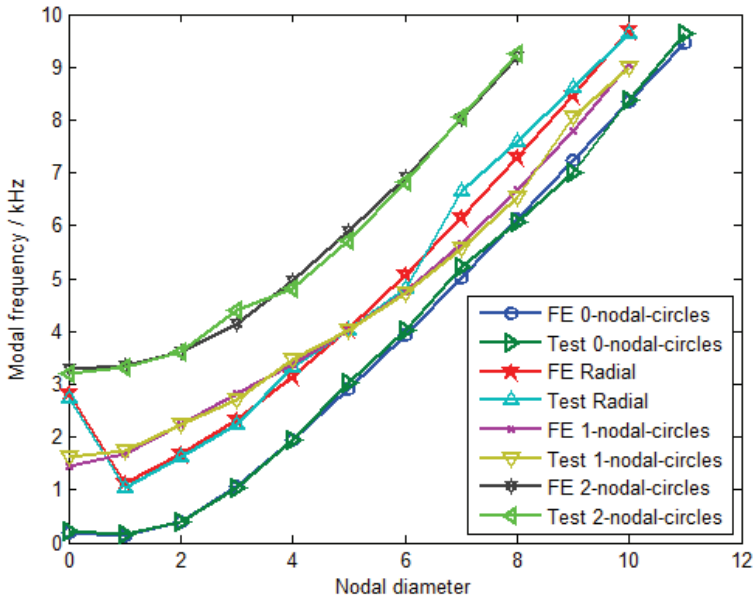
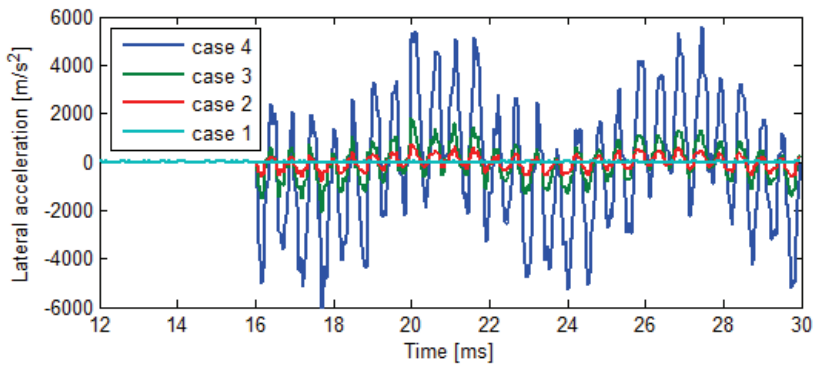


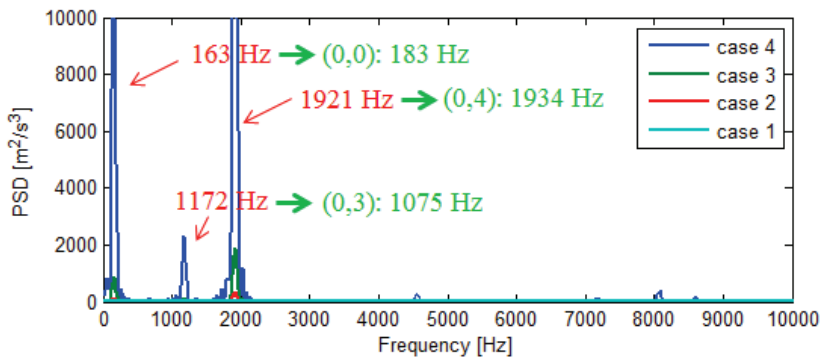
Figure 5.8: Comparison of the calculated and measured wheel modal frequencies

5.3.3.2 Squeal-like wheel vibration

After the validation of wheel dynamic behaviour, wheel dynamic responses were simulated using the proposed explicit FE wheel-rail dynamic interaction model. Figs. 5.9 (a) and (b) show the time histories and the corresponding power spectrum densities (PSDs), respectively, of the lateral vibration of the rolling wheel calculated in simulation cases 1~4. The squeal-like vibration signals represented by large amplitude limit-cycles were produced by the explicit FE model when applying the wheel lateral motion. The amplitudes of the limit-cycles of the time histories increased with increasing amplitude of the lateral motion applied to the wheel model. The three dominant frequencies of the squeal-like vibration signals shown in PSDs in Fig. 5.9 (b) are 163 Hz, 1172 Hz and 1921 Hz. Comparing these frequencies to the wheel modal frequencies identified in Subsection 3.3.1, the wheel modes excited in the simulations of wheel-rail dynamic interaction with wheel lateral motion can be determined: the mode with zero nodal circle and zero nodal diameter (0,0), the mode with zero nodal circle and three nodal diameters (0,3), and the mode with zero nodal circle and four nodal diameters (0,4), as shown in Fig. 5.9 (b) and Table 5.3. The results correspond well to the conclusion that zero-nodal-circle modes tend to be excited in squeal (Thompson, 2009).



(a) Time histories



(b) PSDs

Figure. 5.9: Time histories and PSDs of the simulated wheel lateral vibration during rolling

Table 5.3: Corresponding dominate frequencies of the simulated vibrations and wheel modes

Dominant frequency in PSDs	Corresponding modal frequency	Corresponding mode
163 Hz	183 Hz	0 nodal circle, 0 nodal diameter
1172 Hz	1075 Hz	0 nodal circle, 3 nodal diameters
1921 Hz	1934 Hz	0 nodal circle, 4 nodal diameters

5.3.3.3 Mode-coupling behaviour

Fig. 5.10 compares the wheel vibrations calculated with no lateral motion (case 1) and with large lateral motion (case 4). The comparison of the simulated wheel lateral vibrations in Figs. 5.10 (a) and (d) indicates that the enforcement of the lateral displacement boundary condition at time $t_2=16$ ms excited the out-of-plane axial modes (0,0), (0,3) and (0,4), as denoted in Fig. 5.10 (d). The comparisons of the simulated wheel vertical and longitudinal vibrations in Figs. 5.10 (b) and (e) and in Figs. 5.10 (c) and (f) indicate that the prescribed wheel motion in the axle direction may also excite the in-plane radial wheel modes with one nodal diameter and two nodal diameters, which are denoted by Radial 1 and Radial 2 in Figs. 5.10 (e) and (f), respectively. The coupling of the axial and radial dynamics shown in Fig. 5.10 suggests that

the mode-coupling mechanism can be reproduced by the proposed explicit FE wheel-rail dynamic interaction model.

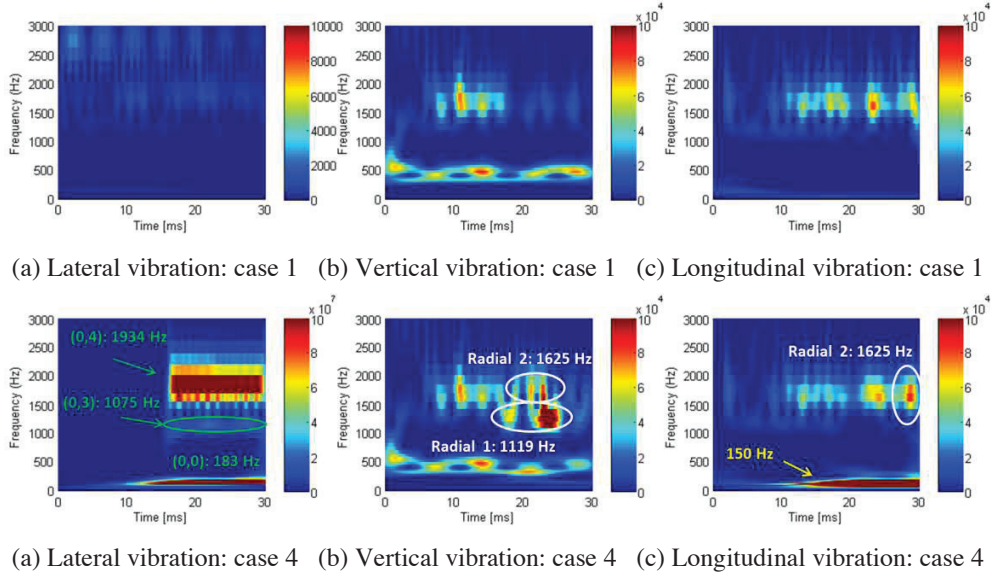


Figure. 5.10: WPSs of the simulated wheel vibration

The dominant frequency component of approximately 150 Hz in Fig. 5.10 (f) was excited mainly by the longitudinal creep force, which generally fluctuated in antiphase with the lateral creep force after time t_3 (see Fig. 5.4 (b)). The dominant frequency of the creep force fluctuations can be estimated by Fig. 5.4 (b) as approximately 150 Hz. However, because the axial wheel mode ((0,0): 103 Hz) with a close modal frequency was excited, the energy amplitude of the calculated wheel lateral vibration concentrated at approximately 150 Hz was much larger than that of the longitudinal vibration, as indicated by the colour bars of Figs. 5.10 (d) and (f).

5.4. Summary of the modelling of squeal-exciting frictional rolling contact

As the second numerical example of the modelling of wheel-rail dynamic interactions, this chapter has proposed an explicit FE wheel-rail dynamic interaction model with wheel lateral motion to simulate the squeal-exciting frictional rolling contact. The two commonly considered mechanisms leading to noise, namely, falling-friction and mode-coupling, were rigorously considered in the explicit FE model. The simulation results indicated that the proposed model can reproduce both mechanisms, thus confirming that the explicit FEM is reliable for predicting wheel-rail squeal-exciting contact and is promising for the accurate prediction of squeal.

This chapter analysed the dynamic contact solutions calculated by the explicit FE wheel-rail interaction model, including contact stresses and the distributions of micro-slip and adhesion-slip regions within the contact patch. The contact solutions obtained with the explicit FE are in agreement with those obtained with Kalker's boundary element program CONTACT.

The influences of the wheel lateral motion and the velocity-dependent COF on the dynamic contact solutions were also discussed.

Wave phenomena caused by large lateral creepage were observed in the analysis of the distribution of micro-slip. A moving local peak of shear stress was discovered within the adhesion region in the variation of contact stress, which was concluded to relate to the generation of perturbation-induced wave discussed in Chapter 7.

Applying the velocity-dependent COF resulted in a less regular adhesion-slip distribution pattern, which may show a more realistic contact condition. The distributions of the adhesion-slip regions determined by the simulated contact stresses and micro-slips with the contact COF were mutually consistent, whereas small discrepancies were observed when the velocity-dependent COF was used. The discrepancies were concluded to stem from the different sensitivities of the approaches used to determine the slip region.

The dynamic behaviour of the FE wheel model was validated through a laboratory hammer test. By relating the dominant frequencies of the simulated squeal-like vibration to the identified wheel modal frequencies, three zero-nodal-circle modes prone to be excited in squeal were determined and found to correspond well to previously reported results.

6

NUMERICAL EXAMPLE 3: CONTACT TRANSITION FROM SINGLE-POINT TO TWO-POINT

This section gives the third numerical example of wheel-rail dynamic interaction modelling – simulating the non-steady-state transition of wheel-rail rolling from single-point to two-point contact. Section 6.1 reviews studies on wheel-rail two-point contact. Section 6.2 presents a 3D explicit FE wheel-track dynamic interaction model for the simulation of contact transition. Section 6.3 carefully examines the calculated evolution of the wheel-rail contact position, stress magnitude and direction, adhesion-slip distribution, and wheel-rail relative velocities in the two contact patches to investigate the transient dynamic effects during the contact transition.

6.1. Introduction of the wheel-rail two-point contact

Complex two-point contact is difficult to model, as it involves arbitrary wheel and rail geometries, large creepage and spin. Traditional approaches based on the half-space assumption, such as Hertz's analytical method, virtual-penetration-based methods (Ayasse & Chollet, 2006; Piotrowski & Kik, 2008), and Kalker's program FASTSIM and CONTACT (Kalker & Johnson, 1993), are considered inaccurate because the radii of curvature of the contact bodies at the flange-gauge corner contact can be of the same size as the contact patch and the patch may be non-planar. ANALYN (Sh. Sichani *et al.*, 2014) and FaStrip (Sh. Sichani *et al.*, 2016), though also limited to the half-space assumption, were proposed as alternatives to the virtual-penetration-based methods and FASTSIM, with higher accuracies in terms of both creep force estimation and shear stress distribution, especially when the contact patch is non-elliptic. By extending the CONTACT to include quasi-quarter-spaces, Li (2002) presented the program WEAR to cope with conformal contact, including two-point contact. Its application to contact between a wheel and the switch blade of a turnout is presented in (Burgelman *et al.*, 2014).

As CONTACT and WEAR are based on the boundary element method (Li, 2002), they can only treat linear-elastic materials and idealised contact geometry, limiting their accuracy in analyses of wear and rolling contact fatigue (RCF) with large plastic deformation and arbitrary contact geometry. The use of the finite element method (FEM) was proposed to overcome these problems. The elastic half-space contact solutions calculated by the FEM correspond well with those obtained from Hertz contact theory (Yan & Fischer, 2000). The FEM was also proven to be applicable to two-point wheel-rail contact, as satisfying solutions have been obtained for contact points on the rail top and gauge corner (Telliskivi & Olofsson, 2004; Ringsber & Josefson, 2005; Sladkowski & Sitarz, 2005; Magheri *et al.*, 2011). A good integration between 3D FEM and multibody modelling is archived in (Meli *et al.*, 2011) to have a full description of vehicle dynamics.

The models in (Yan & Fischer, 2000; Telliskivi & Olofsson, 2004; Ringsber & Josefson, 2005; Sladkowski & Sitarz, 2005; Magheri *et al.*, 2011; Meli *et al.*, 2011) all assumed quasi-static state contact between the discretised wheel and rail models. However, dynamic effects may play significant roles under certain circumstances, such as impact contact at geometric irregularities of the wheel and rail surfaces. To consider such dynamic effects, the explicit FEM was adopted to simulate the fatigue and wear of the rail joint (Wen *et al.*, 2005), the growth of squat (Li *et al.*, 2008) and damage to the crossing nose (Wiest *et al.*, 2008a; Pletz *et al.*, 2012b). The transient elastic-plastic stress-strain states in the contact were calculated by employing elastoplastic materials in the models. By accounting for the normal load and creep force as well as a realistic contact geometry, the transient explicit FEM has been proven to be effective and accurate for solving single-point frictional rolling contact between the wheel

tread and rail with small (Zhao & Li, 2011) or large spin (Deng *et al.*, 2015) by comparing its quasi-static state solutions with those of Hertz and CONTACT. In comparison with the implicit FEM, the explicit integration scheme avoids the regularization of the friction law (Wriggers, 2006) required to treat the no-slip condition in the adhesion area and the convergence difficulties caused by the demanding contact conditions (Mulvihill *et al.*, 2011). Moreover, the computation efficiency is considerably improved when considering high-frequency vibrations.

In addition to impact, dynamic effects may also need to be considered when unstable vibration of the wheel (e.g., during curve negotiation) is present. In such a situation, increased wear, RCF and corrugation are expected (Chen *et al.*, 2010), and a squeal noise may occur (Thompson, 2009). The occurrence of unstable wheel vibration can be significantly influenced by the transition from single-point to two-point contact during wheel curving through curved tracks.

The explicit FEM has been applied to the analysis of wear and RCF in wheel curving with two-point contact (Vo *et al.*, 2015). The effects of the angle of attack (AoA) were considered, and the contact positions with certain AoAs and wheel/rail profiles could be determined. Another application of the explicit FEM to two-point contact was presented in (Chongyi *et al.*, 2010) to simulate the wear process on a laboratory twin-disc rig; good agreement was achieved by comparing the simulation results with the experimental results. However, in both cases, no dynamic effects were considered in the simulations, as the wheel motion was considered to be in the steady state and no unstable vibration occurred.

The chapter studies the transition from single-point to two-point rolling contact by employing the explicit FEM. The transition is a non-steady-state process and occurs in a short period of time. The appearance of the second contact point may cause sudden changes in the normal and tangential forces at the two contact patches, exciting waves and friction-induced unstable vibrations. First, an explicit FE model is presented to reproduce such a transient dynamic process numerically. Then, the contact solutions are carefully examined in terms of the evolution of the contact position, the stress magnitude and direction, the adhesion-slip distribution, and the wheel-rail relative velocities in the two contact patches. The analyses show that waves are indeed excited in the contact patches when two-point contact occurs. The ability to analyse the generation and propagation of the waves in rolling contact will enable a better understanding of dynamic rolling and its resulting wear (including fretting (Wei *et al.*, 2016)) and RCF and may provide a basis for the study of the ‘elusive’ short-pitch corrugation and ‘erratic’ squeal noise, both of which are consequences of dynamic frictional contact.

6.2. Wheel-rail dynamic interaction model with contact transition

The 3D explicit FE wheel-rail dynamic interaction model presented in Chapter 5 (see Fig. 5.2 (a)) was developed in this chapter to simulate non-steady-state transition from single-point to two-point contact by applying different boundary conditions to the wheel in the manner shown in Fig. 6.1 (a). The lateral displacement was constrained at the inner side of the wheel half-axle, and the outer end of the axle was free. In the transient dynamic simulation, the wheel rolled from its initial position to the solution zone with an initial speed of 80 km/h along the X direction, forming an AoA with respect to the rail longitudinal direction. It was driven by a torque applied on the axle, thus generating a longitudinal creep force between the wheel

and rail, which satisfies the requirement that the traction coefficient be below the friction coefficient. The friction coefficient was set to 0.6 to represent dry friction.

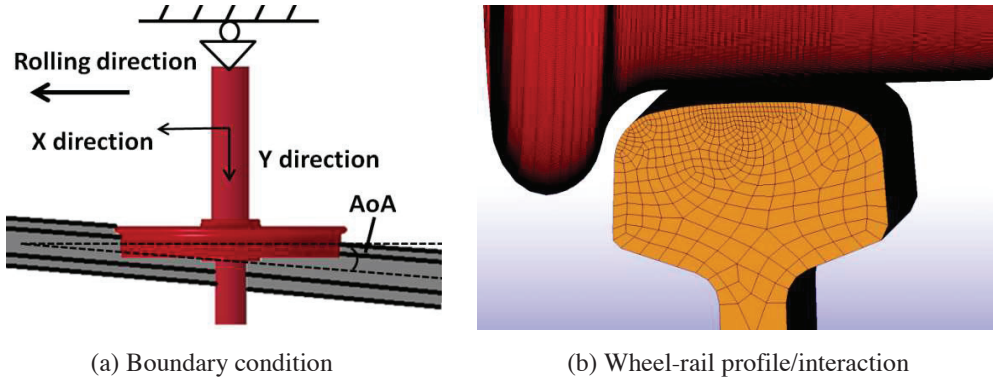


Figure. 6.1: Wheel-rail interaction model

The wheel-rail contact was defined with real geometry, including the wheel flange and rail gauge corner, as shown in Fig. 6.1 (b), enabling the creepage and spin motion caused by the flange rubbing to be fully considered. The wheel rolled with single-point contact between the wheel tread and rail crown before entering the solution zone. The damping in the system dissipated the initial kinetic and potential energy originating from any initial in-equilibrium of the system such that the system reached a quasi-steady state upon arriving at the solution zone. Starting from this state, the wheel-rail rolling entered into the transition from single-point to two-point contact. This transient evolution was captured and analysed in the solution zone.

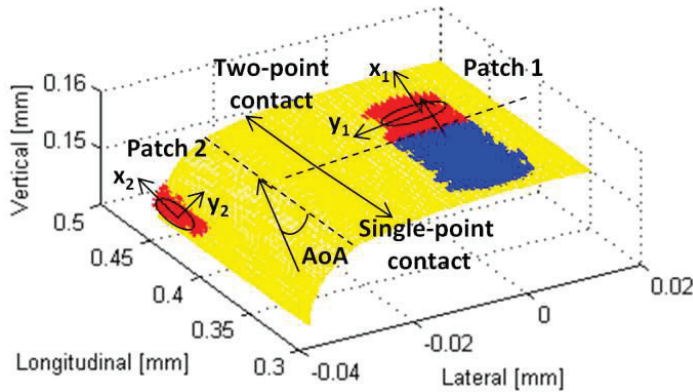
The integration was performed in the time domain with an explicit central difference scheme (see Section 2.2.1). A small time step (86 ns) was employed for the model to meet the Courant stability condition (Courant *et al.*, 1967). This, together with the detailed modelling of the structure and continuum of the wheel/track system, guaranteed that high-frequency dynamic effects up to 10 kHz were reproduced. It is commonly believed that the dynamic effects during wheel curving are mainly generated by the vibration of the wheel (Thompson, 2009). The dynamic behaviour of the FE wheel model has been validated in Section 5.3.3.1.

6.3. Solution of the contact model

To study the dynamic transition from single-point to two-point contact, the contact positions between the wheel and rail must be identified first. Then, the time histories of the normal and tangential contact forces of the two contact points were calculated to present a load transmission during the contact transition. The emphasis of the contact solution was on the evolution of the distributions of the pressure, surface shear stress, adhesion-slip region and wheel-rail relative velocities in the contact patch. The solutions of 9 continuous time steps, 5 before and 4 during the occurrence of the two-point contact, were included in the analyses. The main purpose was to gain an insight into the dynamic effects during the wheel/rail contact transition.

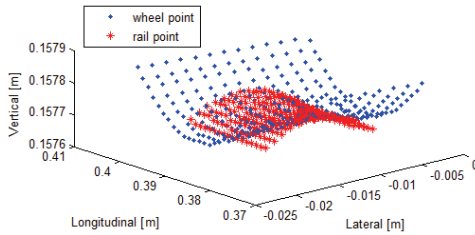
6.3.1 Contact positions

Three different AoAs – 15, 20 and 25 mrad – were adopted in the simulations to emphasise the dynamic effects brought about by the unstable vibrating wheel. The simulated wheel-rail contact positions in the solution zone with AoA=20 mrad are presented in Fig. 6.2 (a). The yellow area represents the rail surface in the solution zone. The origin of the coordinate system is at the centre of the rail bottom surface at the initial position of the wheel-rail contact. Hereafter, the coordinate system already includes the rail inclination in the track.

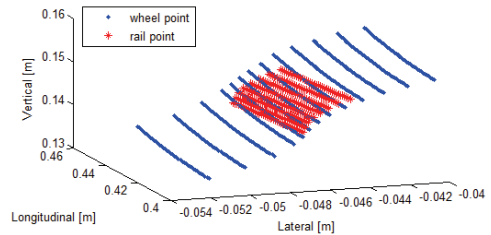


(a) Contact patch ‘footprints’ on the rail

(Blue for single-point contact and red for two-point contact)



(b) Coordinates of nodes in/around Patch 1



(c) Coordinates of nodes in/around Patch 2

Figure. 6.2: Contact patches in the solution zone

By applying explicit central difference time integration and a surface-to-surface contact-searching scheme based on a master-slave algorithm (see Section 2.6), the nodal forces in the solution zone in each time step can be calculated. The positions, shapes and areas of the contact patches were determined with the normal nodal force: a surface node is in contact if the normal nodal force is non-zero (Zhao & Li, 2011). Initially, the wheel-rail contact occurred only between the rail top and wheel tread. A trail of blue patches represents the ‘footprints’ of the single-point contact in a series of time steps. Due to the presence of an AoA, the wheel flange moved towards the gauge corner as the time step goes on and the second contact patch starts to appear. The ‘footprints’ of the contact patches in the case of two-point

contact are shown as two trails of red patches on the rail top and gauge corner. The coordinates of the wheel/rail nodes in and around the two oval-shaped contact patches (labelled as ‘Patch 1’ and ‘Patch 2’ in Fig. 6.2 (a)) from the same time step are plotted in Fig. 6.2 (b) and (c). The contact angle within the range of ‘Patch 2’ was between approximately 65° and 75° . The local lateral and longitudinal directions of Patches 1 and 2 on the rail surface are denoted by vectors x_1 and y_1 and vectors x_2 and y_2 , respectively, as shown in Fig. 6.2 (a).

6.3.2. Contact forces

The time histories of the normal load and the lateral and longitudinal creep forces at the two contact patches are plotted in Fig. 6.3 with different AoAs. With the same initial wheel-rail clearance and train speed, a larger AoA led to a larger lateral speed and consequently an earlier occurrence of the two-point contact. This can be identified according to the positions of the sudden jumps and drops of the curves in Fig. 6.3. The earliest two-point contact occurred at 0.29 m, when $AoA=25$ mrad. A non-steady-state feature (inconstant statistical properties along the time history) of the contact forces can be observed during the contact transition.

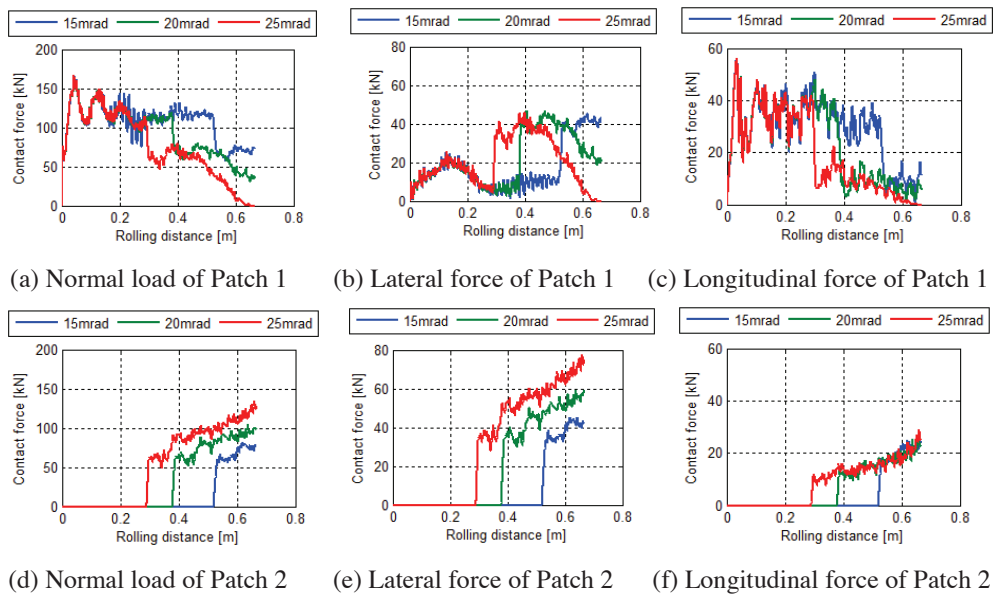


Figure. 6.3: Time history of the wheel-rail contact force

The oscillations of the curves before 0.29 m in Fig. 6.3 (a), (b) and (c) are due to vibrations excited by the initial kinetic and potential energy in the unbalanced system. Because the oscillations are damped out to less than 10% of the static values at 0.29 m, they have only a slight influence on the contact solutions presented in the following sections. The wheel-rail rolling always physically excites vibrations of the structure and waves in the continua. Thus, the real-world quantities fluctuate around their equilibrium values. When flange contact arose, the normal load and longitudinal creep force of Patch 1 in Fig. 6.3 (a) and (c) decreased,

whereas those of Patch 2 in Fig. 6.3 (d) and (f) increased, indicating that they were transmitted from Patch 1 to Patch 2. The time histories of the lateral creep forces follow a different trend; specifically, they jump at both contact patches, as shown in Figs. 6.3 (b) and (e).

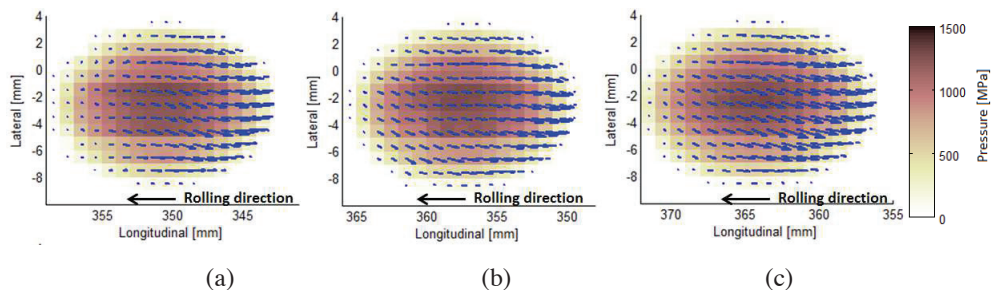
It can be expected that under the prescribed boundary condition shown in Fig. 6.1 (a), the wheel will tend to climb up on the rail when flange contact occurs. In this process, the contact forces of Patch 2 in all 3 directions will continue to increase, whereas those of Patch 1 will gradually decrease to zero. Then, the wheel tread will lose contact with the rail top, and all contact loads will be supported by Patch 2. This entire process was reproduced by the simulation with $AoA=25$ mrad. The simulated rolling distance in all 3 cases is sufficient to cover the transition from single-point to two-point contact.

In reality, the non-steady-state transition may last for a given period of time and then become (quasi-) steady at a certain moment when the transient effects decay. This phenomenon leads to research questions that should be addressed in future studies. For example, future studies should consider investigating the boundary conditions under which and at which moment a (quasi-) steady state can be achieved and to what extent the frictional rolling contact may affect this process.

As shown in Fig. 6.3, the main trends of the simulated contact forces with different AoAs are similar. This is also true for the contact solutions analysed in the following sections. Therefore, only the results with $AoA=20$ mrad will be presented unless additional information can be provided by other simulations.

6.3.3. Pressure and surface shear stress

Stress analyses are crucial to understanding and predicting wheel/rail damage, such as wear and RCF (Zerbst *et al.*, 2009). The evolution of the contact pressure, together with the direction and magnitude of the surface shear stress, are plotted in the contour/vector diagrams in Figs. 6.4 and 6.5 for Patches 1 and 2, respectively. The pressure magnitude corresponds to the depth of colour within the contact patch, as indicated by the colour bar. It shows that the size of Patch 1 shrinks and the size of Patch 2 expands once it has arisen at (f). Fig. 6.5 (i) only shows a part of Patch 2; the other part is out of the solution zone, i.e., beyond 0.45 m. Due to the existence of the AoA, the symmetrical axes of Patch 2 (if they exist) are not parallel to the lateral and longitudinal axes of the coordinate system, as in the case of Patch 1; in addition, the centres of Patches 1 and 2 from the same time step are not aligned along the lateral direction, as indicated in (Vo *et al.*, 2015). The maximum pressures of both patches are approximately in the middle of the respective patches.



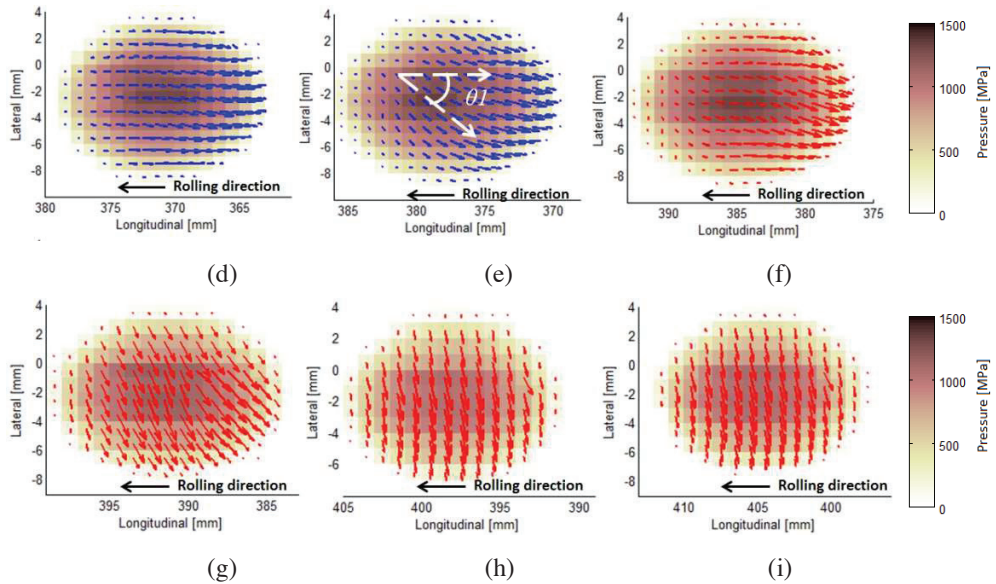


Figure. 6.4: Evolution of pressure and surface shear stress distributions in Patch 1 (Blue colour for shear stress indicates single-point contact; red indicates two-point contact)

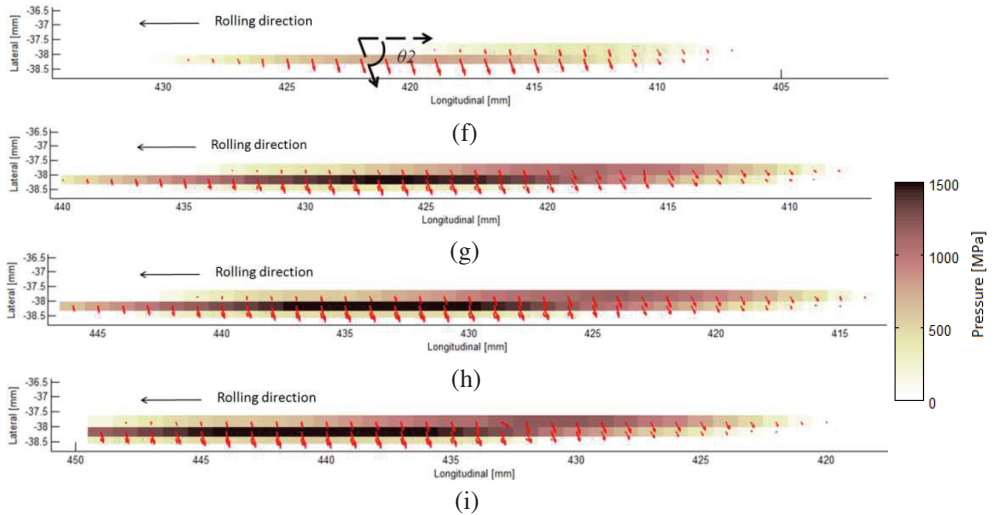
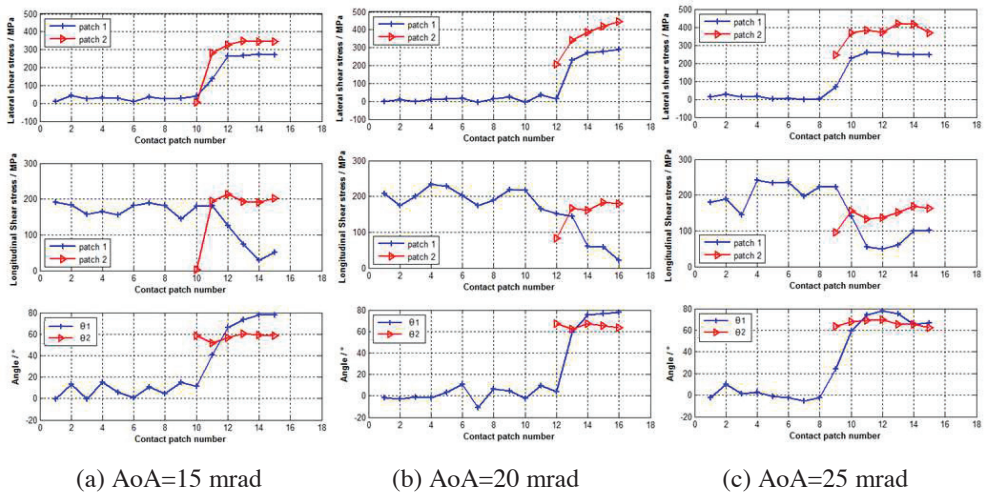


Figure. 6.5: Evolution of pressure and surface shear stress distributions in Patch 2 (Red colour for shear stress indicates two-point contact)

The surface shear stresses in single-point and two-point contact are indicated by blue and red arrows, respectively. The arrows point in the direction of the shear stress, and their lengths are proportional to the magnitudes. To characterise the direction of the surface shear stress, the

orientation angle between the stress vector and the negative direction of the longitudinal axis is denoted as $\theta 1$ and $\theta 2$ in Patches 1 and 2, respectively, as labelled in Figs. 6.4 (e) and 6.5 (f). $\theta 1$ is typically small under a single-point contact (Fig. 6.4 (a)-(e)), but it increases rapidly to approximately 90° under two-point contact (Fig. 6.5 (f) - (i)) and as the participation of the second contact patch increases (Fig. 6.5 (f) - (i)). $\theta 1$ decreases from the leading part to nearly zero in the trailing part, when single-point contact occurs; this gradual change in $\theta 1$ is likely caused by the geometry spin near the flange root in combination with the AoA with which the wheel negotiates a curve. Fig. 6.5 illustrates that $\theta 2$ changes only slightly from the first occurrence of Patch 2 onwards.

The change in the directions of the surface shear stress when two-point contact occurs results from the changes in the magnitude of the stresses in the lateral and longitudinal directions. The specific changes in the magnitude of the surface shear stress in the lateral and longitudinal directions, as well as $\theta 1$ and $\theta 2$, are presented in Fig. 6.6 for 3 different AoAs.



(a) AoA=15 mrad (b) AoA=20 mrad (c) AoA=25 mrad
 Figure. 6.6: Changes in the surface shear stresses and orientation angles with different AoAs (upper graphs: lateral stress; middle graphs: longitudinal stress; bottom graphs: orientation angle)

The values adopted in Fig. 6.6 are the average of all elements within the contact patch. The abscissa of the figures is the serial number of the contact patch in the evolution (from a series of time steps), with an interval of 6.7 mm. For all three AoA values, the lateral shear stress (upper row of Fig. 6.6) increases dramatically when Patch 2 arises, and the lateral shear stress of Patch 2 is larger than that of Patch 1. As shown by Figs. 6.3 (c) and (d), the lateral creep forces at the two contact patches are similar in the early period of the transition (within 0.1 m after the jumps of the curves), whereas the lateral shear stress of Patch 2 is larger because of its smaller size. In the middle row of Fig. 6.6, the longitudinal shear stress of Patch 1 declines to a certain extent because of the participation of Patch 2. The bottom row shows that the absolute value of $\theta 1$ stays in the range of less than 20° in the stage of single-point contact, jumping to approximately 70° in 2~3 output time steps once Patch 2 appears. $\theta 2$ is always between 60° and 70° . This narrow range of high values may be related to the initiation and

growth of head checks, whose orientation is also typically within a narrow range of angles, and their developments are approximately perpendicular to the direction of the surface shear stress (or tangential force) (He *et al.*, 2015). In addition, the calculated large pressure (up to 1,500 MPa) and surface shear stress (up to 450 MPa) with a large orientation angle θ_2 at Patch 2 may lead to severe wear (Sundh & Olofsson, 2008) and downwards plastic flow at the rail gauge corner (Li, 2002). A typical rail sample with severe wear and downwards plastic flow at the gauge corner can be found in Fig. 6.7.

A comparison of the shear stresses under different AoAs in Fig. 6.6 illustrates that with increases in the AoA, the lateral shear stress of Patch 2 increases but the longitudinal shear stress decreases, causing an increase in θ_2 . For Patch 1, the longitudinal shear stress is slightly raised by applying a larger AoA, as shown in the middle row of Fig. 6.6, because a smaller longitudinal load is transmitted to Patch 2 (compare Figs. 6.3 (e) and (f)). This comparison must be made at the incipient moment of the two-point contact, that is, the curves in Figs. 6.3 (e) and (f) should be shifted such that the jumps of the curves between 0.2 and 0.6 m coincide to render the difference at the jump visible.



Figure. 6.7: severe wear and downwards plastic flow at the rail gauge corner

6.3.4. Adhesion-slip distribution

The division of the adhesion and slip regions in the contact patch is an important feature of the frictional rolling contact. It can be derived by comparing the value $F_n \times f - F_t$ with a tolerance ε_T , where F_n , F_t and f are the pressure, surface shear stress, and friction coefficient, respectively, and ε_T is set as a percentage of the largest tangential nodal force in the contact patch (see Section 3.4.3). The pressure and surface shear stresses plotted in Figs. 6.8 and 6.9, respectively, under single-point and two-point contact conditions were extracted from the stress distribution graphs in Figs. 6.4 and 6.5 along the longitudinal centre lines of the contact patches.

Because the stress and adhesion-slip area distributions in single-point contact have been well studied in the literature (Zhao & Li, 2011; Deng *et al.*, 2015), only the results of one time-step (extracted from Fig. 6.4 (b)) are presented in Fig. 6.8. These results correspond well with the results in (Zhao & Li, 2011; Deng *et al.*, 2015).

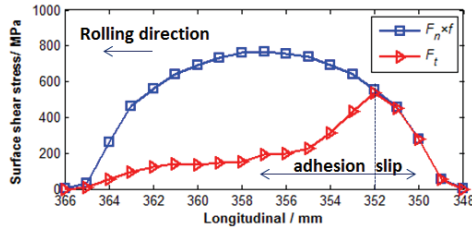


Figure. 6.8: Stress distribution along the longitudinal axis under single-point contact

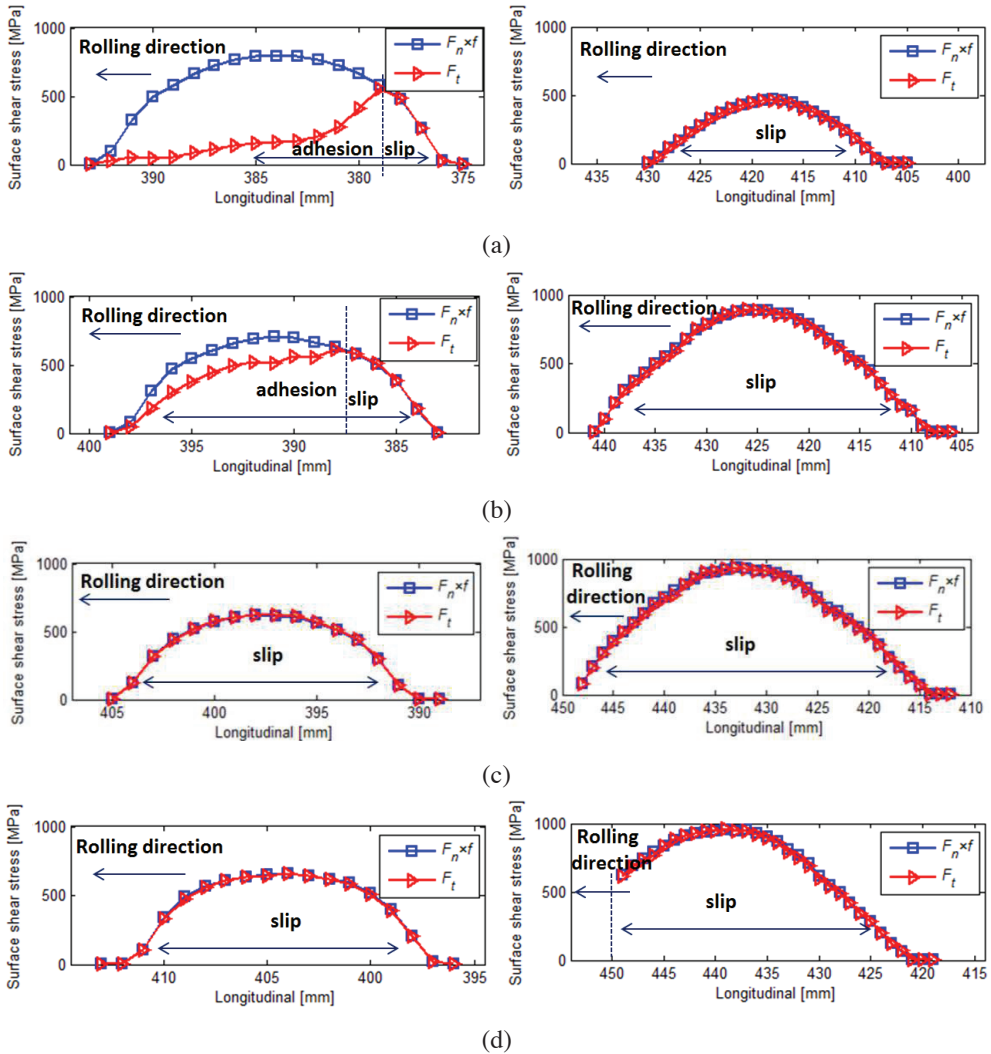


Figure. 6.9: Stress distribution along the longitudinal axis under two-point contact condition (left-hand side graphs: Patch 1; right-hand side graphs: Patch 2)

The adhesion-slip area distributions in Figs. 6.9 (a), (b), (c) and (d) for two-point contact correspond to the stress distributions in Figs. 6.4 (f), (g), (h) and (i), respectively. The left-hand side graph of Fig. 6.9 (a) is similar to that of single-point contact in Fig. 6.8. With the progression of the transition, the adhesion area in Patch 1, indicated by the gaps between the two curves, is reduced in Fig. 6.9 (b) and has completely vanished in Figs. 6.9 (c) and (d).

The right-hand side graphs of Fig. 6.9 (a) show that when the second patch has just come into being, its size is small and its pressure and surface shear stress are low compared to those in Figs. 6.9 (b), (c) and (d). For the same reason as in Fig. 6.5 (i), only a part of Patch 2 is included in Fig. 6.9 (d). The graphs also show that Patch 2 is fully in slip so far, namely, $F_n \times f = F_t$, according to the Coulomb's law employed in the model.

Figs. 6.9 (c) and (d) illustrate that due to the two-point contact, the entire contact area, including Patches 1 and 2, evolved into complete slip. This may further lead to unstable stick-slip rolling, an important cause of 'rutting' (a specific type of short-pitch corrugation in curves) (Grassie, 2009) and curve squeal noise (Thompson, 2009).

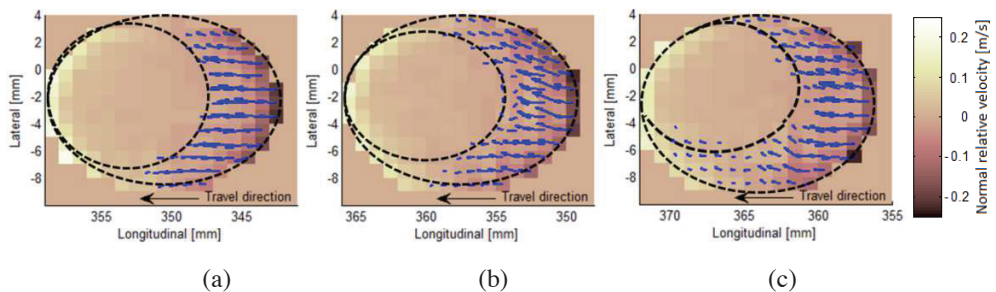
6.3.5. Wheel-rail relative velocity

The analyses of the wheel-rail relative velocities in the contact patch were distinguished in the normal and tangential directions. The evolution of the distributions of the wheel-rail relative velocities in both directions are combined in the contour/vector diagrams in Figs. 6.10 and 6.11 for Patches 1 and 2, respectively.

6.3.5.1 Micro-slip

The tangential wheel-rail relative velocity, the so-called micro-slip, refers to the relative velocity between two contact particles. The adhesion-slip area distribution can also be derived from the micro-slip analysis. The contact and adhesion regions of Patch 1 are indicated by black ovals in Fig. 6.10. The adhesion-slip distributions shown here are in line with the results obtained by the stress analyses in Figs. 6.8 and 6.9.

Similar to the stress distribution shown in Figs. 6.4 and 6.5, the micro-slips under single-point and two-point contact conditions are also indicated by blue and red arrows, respectively. The arrows point in the directions of the micro-slip, and their lengths are proportional to the magnitudes. A comparison of the micro-slip graphs with the surface shear stress graphs illustrates that the general direction of the micro-slip is opposite to and changes together with the direction of the surface shear stress: as the transition proceeds, the direction of the micro-slip in Patch 1 changes from in the longitudinal direction ($\theta \approx 0^\circ$) to in the lateral direction ($\theta \approx 90^\circ$), whereas the change in direction for the Patch 2 micro-slip is less pronounced.



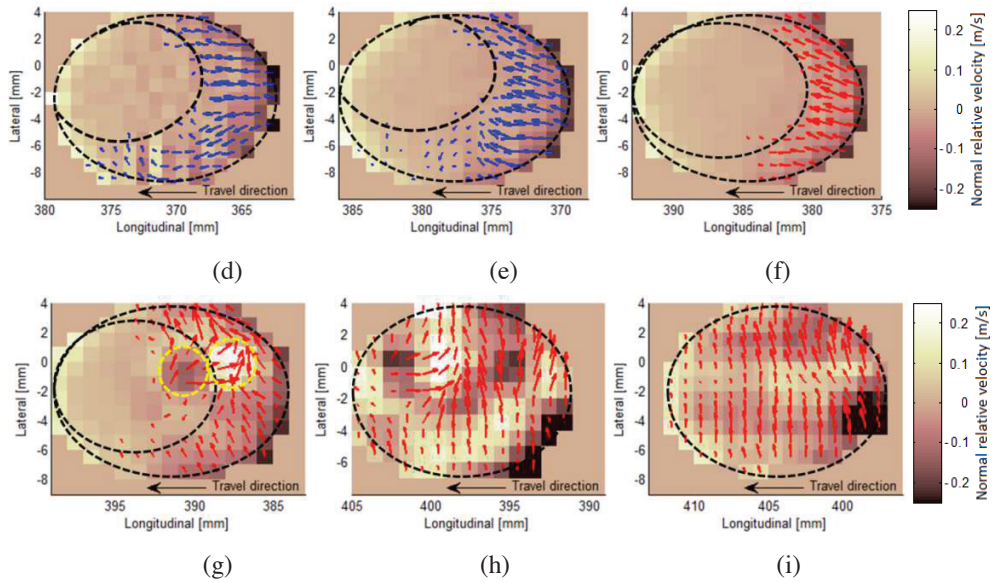


Figure 6.10: Evolution of the distribution of the wheel-rail relative velocity in Patch 1

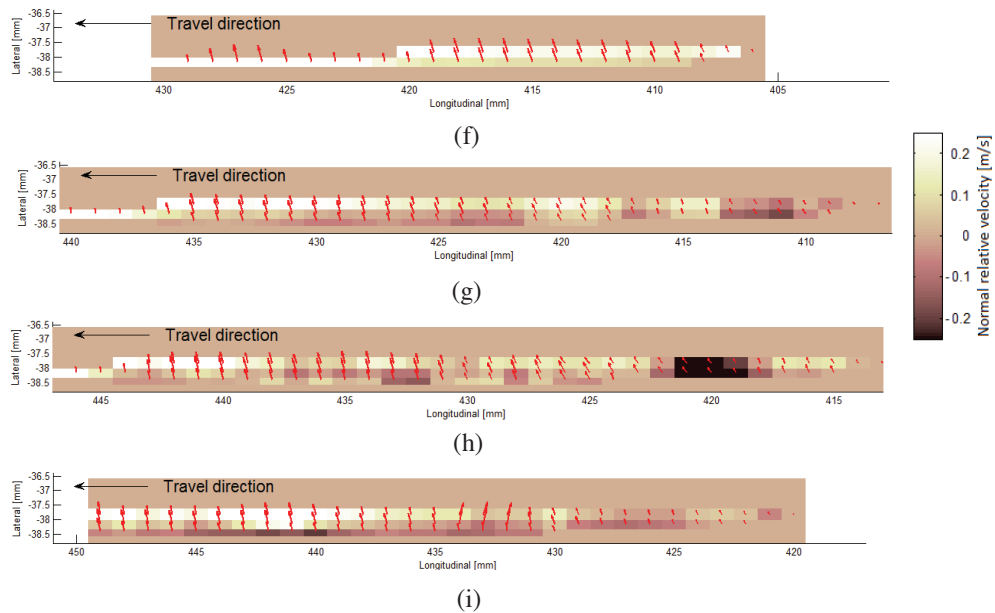


Figure 6.11: Evolution of the distribution of the wheel-rail relative velocity in Patch 2

6.3.5.2 Normal relative velocity

The magnitude of the normal relatively velocity is indicated by the colour depth within the contact patches in Figs. 6.10 and 6.11 for single-point and two-point contact, respectively. The colour outside the contact patch corresponds to a zero relative velocity, whereas a positive (lighter colour) or negative (darker colour) relative velocity corresponds to the condition that the wheel and rail surface elements move towards or away from each other, respectively. The colours at the leading and trailing edges of the contact patch are lighter and darker, respectively.

6.3.5.3 Local intensification and relaxation of compression

Because the surface elements of the wheel and rail were in contact, the further movement towards or away from each other caused the transient intensification or relaxation of the contact, respectively. Therefore, the lighter or darker areas within the contact patches in Figs. 6.10 and 6.11 reflect the transient local compression intensification or relaxation, respectively.

6.3.5.4 Contact perturbation and waves

Figs. 6.10 and 6.11 illustrate the influence of the transient dynamics on the wheel-rail contact. Such local dynamics, coming from the wheel-rail vibrations and wave propagation, is less visible in the stress analyses of Figs. 6.4 and 6.5 because the vibrating displacements in the contact patch are not sufficiently large to cause a clear stress perturbation, although they do affect the stress distribution, as reported in (Zhao & Li, 2011). As the first-order derivative of the displacement, the vibrating velocity is more sensitive to the dynamic perturbation.

Comparing Figs. 6.10 (f) and (g) illustrates that under the two-point contact condition, a perturbation of micro-slip, i.e., the chaotic direction of the micro-slip, is likely to be initiated next to the juncture of the adhesion and slip regions, where the maximum surface shear stress is located, as shown in the yellow ovals in Fig. 6.10 (g). Moreover, this tangential perturbation arises together with the transient local compression intensification and relaxation at the same location of contact patch, indicated by the lighter and darker spots, respectively, in the yellow ovals.

Figs. 6.10 (a) to (e) for the single-point contact illustrate that a perturbation of an (irregular) micro-slip distribution appears to start at the leading bottom part of the contact patch and propagate upwards and towards the trailing direction. The expansion of this perturbation, together with the increasing geometrical spin when approaching flange contact, causes the adhesion region to move upwards in the contact patch, similar to the micro-slip distribution simulated with the large lateral creepage shown in Fig. 5.6.

Compared to the single-point contact condition, a more obvious local compression intensification and relaxation is observed in the two-point contact condition. Embodied in the alternation of the compression intensification and relaxation, an intensification-relaxation wave can be observed within the contact patch. The wave appears to propagate radially, as shown in Fig. 6.10 (h), or parallel to the micro-slip vectors, as shown in Fig. 6.12, calculated for the case of $AoA=25$ mrad. According to the vibration frequencies of the surface nodes and the wavelengths observed in Fig. 6.10 (h) and Fig. 6.12, the wave propagating speed can be estimated as about 3 km/s, close to Rayleigh wave speed in steel. Moreover, the phase difference between normal and tangential surface nodal vibrations is approximate $\pi/2$, corresponding well with the feature of Rayleigh wave. The properties of the observed waves will be discussed in detail in Chapter 7.

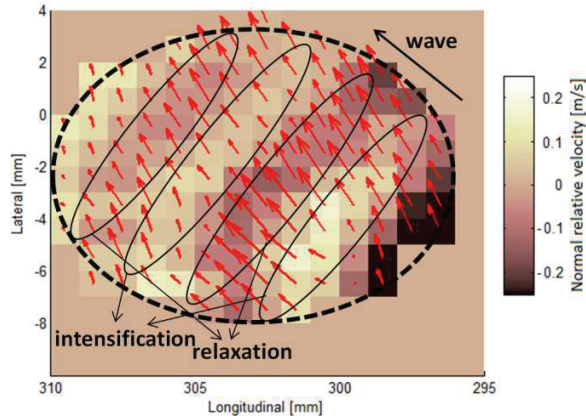


Figure. 6.12: Distribution of wheel-rail relative velocity in Patch 1 under two-point contact condition with $AoA=25$ mrad

As shown in Figs. 6.11 (d), (g), (h) and (i), as well as in Fig. 6.13, the perturbation of the micro-slip always comes together with the transient local compression intensification and relaxation at the same location. Moreover, the micro-slips in the relaxation areas are normally larger than those in the adjacent intensification areas. This inhomogeneous distribution of reciprocating motion within the wheel-rail contact could cause fretting.

6.4. Summary of the modelling of wheel-rail contact transition

This chapter simulated non-steady-state rolling contact with a transition from single-point to two-point contact by an explicit FEM. The structural dynamics of the wheel-track system was coupled with the continuum dynamics of frictional rolling. The stress and adhesion-slip distribution under the single-point contact condition and the positions and shapes of the contact patches under the two-point contact condition corresponded well with the results in the literature. The major findings of the chapter are as follows:

- Transient dynamic effects were captured by the relative velocity in the wheel-rail contact.
- Wave propagation was excited in the wheel and rail continua, especially by the transition from single-point to two-point contact. The vibrations and waves may cause local compression intensification and relaxation of the contact, as well as local perturbation of the micro-slip.
- The compression intensification and relaxation and the micro-slip perturbation always occur simultaneously and at the same locations, and they are likely initiated next to the juncture of the adhesion and slip regions in the contact patch, where the maximum surface shear stress is located.
- The intensification-relaxation wave appears to propagate radially or parallel to the micro-slip vectors. The micro-slip in the relaxation area is larger than that in the adjacent intensification area. This phenomenon may cause fretting.
- Compared to those in single-point contact, stronger waves, the resulting micro-slip perturbation, and the transient local compression intensification and relaxation can be

observed upon the occurrence of the second contact point. Moreover, the contact transition can cause the full slip of the entire wheel-rail contact. These factors may contribute to contact instability and ultimately squeal and corrugation.

- The intensification and relaxation may reflect certain important wheel-rail dynamic characteristics, whereas the irregular micro-slip mirrors the frictional contact perturbation. Thus, the calculated wheel-rail relative velocities appear to connect the wheel-rail dynamic properties to the frictional rolling contact, plausibly providing a more physical and sensitive method than those relying on the steady-state contact force calculation.

7

DYNAMIC-INTERACTION-INDUCED WAVES

Chapter 2 has illustrated theoretically that the explicit FE wheel-rail dynamic interaction model is computationally attractive for analysing high-frequency dynamic problem especially in the case of wave propagation. The explicit FE contact solution may include all the relevant vibration modes of structures and continua, and the associated wave propagations. This chapter investigates the generation mechanisms (Section 7.1) and types (Section 7.2) of the dynamic-interaction-induced waves produced by the numerical simulations presented in Chapters 4-6, and proposes a potential application of the wave study for rail crack detection (Section 7.3).

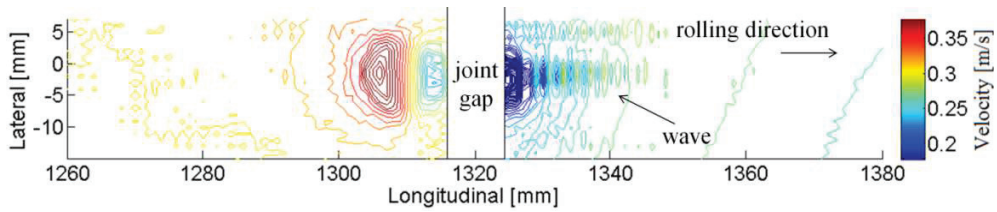
7.1. Categorisation and generation mechanisms of the simulated waves

The waves observed in the wheel-rail dynamic contact solutions presented in Chapters 4-6 may be categorised according to the generation mechanism as impact-induced wave (Section 7.1.1), large-creepage-induced wave (Section 7.1.2) and perturbation-induced wave (Section 7.1.3). The generation mechanisms of the former two are evident: wheel-rail impacts and large creepage cause significant dynamic effects, which result in large oscillations of nodes on wheel and rail surfaces in the vicinity of the contact patch. The large nodal oscillations then propagate radially and form regular wave patterns. The generation mechanism of the perturbation-induced wave is, however, less apparent because the perturbation may arise in seemingly 'steady-state' rolling.

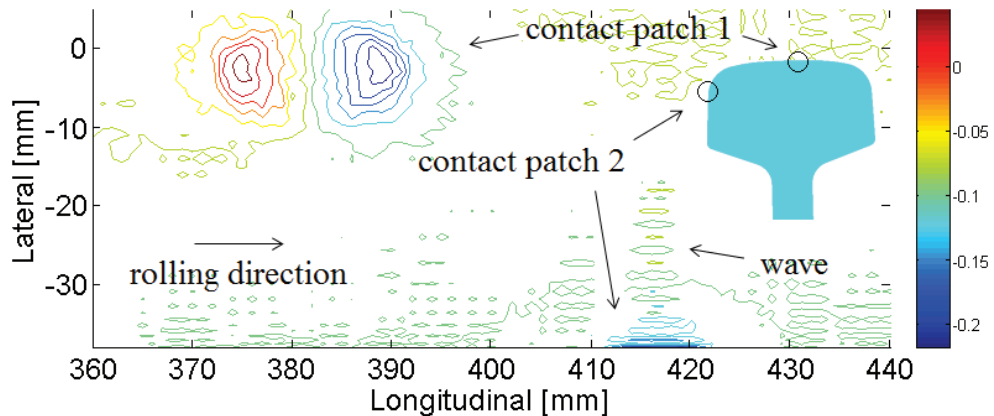
7.1.1 Impact-induced waves

The contour graphs in Fig. 7.1 present two examples of the impact-induced wave, i.e., the wave generated by wheel-rail impacts. Because impact excitations are normal to the wheel-rail contact surfaces, the normal nodal vibrating velocities play more important roles than the tangential ones in the formation of the impact-induced wave (see Fig. 4.27). The magnitude of the normal nodal velocity on the rail surfaces is indicated by the colour depth of the contour graphs; the leading and trailing parts of the contact patch may thus be identified by the blue and red colour, respectively.

Fig. 7.1 (a) shows an impact-induced wave produced by the wheel-IRJ impact simulation with measured contact geometry presented in Chapter 4. When the wheel rolled over the IRJ and hit the rail ends on the other side of the joint, an impact-induced wave occurred at the leading part of the contact patch and propagated forward along the wheel rolling direction. Fig. 7.1 (b) shows another impact-induced wave produced by the contact transition model presented in Chapter 6. The impact-induced wave arisen at contact patch 2 at the moment that the wheel flange came into contact with, or hit, the rail gauge corner. The corresponding animations of Figs. 7.1 (a) and (b) can be found at ("Animation for Fig. 4.27, <https://youtu.be/fAg99j6kquI> ; [accessed 16.11.22] ") and ("Animation for Fig. 7.1 (b), <https://youtu.be/KKSV7A1tCD0>,"), respectively, displaying the generation and propagation of the impact-induced wave.



(a) Produced by the wheel-IRJ impact simulation



(b) Produced by the contact transition simulation

Figure. 7.1: Impact-induced wave patterns

7.1.2 Large-creepage-induced waves

When large creepage occurs between wheel and rail, wave patterns embodied in the alternation of the compression intensification and relaxation (see Fig. 5.6 (f) and Fig. 6.12) may be generated. Two examples of the large-creepage-induced wave are presented in the contour/vector diagrams in Fig. 7.2. The large-creepage-induced wave shown in Fig. 7.2 (a) was simulated with the model with large lateral motion of wheel (simulation case 4 presented in Chapter 5) and the one shown in Fig. 7.2 (b) was simulated by the model of contact transition (presented in Chapter 6), in which large creepage occurred between the rail top surface and wheel tread when the wheel negotiated with the rail via flange contact. The corresponding animations of Figs. 7.2 (a) and (b) displaying the generation and propagation of the large-creepage-induced wave can be found at ("Animation for Fig. 7.2(a), <https://youtu.be/yRD9EDasMmU>,") and ("Animation for Fig. 7.2(b), <https://youtu.be/tQwWTc-GfHw>,"), respectively.

As Figs. 5.6 and 6.12, the contour/vector diagrams in Fig. 7.2 indicate the magnitudes of the normal relatively velocities by the colour depth within the contact patches and indicate the micro-slips by arrows. The blue arrows point in the directions of the micro-slip, and their lengths are proportional to the magnitudes. Both the normal and tangential nodal velocities contribute to the formation of the large-creepage-induced wave (elaborated later in Section 7.2). The large-creepage-induced wave appears to propagate parallel to the micro-slip vectors and the micro-slip in the relaxation area is larger than that in the adjacent intensification area.

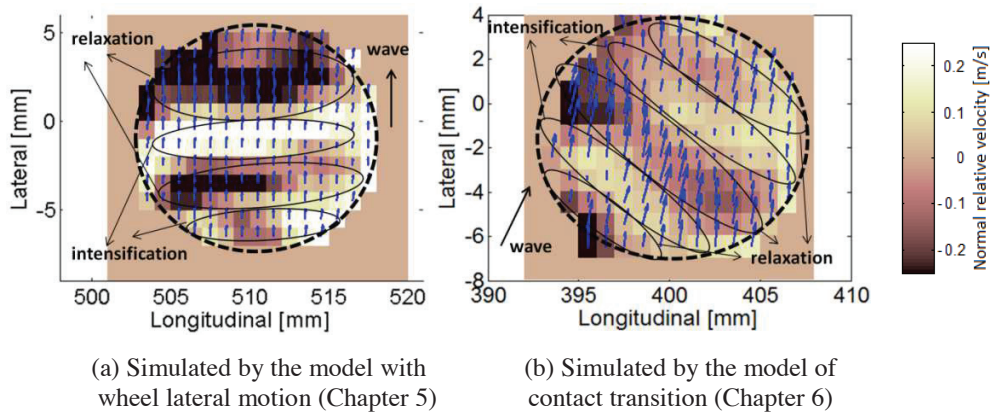


Figure 7.2: Large-creepage-induced wave patterns

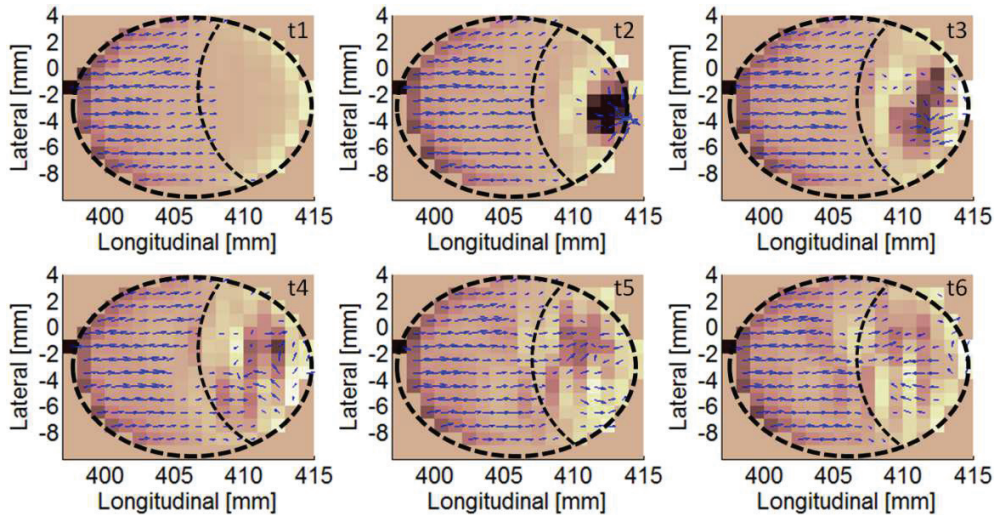
7.1.3 Perturbation-induced waves

The perturbation-induced wave has been frequently observed in the three numerical explicit FE examples: perturbation of nodal velocity suddenly occurred within contact patch and spread radially, consequently developing into a wave pattern. As indicated by a typical example presented in Section 4.6.1, the main difference of the perturbation-induced wave with the former two wave types is that the perturbation-induced wave, or the perturbation to be precise, may be initiated in a seemingly ‘steady-state’ rolling without involving significant dynamic effects caused by non-steady-state contact conditions, e.g., impact contact, contact with unsteady creepage and contact transition.

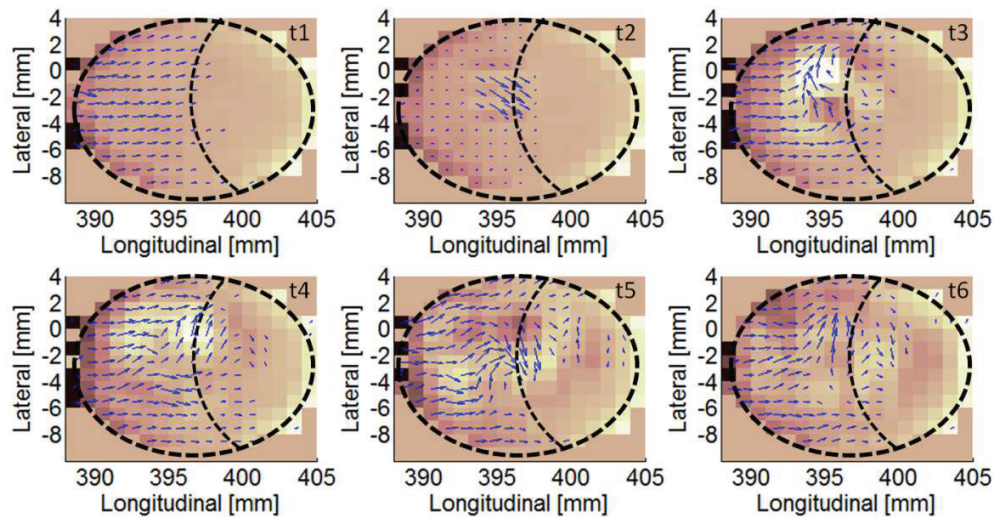
In addition, the initiation of the perturbation has been found either close to the leading edge of the contact patch (see Fig. 4.26) or at the juncture of the adhesion-slip regions (see Fig. 6.10 (g)). Two animations of the generation and propagation of the perturbation-induced wave are presented at ("Animation for Fig. 7.3 (a), <https://youtu.be/BqFapqG8D-Q>," and ("Animation for Fig. 7.3(b), <https://youtu.be/CE1rB0N-IVk>,"). They were simulated with the wheel-rail interaction model without significant dynamic effects (simulation case 1 presented in Chapter 5). The perturbation initiates close to the leading edge of the contact patch in ("Animation for Fig. 7.3 (a), <https://youtu.be/BqFapqG8D-Q>," and at the juncture of the adhesion-slip regions in ("Animation for Fig. 7.3(b), <https://youtu.be/CE1rB0N-IVk>,").

Each animation consists of two windows: the upper window displays the simulated evolution of wheel-rail relative velocities within the contact patch and the lower window displays the simulated evolution of the normal and tangential velocities of the rail surface nodes within the whole solution zone. The evolution of the rail surface nodal velocities may indicate the wave propagation more obviously, while the distribution of the wheel-rail relative velocities may clearly indicate the range of contact patch and adhesion-slip regions, and thus locate the initiation position of the perturbation. Fig. 7.3 shows the generation processes of the two perturbation-induced waves extracted from the upper windows of animations ("Animation for Fig. 7.3 (a), <https://youtu.be/BqFapqG8D-Q>," and ("Animation for Fig. 7.3 (b), <https://youtu.be/CE1rB0N-IVk>,"). The range of the contact patch is indicated by dashed black ovals and the ‘initial’ adhesion and slip regions are divided by dashed curves. The interval between each two consecutive graphs in Fig. 7.3 as well as the time step of the animations in

("Animation for Fig. 7.3 (a), <https://youtu.be/BqFapqG8D-Q>,") and ("Animation for Fig. 7.3(b), <https://youtu.be/CE1rB0N-IVk>,") is $1 \mu\text{s}$. The perturbation occurred at instant t_2 close to the leading edge of the contact patch in Fig. 7.3 (a) and at the juncture of the adhesion-slip regions in Fig. 7.3 (b), and then spread gradually at instants t_3 ~ t_6 .



(a) Perturbation initiates at the leading edge of contact patch



(b) Perturbation initiates at the juncture of adhesion-slip regions

Figure 7.3: Generation processes of two perturbation-induced waves

In Fig. 7.3, the adhesion-slip regions determined by the wheel-rail micro-slip varied significantly after the perturbation occurred, whereas that determined by comparing the

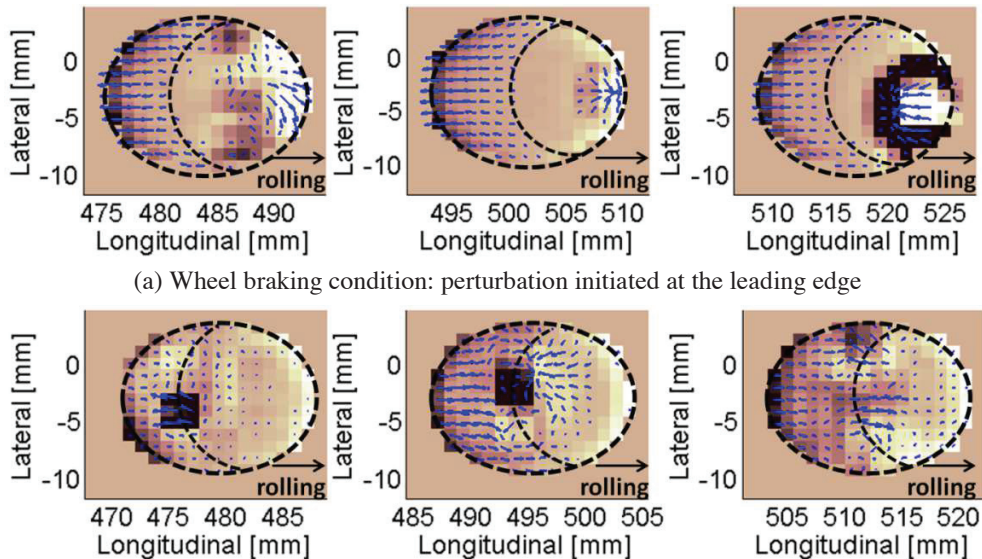
calculated traction bound and shear stress (not shown here) were largely in line with the 'initial' adhesion-slip regions divided by the dashed curves. The discrepancy is attributed to the different sensitivities of the approaches to determining slip region mentioned in Section 5.3.2.3: the micro-slip calculated with the wheel-rail relative velocity may reflect dynamic effects more sensitively than the contact stress calculated with the relative displacement.

In addition, note that the shear stress is close to the traction bound at the initiation locations of the perturbation-induced waves, i.e. near the leading edge and near the juncture of the adhesion-slip regions; therefore, the contact nodes originally in adhesion at these locations are more likely to slip due to an increase of shear stress or decrease of traction bound (or decrease of pressure since constant friction coefficient is used) that possibly occurs in the wheel-rail dynamic interaction. Fig. 5.5 has indicated that the surface shear stress and the traction bound varies periodically but are not exactly in phase, and in each period a local peak of shear stress starts at the leading edge of the contact patch and exits the adhesion region at the juncture of the adhesion-slip region. This local peak of shear stress seems thus to cause a sudden slip in the original adhesion area, acting as a perturbation within the wheel-rail contact patch and then develops into a wave. Because the variation of stress distribution is caused by the dynamic effects of wheel-rail interaction, the perturbation-induced waves seem also to be generated intrinsically by the dynamic effects. The dynamic effects that trigger the perturbation-induced waves are less significant than those initiating the impact-induced wave or large-creepage-induced wave, though.

The initiation location of the perturbation-induced wave was found to be influenced by the traction condition of wheel model. Fig. 7.4 (a) and (b) extracted from animations ("Animation for Fig. 7.4 (a), <https://youtu.be/nC4szzxeJQw>,") and ("Animation for Fig. 7.4 (b), https://youtu.be/1vb_xsv5jvI,") show the perturbation-induced waves simulated by a wheel braking model and a traction model, respectively. The wheel braking condition was simulated by applying an opposite-direction torque to the wheel axle, the directions of the micro-slip vectors within the slip regions in Fig. 7.4 (a) are thus opposite to the wheel rolling direction. Fig. 7.4 and the corresponding animations indicate that the perturbation-induced wave occurred generally at the leading edge of the contact patch in the wheel braking condition, whereas it occurred more often at the juncture of the adhesion-slip regions in the wheel traction condition. The correspondence between the traction/braking condition and the initiation of the perturbation-induced wave suggests that the simulated waves should physically exist but not occur randomly as numerical errors. Experimental observation and validation should be conducted in the future to clarify this correspondence.

The perturbation occurred periodically in the animations ("Animation for Fig. 7.4 (a), <https://youtu.be/nC4szzxeJQw>,") and ("Animation for Fig. 7.4 (b), https://youtu.be/1vb_xsv5jvI,") with periods of approximately 0.6 ms (20 time steps), corresponding to the period of the stress oscillation shown in Fig. 5.5. This confirms that the perturbation may be generated when the local peak of surface shear stress passes the boundary of adhesion region also periodically. Moreover, Fig. 7.3 shows that the adhesion region decreased gradually with the spread of the perturbation. It can be expected that the adhesion region may vanish under certain dynamic contact condition (not simulated in this study), and the periodical friction saturation, the so-called stick-slip rolling contact, may thus occur with the periodical stress oscillation. This may further result in the wheel-rail friction-induced instability. Therefore, the frictional perturbation discovered in this study may be closely related to the dynamic friction-induced instability. Because the initiation of perturbation may be influenced by wheel traction condition, based on a better understanding of this wave

phenomenon, traction and braking control strategies may be optimised to mitigate squeal and corrugation in the future.



(a) Wheel braking condition: perturbation initiated at the leading edge

(b) Wheel traction condition: perturbation initiated at the juncture of adhesion-slip regions

Figure. 7.4: Perturbation initiated simulated by wheel braking and traction conditions

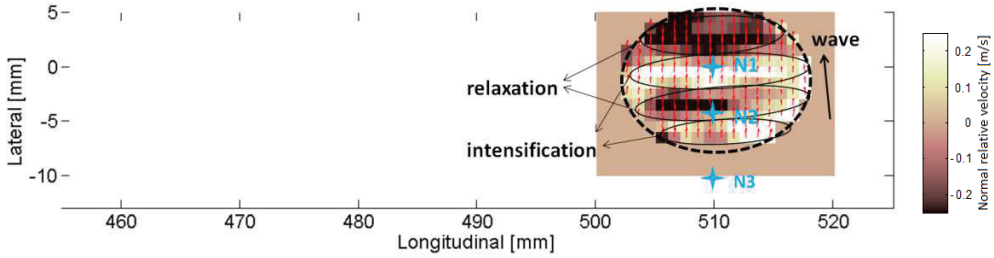
7.2. Type of the simulated waves

The wave reflection due to the joint (see Fig. 4.25 (b)) and wave interference due to two contact points (see ("Animation for Fig. 7.2(b), <https://youtu.be/tQwWTc-GfHw>,")) cause superposition of the waves simulated by the wheel-IRJ model and the contact transition model; the study of surface nodal motion forming the waves thus became complex, posing challenges in identifying the simulated wave type. This study, therefore, has so far been limited to the investigation of the wave type simulated by the model with wheel lateral motion, i.e., the large-creepage-induced wave.

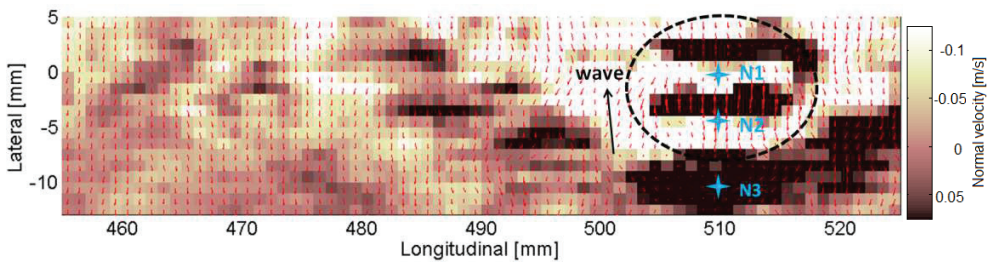
7.2.1 Preliminary inference of the wave type

A typical large-creepage-induced wave pattern simulated by the model with large lateral motion of wheel (simulation case 4 presented in Chapter 5) is presented in the contour/vector diagrams of Fig. 7.5 (see also ("Animation for Fig. 7.5, <https://youtu.be/jTbWh-FGxPc>,")) for the corresponding animation with a time step of $0.3 \mu\text{s}$). The wave phenomenon can be observed from the distribution of wheel-rail relative velocities within the contact patch shown in Fig. 7.5 (a) as well as the distribution of the rail surface nodal velocities within the whole solution zone shown in Fig. 7.5 (b). The contact patches are indicated by dashed black ovals in Fig. 7.5. As Figs. 5.6 and 6.12, the contour/vector diagrams indicate the magnitudes and directions of the normal (relatively) velocities by the colour depth, and those of the tangential (relatively) velocities by arrows. The wave in Fig. 7.5 (a) is embodied in the alternation of the compression intensification and relaxation within the contact patch, whereas the wave in Fig.

7.5 (b) is indicated by the vibrations of rail surface nodes. The wavelengths can be estimated to be approximately 6 mm.



(a) Distribution of wheel-rail relative velocities within the contact patch



(b) Rail surface nodal velocities within the whole solution zone

Figure. 7.5: Large-creepage-induced wave simulated by the model of wheel lateral motion

Assuming that the time step used in the animation ("Animation for Fig. 7.5, <https://youtu.be/jTbWh-FGxPc>,") – $0.3 \mu\text{s}$ – is sufficiently small for capturing the main characteristics of the wave, e.g., wave speed and traveling direction, and thus for identifying the wave type (this assumption will be proven to be valid in Section 7.2.3), three pieces of evidence may preliminarily attribute the simulated large-creepage-induced wave to Rayleigh wave. First, the observed wave is formed by the simulated rail surface nodal velocities, which can thus be considered as a type of surface wave; second, both the normal and the tangential nodal motion contribute to the formation of the wave, and the direction of the tangential nodal motion is roughly parallel but opposite to the wave propagation direction; third, the wave speed estimated by dividing the wave travelling distance 1 mm within each time step by the time step size $0.3 \mu\text{s}$ approximates to the Rayleigh wave speed in the steel (about 3 km/s).

7.2.2 Rayleigh surface waves

Rayleigh wave is a commonly known type of surface waves. It is formed by the retrograde elliptical particle motion on the surface as shown in Fig. 7.6: the surface particles move in both the tangential (parallel but opposite to the direction of wave propagation) and transverse directions (normal to the surface), and the phase difference between the tangential motion and the transverse motion is $\pi/2$. The travelling speed of Rayleigh wave in steel is approximately 3 km/s.

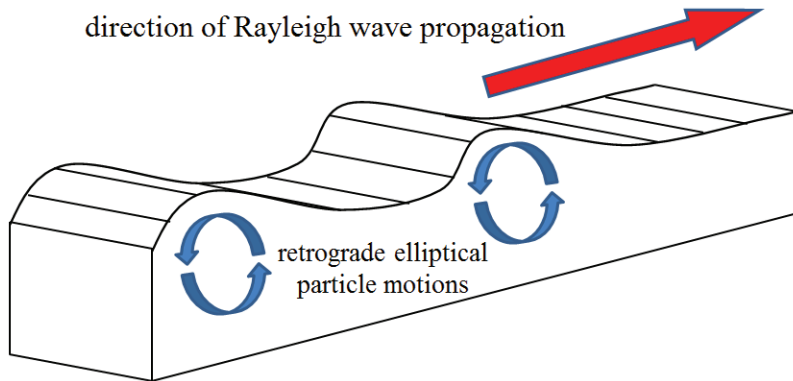


Figure. 7.6: Retrograde elliptical particle motion of Rayleigh wave

7.2.3 Nodal motion of the large-creepage-induced waves

The inference attributing the simulated large-creepage-induced wave to Rayleigh wave is based on the assumption that the time step is sufficiently small. If this is false, the estimated travelling speed and direction of the wave may be wrong. The simulated rail surface nodal motion is analysed in this subsection to confirm the inference of wave type.

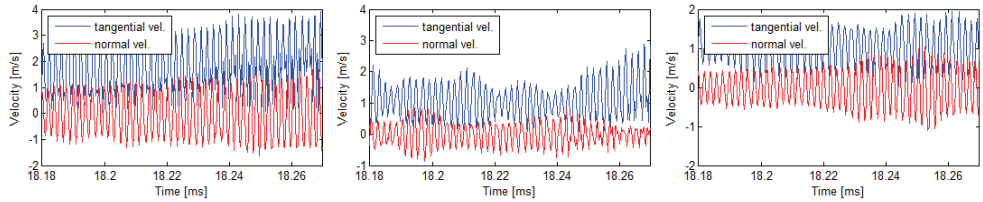
The normal and tangential velocities of three rail surface nodes N1~N3 located approximately along the lateral centre line of the contact patch, denoted by the blue stars in Fig. 7.5, were analysed. N1 and N2 are within the contact patch while N3 is outside the contact patch. The longitudinal coordinate of the selected nodes is 510 mm, while the lateral coordinates are 0 mm, -4 mm and -10 mm, respectively.

Time histories of the simulated normal and tangential velocities of the three selected nodes during the period of 18.18 s~18.27 ms (the same with the period of animation ("Animation for Fig. 7.5, <https://youtu.be/jTbWh-FGxPc>,")) are plotted in Fig. 7.7 (a). The tangential nodal velocities have trend components because of the large lateral motion of the wheel. The PSDs (power spectrum density) of the time histories shown correspondingly in Fig. 7.7 (b) indicate that all the nodal velocities are narrow-banded signals and have a dominant frequency around 0.495 MHz. The travelling speed of the simulated wave may thus be calculated by multiplying the wavelength $\lambda_w = 6$ mm and the frequency $f_w = 0.495$ MHz as:

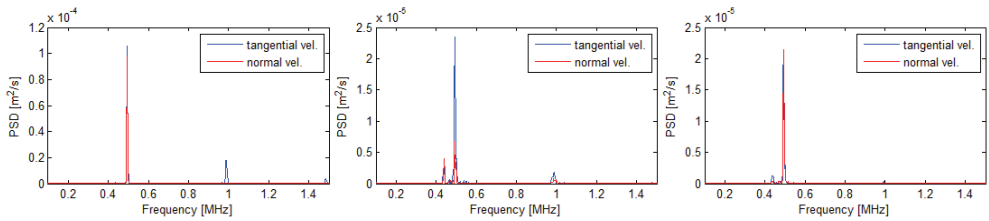
$$v_w = \lambda_w \times f_w \approx 3 \text{ km/s} \quad (7.1)$$

The agreement of the wave speed calculated by Eqn. (7.1) and that estimated by animation ("Animation for Fig. 7.5, <https://youtu.be/jTbWh-FGxPc>,") indicate that the time step of the animation is sufficiently small for capturing the main characteristics of the wave. The band-pass filtered time histories around the dominant frequency (between frequencies 0.48 and 0.51 MHz) are shown in Fig. 7.7 (c) and their close-up views are shown in Fig. 7.7 (d). Fig. 7.7 (e) indicates that the phases out of the tangential and normal signals of N1 and N2 inside the contact patch are approximately $\pi/2$, corresponding well to that of particles of Rayleigh wave, whereas that of N3 outside the contact patch is about 0.65π , possibly influenced by the involvement of other types of wave or the deformation of rail surface around the contact patch. Fig. 7.7 (f) shows that the coherence of the tangential and normal signals of N1~N3 are over 0.8 in the frequency range of interest. The Rayleigh-wave-like elliptical nodal motion of N1~N3 in displacement is plotted in Fig. 7.7 (g) (see also ("Animation for Fig. 7.7,

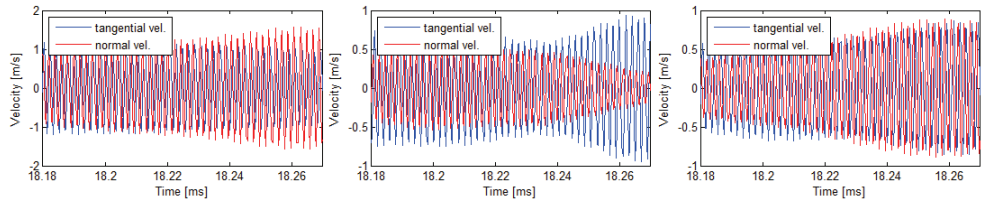
<https://youtu.be/XWyuY70mKI4>,") for the animations of the corresponding nodal motion). The elliptical trails of each node in different rounds do not exactly overlap due to the dynamic effects of wheel-rail interaction. The analysis of Fig. 7.7 confirms that Rayleigh wave may be generated in wheel-rail dynamic interactions and can be reproduced by the proposed explicit FEM.



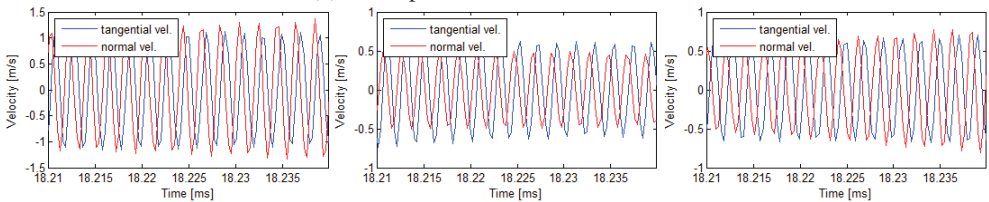
(a) Time histories



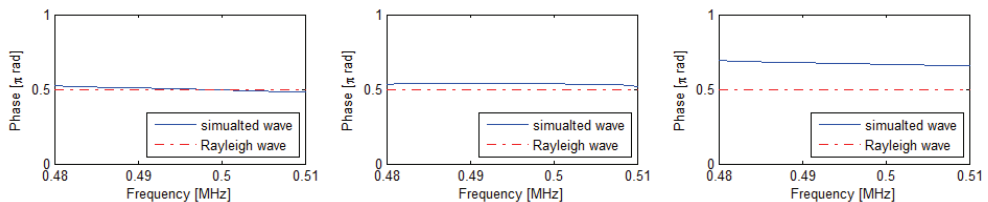
(b) PSDs



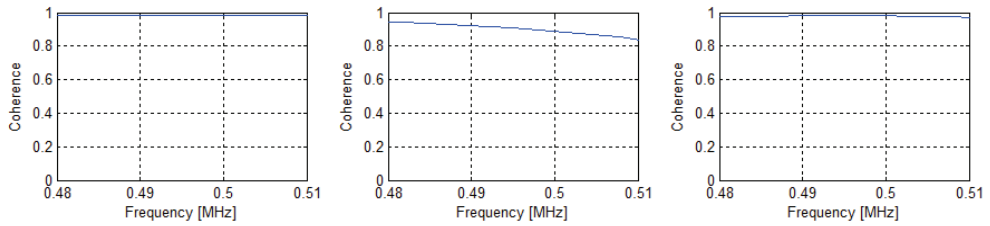
(c) Band-pass filtered time histories



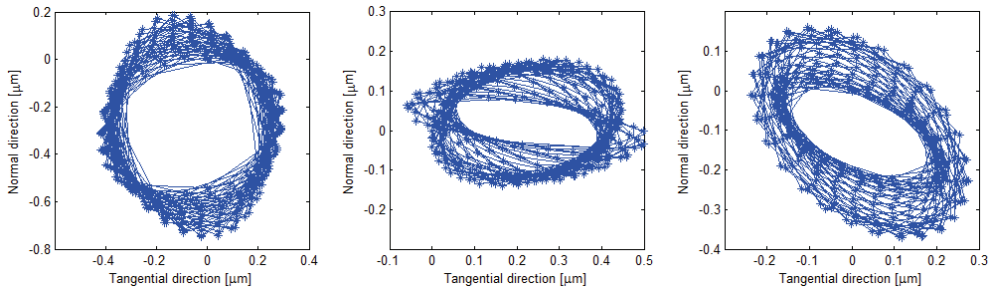
(d) Close-ups of the filtered time histories



(e) Phases out of the tangential and normal signals



(f) Coherence of the tangential and normal signals

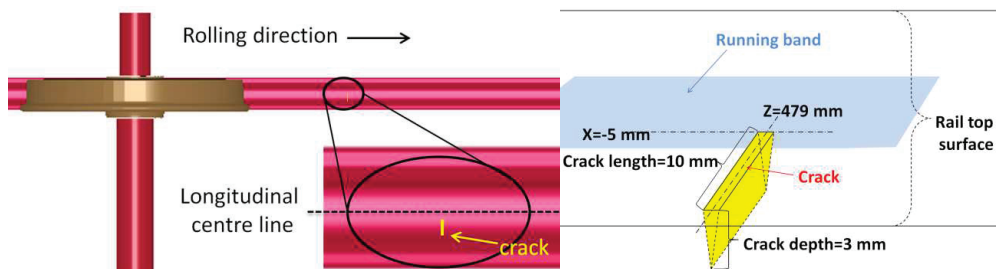


(g) Rayleigh-wave-like elliptical nodal motion

Figure. 7.7: Simulated surface nodal motion (Left, middle and right graphs are for the rail surface nodes N1, N2 and N3, respectively)

7.3. Waves generated by a crack

Rayleigh waves have been widely used for discovering the mechanical and structural properties of the object being tested, e.g., crack detection. As the proposed explicit FEM can capture Rayleigh wave phenomenon, an explicit FE wheel-rail dynamic interaction model with a crack on the rail top is presented to investigate the wave generated by the crack, which may contribute to the early-stage detection of cracks in the rail surface. The model was developed from the wheel-rail interaction model with no lateral motion of wheel (simulation case 1 presented in Chapter 5) by adding a ‘seam’ in the rail top, as shown in Fig. 7.8 (a). Fig. 7.8 (b) shows the size and accurate position of the modelled crack. A contact pair with a static COF 0.35 was defined between the crack surfaces.

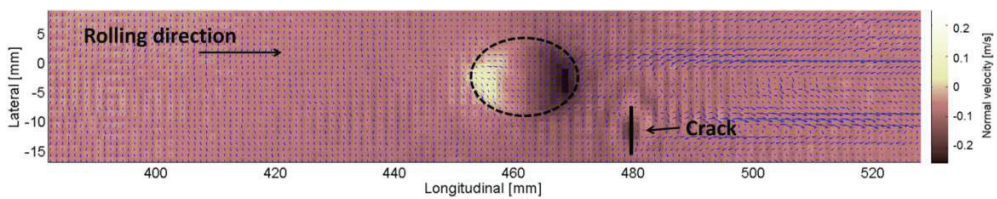


(a) Adding a ‘seam’ to the rail top

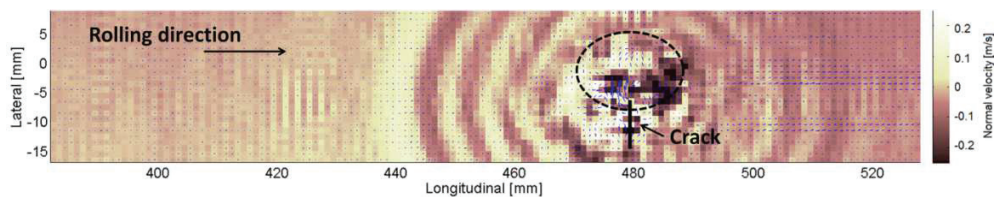
(b) The size and position of the modelled crack

Figure. 7.8: wheel-rail interaction model with a crack on the rail top surface

The contour/vector diagrams in Figs. 7.9 (a) and (b) show the distribution of the rail surface nodal velocities within the whole solution zone when the wheel was approaching and rolling over the crack in the simulation. The contact patch is indicated by the dashed black oval; the crack is denoted by the bold black line. The wave patterns observed in Fig. 7.9 were generated at the location of the crack and propagate radially. The wave generated when the wheel was rolling over the crack is more significant than the wave generated when the wheel was approaching the crack. See ("Animation for Fig. 7.9(a), <https://youtu.be/lYq0A5twj7Q>,") and ("Animation for Fig. 7.9(b), https://youtu.be/w64p_5XHjrg,") for the corresponding animations with a time step of $1 \mu\text{s}$. The characteristics of the waves generated by cracks should be investigated and experimental validation is required in future studies to develop a wave-based rail crack detection method.



(a) Wheel approaches the crack



(b) Wheel rolls over the crack

Figure. 7.9: Waves excited by the crack

7.4. Summary of the simulated waves

This chapter analysed the generation mechanisms of the waves produced by the explicit FE wheel-rail dynamic interaction models. According to the analysis, the waves were categorised as the impact-induced wave, the large-creepage-induced wave and the perturbation-induced wave. All the three types of wave are generated intrinsically by the dynamic effects of wheel-rail dynamic interactions. The dynamic effects initiating the perturbation-induced wave are less significant than those initiating the impact-induced wave or large-creepage-induced wave. The initiation location of the perturbation-induced wave may be influenced by the traction condition of a wheel model: the perturbation occurs generally at the leading edge of the contact patch during wheel braking, whereas it occurs more often at the juncture of the adhesion-slip regions during wheel traction. In addition, the frictional perturbation discovered in this study is suspected to be closely related to the dynamic friction-induced instability. Because the initiation of perturbation may be influenced by the wheel traction condition, traction and braking control strategies may be optimised based on this new insight to mitigate squeal and corrugation in the future.

This chapter also studied the characteristics of the simulated large-creepage-induced wave. The large-creepage-induced wave may be attributed to Rayleigh wave because the simulated wave is formed in rail surface nodes with retrograde elliptical motion and the simulated wave speed is in line with the speed of Rayleigh wave travelling in steel. The reproduction of the Rayleigh wave confirms that the proposed explicit FEM is appropriate and reliable for simulating wheel-rail dynamic interactions with the involvement of wave phenomena.

An explicit FE wheel-rail dynamic interaction model with a crack in the rail top was proposed in this chapter to investigate waves generated by the crack. Waves were generated at the location of the crack and propagate radially when the wheel approached and rolled over the crack in the simulation. With a further investigation of the characteristics of the waves generated by cracks and experimental validation, this study may contribute to a wave-based method for the detection of early-stage rail cracks.

8

CONCLUSIONS AND FUTURE RESEARCH

8.1. Conclusions

This study has theoretically demonstrated that the explicit finite element method (FEM) is an ideal approach for solving wheel-rail dynamic interactions by fully coupling the calculation of wheel-rail frictional rolling contact with the calculation of high-frequency structural dynamics. To facilitate other researchers to perform simulations of wheel-rail dynamic interactions with commercial explicit FEM software, systematic perceptions of the involved algorithms and modelling know-how are provided. This study has proposed an indirect validation method for wheel-rail dynamic contact solutions. The reliability of the wheel-rail dynamic interaction solutions may be confirmed by separately verifying the quasi-steady-state contact solutions against Hertz contact theory and CONTACT and validating wheel/rail structural dynamic responses with measurements. To put the method to broad use, this thesis has also proposed a procedure for establishing robust explicit finite element (FE) wheel-rail dynamic interaction models and converting outputs into solutions of wheel-rail contact and dynamic responses.

Three typical numerical examples have been presented to demonstrate the effectiveness of the method for the modelling of wheel-rail dynamic interactions.

The first numerical example presented an explicit FE wheel-insulated rail joint (IRJ) dynamic interaction model, which was validated against a comprehensive field measurement including a hammer test and a pass-by measurement. The simulated transient impact contact solutions tended to vary noticeably with the time step, indicating that dynamic effects play important roles in the wheel-IRJ impact contact. Transient positive surface shear stress, whose direction is opposite that of shear stress under ordinary tractive rolling, was discovered on the rail surface immediately after the joint. The influence of the wheel-rail contact geometry on the transient contact solutions was also investigated. The good agreement between the simulated 'footprints' of the contact patch and the in situ running band implied that the model with the measured geometry provided more realistic predictions of the transient solutions of the impact contact at the target IRJ. In addition, regular wave patterns were produced both before and during the wheel-IRJ impacts in the simulations, and these patterns reflected continuum vibrations excited by wheel-rail frictional rolling and impact contact and confirmed that the simulated transient contact solutions are reliable.

The second numerical example proposed an explicit FE wheel-rail dynamic interaction model with wheel lateral motion to investigate wheel-rail squeal-exciting contact with the involvement of dynamic effects, unsteady lateral creepage and velocity-dependent friction. The proposed model is considered to be capable of reproducing the two commonly considered mechanisms leading to squeal: falling-friction and mode-coupling. The analyses of the simulated results indicated that the explicit FE dynamic interaction model can comprehensively consider and accurately predict the wheel-rail dynamic contact and structural dynamic behaviour.

The third numerical example used an explicit FE model to simulate the non-steady-state transition of wheel-rail rolling from single-point to two-point contact. The stress and adhesion-slip distribution under the single-point contact condition and the positions and shapes of the contact patches under the two-point contact condition corresponded well with the results in the literature. Transient dynamic effects can be captured by the relative velocity in the wheel-rail contact. Wave propagation was excited in the wheel and rail continua, especially by the transition from single-point to two-point contact. The vibrations and waves may cause local

compression intensification and relaxation of the contact, as well as local perturbation of the micro-slip. Compared to those in single-point contact, stronger waves embodied in the alternation of the compression intensification and relaxation can be observed upon the occurrence of the second contact point. Moreover, the contact transition can cause the full slip of the entire wheel-rail contact. These factors could contribute to contact instability and ultimately squeal and corrugation.

This study finally analysed the generation mechanisms of the waves produced by the explicit FE wheel-rail dynamic interaction models. The waves were categorised as the impact-induced wave, the large-creepage-induced wave and the perturbation-induced wave. All three types of wave were generated intrinsically by the dynamic effects of wheel-rail interaction. The frictional perturbation discovered in this study was suspected to be closely related to the dynamic friction-induced instability. Because the initiation of perturbation may be influenced by the wheel traction condition, traction and braking control strategies may be optimised based on this new insight to mitigate squeal and corrugation in the future. The analysis of the characteristics of the simulated large-creepage-induced wave suggested that the large-creepage-induced wave can be attributed to Rayleigh wave. The reproduction of Rayleigh wave confirmed that the proposed explicit FEM is appropriate and reliable for simulating wheel-rail dynamic interactions with the involvement of wave phenomena.

8.2. Future research

Dynamic contact algorithms should further be studied and developed for more sensitive and realistic dynamic contact solutions. When employing the penalty contact algorithm implemented in the currently used general-purposed explicit FEM programs, the calculated contact stress has been proven to be less sensitive to the high-frequency dynamic effects than the calculated contact nodal vibrating velocity. This may constrain the method from accurately predicting and reproducing the ‘enigmatic’ squeal and corrugation, whose occurrences are quite sensitive to both the structural dynamic behaviour and contact condition.

The displacement boundary conditions applied to the proposed explicit FE wheel (axle) model may not be sufficient for simulating wheel curving behaviour and the rolling contact on the curve tracks. More realistic kinematic boundary conditions or a full wheelset model may be required to reliably calculate unstable wheel vibration and consequent squeal. Moreover, solid rail-pad representations with proper material parameters proposed in (Oregui *et al.*, 2015b) may be adopted in future studies of wheel-rail dynamic interactions to improve the accuracies of the lateral and longitudinal dynamics simulations. In addition, the creepage value calculated with the explicit FEM should be determined in future study and compared to those estimated using CONTACT with the same input parameters.

An explicit FEM solver dedicated to the analysis of the wheel-rail dynamic interaction may be developed in the future. On one hand, the computation cost is expected to be reduced by eliminating redundant conditional statements in the general-purposed explicit FE commercial programs; on the other hand, a newly developed solver may provide more convenience and flexibility to future amendments to the algorithm: the penalty contact algorithm with nonlinear or functional penalty contact stiffness, more sensitive dynamic contact algorithms, and the coupling with multi-body dynamics analyses may be implemented for future analyses of wheel-rail dynamic interactions.

The investigation of waves caused by wheel-rail dynamic interactions will continue, including the generation mechanism of the perturbation and its correspondence to the

traction/braking condition. Experimental validation of the waves simulated by the proposed explicit FE models should be conducted. In addition, waves have been found to be generated at a crack and to propagate radially when the wheel approaches and rolls over the crack in the simulation. With further investigation of the characteristics of the waves generated by cracks and experimental validation, a wave-based method for the detection of early-stage rail cracks may be developed in the future.

REFERENCES

- Anderson, D., & Wheatley, N. (2008). Mitigation of wheel squeal and flanging noise on the Australian rail network. *Noise and Vibration Mitigation for Rail Transportation Systems*, 99, 399-405. doi:10.1007/978-3-540-74893-9_56
- Attaway, S. W., Hendrickson, B. A., Plimpton, S. J., Gardner, D. R., Vaughan, C. T., Brown, K. H., & Heinstein, M. W. (1998). A parallel contact detection algorithm for transient solid dynamics simulations using PRONTO3D. *Computational Mechanics*, 22(2), 143-159. doi:10.1007/s004660050348
- Ayasse, J. B., & Chollet, H. (2006). Determination of the wheel rail contact patch in semi-Hertzian conditions. *Vehicle System Dynamics*, 43(3), 161-172. doi:10.1080/00423110412331327193
- Bathe, K. J. (1996). *Finite Element Procedures*: Prentice Hall.
- Burgelman, N., Li, Z., & Dollevoet, R. (2014). A new rolling contact method applied to conformal contact and the train–turnout interaction. *Wear*, 321, 94-105. doi:10.1016/j.wear.2014.10.008
- Cai, W., Wen, Z. F., Jin, X. S., & Zhai, W. M. (2007). Dynamic stress analysis of rail joint with height difference defect using finite element method. *Engineering Failure Analysis*, 14(8), 1488-1499. doi:10.1016/j.engfailanal.2007.01.007
- Carter, F. W. (1926). On the action of a locomotive driving wheel. *Proceedings of the Royal Society of London Series a-Containing Papers of a Mathematical and Physical Character*, 112(760), 151-157. doi:10.1098/rspa.1926.0100
- Chen, G. X., Zhou, Z. R., Ouyang, H., Jin, X. S., Zhu, M. H., & Liu, Q. Y. (2010). A finite element study on rail corrugation based on saturated creep force-induced self-excited vibration of a wheelset–track system. *Journal of Sound and Vibration*, 329(22), 4643-4655. doi:10.1016/j.jsv.2010.05.011
- Chen, Y. C., & Kuang, J. H. (2002). Contact stress variations near the insulated rail joints. *Proceedings of the Institution of Mechanical Engineers, Part F: Journal of Rail and Rapid Transit*, 216(4), 265-273. doi:10.1243/095440902321029217
- Chen, Y. C., & Chen, L. W. (2006). Effects of insulated rail joint on the wheel/rail contact stresses under the condition of partial slip. *Wear*, 260(11-12), 1267-1273. doi:10.1016/j.wear.2005.08.005

- Chiello, O., Ayasse, J. B., Vincent, N., & Koch, J. R. (2006). Curve squeal of urban rolling stock—Part 3: Theoretical model. *Journal of Sound and Vibration*, 293(3-5), 710-727. doi:10.1016/j.jsv.2005.12.010
- Chongyi, C., Chengguo, W., & Ying, J. (2010). Study on numerical method to predict wheel/rail profile evolution due to wear. *Wear*, 269(3-4), 167-173. doi:10.1016/j.wear.2009.12.031
- Courant, R., Friedrichs, K., & Lewy, H. (1967). On the Partial Difference Equations of Mathematical Physics. *IBM Journal of Research and Development*, 11(2), 215-234. doi:10.1147/rd.112.0215
- Damme, S., Nackenhorst, U., Wetzel, A., & Zastrau, B. W. (2003). On the numerical analysis of the wheel-rail system in rolling contact. *System Dynamic and Long-Term Behaviour of Railway Vehicles, Track and Subgrade*, 6, 155-174.
- de Beer, F. G., Janssens, M. H. A., & Kooijman, P. P. (2003). Squeal noise of rail-bound vehicles influenced by lateral contact position. *Journal of Sound and Vibration*, 267(3), 497-507. doi:10.1016/s0022-460x(03)00710-7
- De Man, A. P. (2002). *Dynatrack: A survey of dynamic railway track properties and their quality*. (Ph.D. doctoral thesis), TU Delft.
- Deng, X., Qian, Z., & Dollevoet, R. (2015). Lagrangian Explicit Finite Element Modeling for Spin-Rolling Contact. *Journal of Tribology*, 137(4), 041401. doi:10.1115/1.4030709
- Eadie, D. T., Santoro, M., & Powell, W. (2003). Local control of noise and vibration with KELTRACK™ friction modifier and Protector® trackside application: an integrated solution. *Journal of Sound and Vibration*, 267(3), 761-772. doi:10.1016/s0022-460x(03)00739-9
- Eadie, D. T., Santoro, M., & Kalousek, J. (2005). Railway noise and the effect of top of rail liquid friction modifiers: changes in sound and vibration spectral distributions in curves. *Wear*, 258(7-8), 1148-1155. doi:10.1016/j.wear.2004.03.061
- Ekberg, A., & Sandström, J. (2009). Numerical study of the mechanical deterioration of insulated rail joints. *Proceedings of the Institution of Mechanical Engineers, Part F: Journal of Rail and Rapid Transit*, 223(3), 265-273. doi:10.1243/09544097jrrt243
- Fingberg, U. (1990). A model of wheel-rail squealing noise. *Journal of Sound and Vibration*, 143(3), 365-377. doi:10.1016/0022-460x(90)90729-j
- Flanagan, D. P., & Belytschko, T. (1981). A uniform strain hexahedron and quadrilateral with orthogonal hourglass control. *International Journal for Numerical Methods in Engineering*, 17(5), 679-706. doi:10.1002/nme.1620170504

- Glocker, C., Cataldi-Spinola, E., & Leine, R. I. (2009). Curve squealing of trains: Measurement, modelling and simulation. *Journal of Sound and Vibration*, 324(1-2), 365-386. doi:10.1016/j.jsv.2009.01.048
- Graf, M., & Ostermeyer, G. P. (2015). Friction-induced vibration and dynamic friction laws: Instability at positive friction-velocity-characteristic. *Tribology International*, 92, 255-258. doi:10.1016/j.triboint.2015.06.019
- Grassie, S. L., Gregory, R. W., Harrison, D., & Johnson, K. L. (1982). The Dynamic-Response of Railway Track to High-Frequency Vertical Excitation. *Journal of Mechanical Engineering Science*, 24(2), 77-90. doi:10.1243/jmes_jour_1982_024_018_02
- Grassie, S. L. (2009). Rail corrugation: Characteristics, causes, and treatments. *Proceedings of the Institution of Mechanical Engineers, Part F: Journal of Rail and Rapid Transit*, 223(6), 581-596. doi:10.1243/09544097jrrt264
- Hallquist, J. O., Goudreau, G. L., & Benson, D. J. (1985). Sliding Interfaces with Contact-Impact in Large-Scale Lagrangian Computations. *Computer Methods in Applied Mechanics and Engineering*, 51(1-3), 107-137. doi:10.1016/0045-7825(85)90030-1
- Hallquist, J. O. (2006). *LS-DYNA Theory Manual*.
- He, C. G., Huang, Y. B., Ma, L., Guo, J., Wang, W. J., Liu, Q. Y., & Zhu, M. H. (2015). Experimental investigation on the effect of tangential force on wear and rolling contact fatigue behaviors of wheel material. *Tribology International*, 92, 307-316. doi:10.1016/j.triboint.2015.07.012
- Heckl, M. A., & Abrahams, I. D. (2000). Curve Squeal of Train Wheels, Part 1: Mathematical Model for Its Generation. *Journal of Sound and Vibration*, 229(3), 669-693. doi:10.1006/jsvi.1999.2510
- Hertz, H. (1882). Ueber die Berührung fester elastischer Körper. *Journal für die reine und angewandte Mathematik (Crelle's Journal)*, 1882(92). doi:10.1515/crll.1882.92.156
- Hibbitt, K., & Sorensen. (2001). *ABAQUS/Explicit: User's Manual: Hibbitt, Karlsson and Sorenson Incorporated*.
- Himebaugh, A. K., Plaut, R. H., & Dillard, D. A. (2008). Finite element analysis of bonded insulated rail joints. *International Journal of Adhesion and Adhesives*, 28(3), 142-150. doi:10.1016/j.ijadhadh.2007.09.003
- Hu, G., & Wriggers, P. (2002). On the adaptive finite element method of steady-state rolling contact for hyperelasticity in finite deformations. *Computer Methods in Applied Mechanics and Engineering*, 191(13-14), 1333-1348. doi:10.1016/s0045-7825(01)00326-7
- Huang, Z. Y. (2007). *Theoretical modelling of railway curve squeal*. University of Southampton.

- Huang, Z. Y., Thompson, D. J., & Jones, C. J. C. (2008). Squeal prediction for a bogied vehicle in a curve. *Noise and Vibration Mitigation for Rail Transportation Systems*, 99, 313-319. doi:10.1007/978-3-540-74893-9_44
- Hughes, T. J. R., Taylor, R. L., Sackman, J. L., Curnier, A., & Kanoknukulchai, W. (1976). A finite element method for a class of contact-impact problems. *Computer Methods in Applied Mechanics and Engineering*, 8(3), 249-276. doi:10.1016/0045-7825(76)90018-9
- Hughes, T. J. R., & Liu, W. K. (1981). Nonlinear finite element analysis of shells-part II. two-dimensional shells. *Computer Methods in Applied Mechanics and Engineering*, 27(2), 167-181. doi:10.1016/0045-7825(81)90148-1
- Iwnicki, S., Thompson, D., Berg, M., Cole, C. (Ed.), Boronenko, Y., Andersson, E., Iwnicki, S., Wickens, A., Lewis, R., Orlova, A., Chollet, H., Olofsson, D., Dahlberg, T., Johnson, D., Goodall, R., Stow, J., Allen, P., Jones, C., Wu, H., Mei, T., Polach, O., Wilson, N. (2006). *Handbook of Railway Vehicle Dynamics*: Boca Raton: CRC Press.
- Jiang, J., Anderson, D. C., & Dwight, R. (2015). The Mechanisms of Curve Squeal. *Noise and Vibration Mitigation for Rail Transportation Systems*, 126, 587-594. doi:10.1007/978-3-662-44832-8_69
- Johansson, A., Pålsson, B., Ekh, M., Nielsen, J. C. O., Ander, M. K. A., Brouzoulis, J., & Kassa, E. (2011). Simulation of wheel-rail contact and damage in switches & crossings. *Wear*, 271(1-2), 472-481. doi:10.1016/j.wear.2010.10.014
- Johnson, K. L. (1985). *Contact Mechanics*: Cambridge university press.
- Jones, C. J. C., Thompson, D. J., & Diehl, R. J. (2006). The use of decay rates to analyse the performance of railway track in rolling noise generation. *Journal of Sound and Vibration*, 293(3-5), 485-495. doi:10.1016/j.jsv.2005.08.060
- Kabo, E., Nielsen, J. C. O., & Ekberg, A. (2006). Prediction of dynamic train-track interaction and subsequent material deterioration in the presence of insulated rail joints. *Vehicle System Dynamics*, 44, 718-729. doi:10.1080/00423110600885715
- Kalker, J. J. (1990). *Three-Dimensional Elastic Bodies in Rolling Contact*: Springer Netherlands.
- Kalker, J. J., & Johnson, K. L. (1993). Three-Dimensional Elastic Bodies in Rolling Contact. *Journal of applied Mechanics*, 60(1), 255. doi:10.1115/1.2900773
- Kerr, A. D., & Cox, J. E. (1999). Analysis and tests of bonded insulated rail joints subjected to vertical wheel loads. *International Journal of Mechanical Sciences*, 41(10), 1253-1272. doi:10.1016/S0020-7403(98)00042-3

- Kitagawa, T., Murata, K., Kawaguchi, T., Tanaka, S., & Nagakura, K. (2015). Experimental and Theoretical Studies on Impact Noise Generation due to Rail Joints. *Noise and Vibration Mitigation for Rail Transportation Systems*, 126, 55-62. doi:10.1007/978-3-662-44832-8_8
- Knothe, K., Wille, R., & Zastra, B. W. (2001). Advanced Contact Mechanics–Road and Rail. *Vehicle System Dynamics*, 35(4-5), 361-407. doi:10.1076/vesd.35.4.361.2043
- Li, Z. (2002). Wheel-rail rolling contact and its application to wear simulation. Delft University of Technology.
- Li, Z. L., Zhao, X., Dollevoet, R., & Molodova, M. (2008). Differential wear and plastic deformation as causes of squat at track local stiffness change combined with other track short defects. *Vehicle System Dynamics*, 46, 237-246. doi:10.1080/00423110801935855
- Lundén, R., & Paulsson, B. (2009). 1 - Introduction to wheel–rail interface research *Wheel–Rail Interface Handbook* (pp. 3-33): Woodhead Publishing.
- Magheri, S., Malvezzi, M., Meli, E., & Rindi, A. (2011). An innovative wheel–rail contact model for multibody applications. *Wear*, 271(1-2), 462-471. doi:10.1016/j.wear.2010.10.038
- Maia, N., & Silva, J. (1998). *Theoretical and Experimental Modal Analysis*. England: Research Studies Press LTD.
- Mandal, N. K., & Dhanasekar, M. (2013). Sub-modelling for the ratchetting failure of insulated rail joints. *International Journal of Mechanical Sciences*, 75, 110-122. doi:10.1016/j.ijmecsci.2013.06.003
- Mandal, N. K. (2016). Finite element analysis of the mechanical behaviour of insulated rail joints due to impact loadings. *Proceedings of the Institution of Mechanical Engineers Part F-Journal of Rail and Rapid Transit*, 230(3), 759-773. doi:10.1177/0954409714561708
- Mandal, N. K., Dhanasekar, M., & Sun, Y. Q. (2016). Impact forces at dipped rail joints. *Proceedings of the Institution of Mechanical Engineers Part F-Journal of Rail and Rapid Transit*, 230(1), 271-282. doi:10.1177/0954409714537816
- Meli, E., Magheri, S., & Malvezzi, M. (2011). Development and implementation of a differential elastic wheel–rail contact model for multibody applications. *Vehicle System Dynamics*, 49(6), 969-1001. doi:10.1080/00423114.2010.504854
- Mijar, A. R., & Arora, J. S. (2004). An augmented Lagrangian optimization method for contact analysis problems, 1: formulation and algorithm. *Structural and Multidisciplinary Optimization*, 28(2-3). doi:10.1007/s00158-004-0423-y
- Mindlin, R. D. (1949). Compliance of elastic bodies in contact. *Journal of applied Mechanics*(16), 259-268.

- Molodova, M., Li, Z. L., & Dollevoet, R. (2011). Axle box acceleration: Measurement and simulation for detection of short track defects. *Wear*, 271(1-2), 349-356. doi:10.1016/j.wear.2010.10.003
- Molodova, M. (2013). Detection of early squats by axle box acceleration. Delft University of Technology.
- Molodova, M., Li, Z. L., Nunez, A., & Dollevoet, R. (2014). Validation of a finite element model for axle box acceleration at squats in the high frequency range. *Computers & Structures*, 141, 84-93. doi:10.1016/j.compstruc.2014.05.005
- Mulvihill, D. M., Kartal, M. E., Nowell, D., & Hills, D. A. (2011). An elastic-plastic asperity interaction model for sliding friction. *Tribology International*, 44(12), 1679-1694. doi:10.1016/j.triboint.2011.06.018
- Nackenhorst, U. (2004). The ALE-formulation of bodies in rolling contact. *Computer Methods in Applied Mechanics and Engineering*, 193(39-41), 4299-4322. doi:10.1016/j.cma.2004.01.033
- Noh, G., & Bathe, K.-J. (2013). An explicit time integration scheme for the analysis of wave propagations. *Computers & Structures*, 129, 178-193. doi:10.1016/j.compstruc.2013.06.007
- Oden, J. T., & Pires, E. B. (1984). Algorithms and numerical results for finite element approximations of contact problems with non-classical friction laws. *Computers & Structures*, 19(1-2), 137-147. doi:10.1016/0045-7949(84)90212-8
- Oregui, M., Li, Z., & Dollevoet, R. (2015a). Identification of characteristic frequencies of damaged railway tracks using field hammer test measurements. *Mechanical Systems and Signal Processing*, 54-55, 224-242. doi:10.1016/j.ymsp.2014.08.024
- Oregui, M., Li, Z., & Dollevoet, R. (2015b). An investigation into the modeling of railway fastening. *International Journal of Mechanical Sciences*, 92, 1-11. doi:10.1016/j.ijmecsci.2014.11.019
- Oregui, M., Molodova, M., Nunez, A., Dollevoet, R., & Li, Z. (2015c). Experimental Investigation Into the Condition of Insulated Rail Joints by Impact Excitation. *Experimental Mechanics*, 55(9), 1597-1612. doi:10.1007/s11340-015-0048-7
- Oregui, M., Li, Z. L., & Dollevoet, R. (2016). An investigation into the vertical dynamics of tracks with monoblock sleepers with a 3D finite-element model. *Proceedings of the Institution of Mechanical Engineers Part F-Journal of Rail and Rapid Transit*, 230(3), 891-908. doi:10.1177/0954409715569558
- Ouyang, H., Nack, W., Yuan, Y., & Chen, F. (2005). Numerical analysis of automotive disc brake squeal: a review. *International Journal of Vehicle Noise and Vibration*, 1(3/4), 207. doi:10.1504/ijvnr.2005.007524

- Périard, F. J. (1998). *Wheel-Rail Noise Generation: Curve Squealing by Trams*. Delft University of Technology.
- Pieringer, A. (2014). A numerical investigation of curve squeal in the case of constant wheel/rail friction. *Journal of Sound and Vibration*, 333(18), 4295-4313. doi:10.1016/j.jsv.2014.04.024
- Piotrowski, J., & Kik, W. (2008). A simplified model of wheel/rail contact mechanics for non-Hertzian problems and its application in rail vehicle dynamic simulations. *Vehicle System Dynamics*, 46(1-2), 27-48. doi:10.1080/00423110701586444
- Pletz, M., Daves, W., & Ossberger, H. (2012a). A wheel passing a crossing nose: Dynamic analysis under high axle loads using finite element modelling. *Proceedings of the Institution of Mechanical Engineers, Part F: Journal of Rail and Rapid Transit*, 226(6), 603-611. doi:10.1177/0954409712448038
- Pletz, M., Daves, W., & Ossberger, H. (2012b). A wheel set/crossing model regarding impact, sliding and deformation-Explicit finite element approach. *Wear*, 294, 446-456. doi:10.1016/j.wear.2012.07.033
- Poritsky, H. (1950). Stresses and deflections of cylindrical bodies in contact with application to contact of gears and of locomotive wheels. *Journal of Applied Mechanics-Transactions of the ASME*, 17(2), 191-201.
- Railway applications - Noise emission - Characterisation of the dynamic properties of track sections for pass by noise measurements. (2010). EN 15461:2008+A1:2010(E) (Vol. EN 15461:2008+A1:2010(E)).
- Remington, P. J. (1987). Wheel/rail squeal and impact noise: What do we know? What don't we know? Where do we go from here? *Journal of Sound and Vibration*, 116(2), 339-353. doi:10.1016/s0022-460x(87)81306-8
- Ringsberg, J. (2003). Rolling contact fatigue analysis of rails including numerical simulations of the rail manufacturing process and repeated wheel-rail contact loads. *International Journal of Fatigue*, 25(6), 547-558. doi:10.1016/s0142-1123(02)00147-0
- Ringsber, J. W., & Josefson, B. L. (2005). Finite element analyses of rolling contact fatigue crack initiation in railheads. *Proceedings of the Institution of Mechanical Engineers, Part F: Journal of Rail and Rapid Transit*, 215(4), 243-259. doi:10.1243/0954409011531558
- Rudd, M. J. (1976). Wheel/rail noise—Part II: Wheel squeal. *Journal of Sound and Vibration*, 46(3), 381-394. doi:10.1016/0022-460x(76)90862-2
- Sandstrom, J., & Ekberg, A. (2009). Numerical study of the mechanical deterioration of insulated rail joints. *Proceedings of the Institution of Mechanical Engineers Part F-Journal of Rail and Rapid Transit*, 223(3), 265-273. doi:10.1243/09544097jrrt243

- Sarl, M. (2005). *Radioss Theory Manual*: Mecalog Sarl.
- Sh. Sichani, M., Enblom, R., & Berg, M. (2014). A novel method to model wheel–rail normal contact in vehicle dynamics simulation. *Vehicle System Dynamics*, 52(12), 1752-1764. doi:10.1080/00423114.2014.961932
- Sh. Sichani, M., Enblom, R., & Berg, M. (2016). An alternative to FASTSIM for tangential solution of the wheel–rail contact. *Vehicle System Dynamics*, 54(6), 748-764. doi:10.1080/00423114.2016.1156135
- Sladkowski, A., & Sitarz, M. (2005). Analysis of wheel–rail interaction using FE software. *Wear*, 258(7-8), 1217-1223. doi:10.1016/j.wear.2004.03.032
- Squicciarini, G., Usberti, S., Thompson, D. J., Corradi, R., & Barbera, A. (2015). Curve Squeal in the Presence of Two Wheel/Rail Contact Points. *Noise and Vibration Mitigation for Rail Transportation Systems*, 126, 603-610. doi:10.1007/978-3-662-44832-8_71
- Sundh, J., & Olofsson, U. (2008). Seizure mechanisms of wheel–rail contacts under lubricated conditions using a transient ball-on-disc test method. *Tribology International*, 41(9-10), 867-874. doi:10.1016/j.triboint.2007.12.011
- Telford, W. M., Geldart, L. P., & Sheriff, R. E. (1990). *Applied Geophysics*: Cambridge University Press.
- Telliskivi, T., & Olofsson, U. (2004). Wheel–rail wear simulation. *Wear*, 257(11), 1145-1153. doi:10.1016/j.wear.2004.07.017
- Thompson, D. J., & Vincent, N. (1995). Track Dynamic Behaviour at High Frequencies. Part 1: Theoretical Models and Laboratory Measurements. *Vehicle System Dynamics*, 24(sup1), 86-99. doi:10.1080/00423119508969617
- Thompson, D. J. (2009). *Railway Noise and Vibration : Mechanisms, Modelling and Means of Control*: Elsevier.
- Vermeulen, P. J., & Johnson, K. L. (1964). Contact of Nonspherical Elastic Bodies Transmitting Tangential Forces. *Journal of applied Mechanics*, 31(2), 338. doi:10.1115/1.3629610
- Vincent, N., & Thompson, D. J. (1995). Track Dynamic Behaviour at High Frequencies. Part 2: Experimental Results and Comparisons with Theory. *Vehicle System Dynamics*, 24(sup1), 100-114. doi:10.1080/00423119508969618
- Vincent, N., Koch, J. R., Chollet, H., & Guerder, J. Y. (2006). Curve squeal of urban rolling stock—Part 1: State of the art and field measurements. *Journal of Sound and Vibration*, 293(3-5), 691-700. doi:10.1016/j.jsv.2005.12.008

- Vo, K. D., Tieu, A. K., Zhu, H. T., & Kosasih, P. B. (2014). A 3D dynamic model to investigate wheel–rail contact under high and low adhesion. *International Journal of Mechanical Sciences*, 85, 63-75. doi:10.1016/j.ijmecsci.2014.05.007
- Vo, K. D., Zhu, H. T., Tieu, A. K., & Kosasih, P. B. (2015). FE method to predict damage formation on curved track for various worn status of wheel/rail profiles. *Wear*, 322-323, 61-75. doi:10.1016/j.wear.2014.10.015
- Wei, Z. L., Li, Z. L., Qian, Z. W., Chen, R., & Dollevoet, R. (2016). 3D FE modelling and validation of frictional contact with partial slip in compression-shift-rolling evolution. *International Journal of Rail Transportation*, 4(1), 20-36. doi:10.1080/23248378.2015.1094753
- Wei, Z., Nunez, A., Li, Z., & Dollevoet, R. (2017a). Evaluating Degradation at Railway Crossings Using Axle Box Acceleration Measurements. *Sensors (Basel)*, 17(10). doi:10.3390/s17102236
- Wei, Z., Shen, C., Li, Z., & Dollevoet, R. (2017b). Wheel–Rail Impact at Crossings: Relating Dynamic Frictional Contact to Degradation. *Journal of Computational and Nonlinear Dynamics*, 12(4), 041016. doi:10.1115/1.4035823
- Wen, Z. F., Jin, X. S., & Zhang, W. H. (2005). Contact-impact stress analysis of rail joint region using the dynamic finite element method. *Wear*, 258(7-8), 1301-1309. doi:10.1016/j.wear.2004.03.040
- Wiest, M., Daves, W., Fischer, F. D., & Ossberger, H. (2008a). Deformation and damage of a crossing nose due to wheel passages. *Wear*, 265(9-10), 1431-1438. doi:10.1016/j.wear.2008.01.033
- Wiest, M., Kassa, E., Daves, W., Nielsen, J. C. O., & Ossberger, H. (2008b). Assessment of methods for calculating contact pressure in wheel-rail/switch contact. *Wear*, 265(9-10), 1439-1445. doi:10.1016/j.wear.2008.02.039
- Wriggers, P. (2006). *Computational Contact Mechanics*: Springer Berlin Heidelberg.
- Wu, S. R. (2003). A priori error estimates for explicit finite element for linear elasto-dynamics by Galerkin method and central difference method. *Computer Methods in Applied Mechanics and Engineering*, 192(51-52), 5329-5353. doi:10.1016/j.cma.2003.08.002
- Wu, S. R. (2006). Lumped mass matrix in explicit finite element method for transient dynamics of elasticity. *Computer Methods in Applied Mechanics and Engineering*, 195(44-47), 5983-5994. doi:10.1016/j.cma.2005.10.008
- Wu, S. R. (2009). A variational principle for dynamic contact with large deformation. *Computer Methods in Applied Mechanics and Engineering*, 198(21-26), 2009-2015. doi:10.1016/j.cma.2008.12.013

- Wu, S. R., & Gu, L. (2012). *Introduction to the Explicit Finite Element Method for Nonlinear Transient Dynamics*. Somerset, UNITED STATES: John Wiley & Sons, Incorporated.
- Wu, T. X., & Thompson, D. J. (2002). A Hybrid Model for the Noise Generation Due to Railway Wheel Flats. *Journal of Sound and Vibration*, 251(1), 115-139. doi:10.1006/jsvi.2001.3980
- Wu, T. X., & Thompson, D. J. (2003). On the impact noise generation due to a wheel passing over rail joints. *Journal of Sound and Vibration*, 267(3), 485-496. doi:10.1016/S0022-460x(03)00709-0
- Xin, L., Markine, V. L., & Shevtsov, I. Y. (2016). Numerical procedure for fatigue life prediction for railway turnout crossings using explicit finite element approach. *Wear*, 366-367, 167-179. doi:10.1016/j.wear.2016.04.016
- Yan, W., & Fischer, F. D. (2000). Applicability of the Hertz contact theory to rail-wheel contact problems. *Archive of Applied Mechanics (Ingenieur Archiv)*, 70(4), 255-268. doi:10.1007/s004199900035
- Yang, J. N., & Thompson, D. J. (2014). Time-domain prediction of impact noise from wheel flats based on measured profiles. *Journal of Sound and Vibration*, 333(17), 3981-3995. doi:10.1016/j.jsv.2014.04.026
- Yang, Z., Li, Z., & Dollevoet, R. P. B. J. (2015). An Explicit Integration Finite Element Method for Impact Noise Generation at a Squat. *Noise and Vibration Mitigation for Rail Transportation Systems*, 126, 63-70. doi:10.1007/978-3-662-44832-8_9
- Yang, Z., Li, Z. L., & Dollevoet, R. (2016). Modelling of non-steady-state transition from single-point to two-point rolling contact. *Tribology International*, 101, 152-163. doi:10.1016/j.triboint.2016.04.023
- Yang, Z., Boogaard, A., Chen, R., Dollevoet, R., & Li, Z. (2018). Numerical and experimental study of wheel-rail impact vibration and noise generated at an insulated rail joint. *International Journal of Impact Engineering*, 113, 29-39. doi:10.1016/j.ijimpeng.2017.11.008
- Zenzerovic, I., Kropp, W., & Pieringer, A. (2016). An engineering time-domain model for curve squeal: Tangential point-contact model and Green's functions approach. *Journal of Sound and Vibration*, 376, 149-165. doi:10.1016/j.jsv.2016.04.037
- Zerbst, U., Lundén, R., Edel, K. O., & Smith, R. A. (2009). Introduction to the damage tolerance behaviour of railway rails – a review. *Engineering Fracture Mechanics*, 76(17), 2563-2601. doi:10.1016/j.engfracmech.2009.09.003
- Zhao, X., & Li, Z. L. (2011). The solution of frictional wheel-rail rolling contact with a 3D transient finite element model: Validation and error analysis. *Wear*, 271(1-2), 444-452. doi:10.1016/j.wear.2010.10.007

- Zhao, X., Li, Z., & Liu, J. (2012). Wheel-rail impact and the dynamic forces at discrete supports of rails in the presence of singular rail surface defects. *Proceedings of the Institution of Mechanical Engineers Part F-Journal of Rail and Rapid Transit*, 226(F2), 124-139. doi:10.1177/0954409711413975
- Zhao, X., Li, Z., & Dollevoet, R. (2014a). Influence of the Fastening Modeling on the Vehicle-Track Interaction at Singular Rail Surface Defects. *Journal of Computational and Nonlinear Dynamics*, 9(3), 031002. doi:10.1115/1.4025895
- Zhao, X., Wen, Z., Zhu, M., & Jin, X. (2014b). A study on high-speed rolling contact between a wheel and a contaminated rail. *Vehicle System Dynamics*, 52(10), 1270-1287. doi:10.1080/00423114.2014.934845
- Zhao, X., & Li, Z. L. (2015). A three-dimensional finite element solution of frictional wheel-rail rolling contact in elasto-plasticity. *Proceedings of the Institution of Mechanical Engineers Part J-Journal of Engineering Tribology*, 229(1), 86-100. doi:10.1177/1350650114543717
- Zhao, X., & Li, Z. (2016). A solution of transient rolling contact with velocity dependent friction by the explicit finite element method. *Engineering Computations*, 33(4), 1033-1050. doi:10.1108/ec-09-2014-0180
- Zhao, X., Zhao, X., Liu, C., Wen, Z., & Jin, X. (2016). A study on dynamic stress intensity factors of rail cracks at high speeds by a 3D explicit finite element model of rolling contact. *Wear*. doi:10.1016/j.wear.2016.06.001
- Zong, N., & Dhanasekar, M. (2013). Minimization of railhead edge stresses through shape optimization. *Engineering Optimization*, 45(9), 1043-1060. doi:10.1080/0305215x.2012.717075
- Zong, N., & Dhanasekar, M. (2014). Experimental studies on the performance of rail joints with modified wheel/railhead contact. *Proceedings of the Institution of Mechanical Engineers Part F-Journal of Rail and Rapid Transit*, 228(8), 857-877. doi:10.1177/0954409713496764
- Zong, N., & Dhanasekar, M. (2017). Sleeper embedded insulated rail joints for minimising the number of modes of failure. *Engineering Failure Analysis*, 76, 27-43. doi:10.1016/j.engfailanal.2017.02.001

List of animation links:

Animation for Fig. 4.25, <https://youtu.be/tWyWKw9XxRI>.

Animation for Fig. 4.27, <https://youtu.be/fAg99j6kquI>.

Animation for Fig. 4.28, <https://youtu.be/eHh24SnWDFQ>.

Animation for Fig. 5.5, <https://youtu.be/3jeei3NTP84>.

Animation for Fig. 7.1 (b), <https://youtu.be/KKSV7A1tCD0>.

Animation for Fig. 7.2(a), <https://youtu.be/yRD9EDasMmU>.

Animation for Fig. 7.2(b), <https://youtu.be/tQwWTc-GfHw>.

Animation for Fig. 7.3 (a), <https://youtu.be/BqFapqG8D-Q>.

Animation for Fig. 7.3 (b), <https://youtu.be/CE1rB0N-IVk>.

Animation for Fig. 7.4 (a), <https://youtu.be/nC4szzxeJQw>.

Animation for Fig. 7.4 (b), https://youtu.be/1vb_xsv5jvI.

Animation for Fig. 7.5, <https://youtu.be/jTbWh-FGxPc>.

Animation for Fig. 7.7, <https://youtu.be/XWyuY70mKl4>.

Animation for Fig. 7.9(a), <https://youtu.be/IYq0A5twj7Q>.

Animation for Fig. 7.9(b), https://youtu.be/w64p_5XHjrg.

ACKNOWLEDGEMENTS (致谢)

3rd September 2012 is a memorable date. Watched by my parents and girlfriend Lin, I entered the departure hall of Beijing international airport. The flight was heading to the Netherlands, a strange country where I was going to live for years for PhD study

The first meeting with Prof. Zili Li took place on the next day after I arrived at Delft. After deciding the direction of my PhD research, a weekly meeting was scheduled, which consequently adapted me to the PhD study quickly. The next period of frequent meetings with Prof. Li occurred when my draft thesis had been put on the table between us. ‘These problems may be ignored if your aim is to be an ordinary researcher’. During that period, I think over your comments about my thesis on the way home, in the kitchen, during the shower and in the dream. Your careful and critical attitude to research influenced me greatly in my PhD study, and will be a fortune to my future career.

Prof. Dollevoet is a funny, easy-going and smart boss. Your jokes make our discussions interesting and impressive; your kindness let me feel homely to live in a foreign country; your wisdom is driving our group to progress in a high speed line.

Dr. Zhiwei Qian can somehow narrate any scientific theory, method, principle or daily triviality with impeccable logic and thus comprehensible. I can indeed perceive an increase in knowledge and a decrease in time after talking with you. What I have learned from you is not only good thinking of research but also a relaxed attitude to the life: ‘those do not matter!’ I expect this will matter me in the long run.

Researchers understand the importance of experimental validation to a model. The most important measurement of my PhD study was performed with the great assistance of Anthonie Boogaard. In contrast, our fruitful discussions, sending me to hospital for emergency treatment and translating the abstract of this thesis into Dutch are not worth mentioning.

One advantage of working in a new place is to harvest more colleagues and friends. Jacqueline Barnhoorn seems to be always ready to solve any administrative difficulty that we may occur in the work and daily life. Many thanks also to Valeri Markine, Michael Steenbergen, Maria Molodova, Xiangyun Deng, Shaoguang Li, Chang Wan, Maider Oregui, Nico Burgelman, Haoyu Wang, Lizuo Xin, Zilong Wei, Siamak Hajizadeh, Yuewei Ma, Xiangming Liu, Siamand Rahimi, Meysam Naeimi, Chen Shen, Ali Jamshidi, Omid Hajizad, Ling Chang, Jan Moraal, Greg Lambert, Ivan Shevtsov, Dirk Doedens, Jurjen Hendriks, Joris van Dijk, Harm Visser, Evert van Veldhuizen, Ruud van Bezooijen, Aad van der Linden, and our Chinese

visiting scholars: Yu Zhou, Pingrui Zhao, Rong Chen, Hongqin Liang, Qian Xiao, Xiaoping Wu, Xianmai Chen, Xiubo Liu. Your scientific knowledge and engineering experience have provided valuable insights into my PhD research. I would also like to express my appreciation to Prof. Songliang Lian and Prof. Junjie Fan. It has been nine years since you introduced me to the railway research field.

Homesickness is inevitable to live alone in a foreign country, especially in early stages. Thanks to my ‘Zusterlaan friends’: Ming Li, Jinhua Wang, Feifei Wang, Jingyu Zhang, Xueming Li and Xiaowei Ouyang. You made the beginning of my PhD life in Delft colourful. May our friendships go for good!

As a loyal board-game player, special thanks to my board-game partners in Delft: Xiangming Liu, Xin Tian, Zhiwei Qian, Yufei Yuan, Jiangxiong Wei, Mo Zhang, Xiangyun Deng, Rong Chen, Pan Zhang, Yuguang Yang. For games there are winners and losers; for friendships you are all winners.

Studying, working and playing board games may not fill up an eventful PhD Life. I would also express gratitude to my friends in the other aspects. I cannot list you all, but these names occur to me at this moment: Yaqing Shu & Lan Song & Yufeng & Yuyao, Qu Hu & Xiao Liang, Yuling Li & Michael Weymeis, Xiaochen Liu, Xin Li, Tao Lv, Chenjie Yu, Meng Wang & Yanyan Sun & Kaka & Alice, Xavi Bellsolà & Montse Torras, Yusen Chen, Bin Hu, Ye Zhang, Yang Qu, Silvia Varotto, Paul van Gent,

My ‘girlfriend Lin’ mentioned in the beginning became my wife two years ago, and is about to become the mother of our daughter within five months. My gratitude to you is beyond words. But still, thank you for following me from Beijing to Shanghai, from China to Netherlands. What I will return is to follow you from young to old, from now to forever.

I can feel that my parents have always been watching me by their hearts in these years that I am going for the PhD, as close as they watched me to enter the departure hall on 3rd September 2012. Your great concerns drive me to go forward with power; your endless supports encourage me to overcome any difficulty!

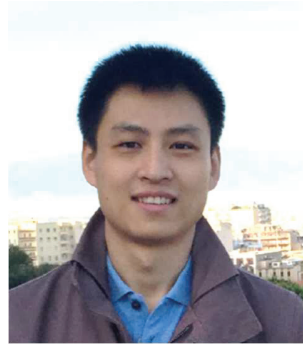
在荷兰攻博这几年，我知道父母始终都在心里注视着我，如同注视着我当年步入机场候机室准备搭乘飞往荷兰的航班。您们伟大的关怀使我充满前进的动力；您们无尽的支持为我提供面对困难的勇气！

Zhen Yang

16 May 2018

CURRICULUM VITAE

Zhen Yang (杨震) was born in Hohhot, Inner Mongolia, China on 28th June, 1986. He received his BSc degree in Traffic Engineering at Beijing Institute of Technology (Beijing) in 2009. After that, he conducted master study in Railway Engineering at Tongji University (Shanghai) under the supervision of Prof. Songliang Lian. His master research includes numerical modelling and field/laboratory measurements of wheel-rail contact forces and track vibrations. After obtaining the MSc degree in 2012, he joined the research team of Prof. Zili Li in Delft University of Technology (Delft, Netherlands) for PhD study. His PhD research focuses on the modelling of wheel-rail dynamic interactions, as presented in this thesis.



LIST OF PUBLICATIONS

Z. Yang, Z. Li, R.P.B.J. Dollevoet, An Explicit Integration Finite Element Method for Impact Noise Generation at a Squat, Notes on Numerical Fluid Mechanics and Multidisciplinary Design, 126 (2015) 63-70.

Z. Yang, Z.L. Li, R. Dollevoet, Modelling of non-steady-state transition from single point to two-point rolling contact, Tribology International, 101 (2016) 152-163.

Z. Yang, A. Boogaard, R. Chen, R. Dollevoet, Z. Li, Numerical and experimental study of wheel-rail impact vibration and noise generated at an insulated rail joint, International Journal of Impact Engineering, 113 (2018) 29-39.

Z. Yang, A. Boogaard, Z. Wei, J. Liu, R. Dollevoet, Z. Li, Numerical study of wheel-rail impact contact solutions at an insulated rail joint, International Journal of Mechanical Sciences, 138-139 (2018) 310-322.

Z. Yang, Z. Li, Numerical modelling of wheel-rail dynamic interaction with wheel lateral motion -- a contribution to the study of wheel squeal noise, under review by Journal of Sound and Vibration.

Z. Yang, X. Deng, Z. Li, Numerical modelling of dynamic frictional rolling contact with an explicit finite element method, Submitted to International Journal of Mechanical Sciences.